POLYTECHNIQUE MONTRÉAL

affiliée à l'Université de Montréal

Growth control and study of ultrathin silver films for energy-saving coatings

SOROUSH HAFEZIAN

Département de Génie physique

Thèse présentée en vue de l'obtention du diplôme de *Philosophiae Doctor*

Génie physique

Mai 2019

POLYTECHNIQUE MONTRÉAL

affiliée à l'Université de Montréal

Cette thèse intitulée :

Growth control and study of ultrathin silver films for energy-saving coatings

présentée par **Soroush HAFEZIAN**

en vue de l'obtention du diplôme de *Philosophiae Doctor*

a été dûment acceptée par le jury d'examen constitué de :

Michael WERTHEIMER, président
Ludvik MARTINU, membre et directeur de recherche
Stéphane KÉNA-COHEN, membre et codirecteur de recherche
Sjoerd ROORDA, membre
Pandurang ASHRIT, membre externe

DEDICATION

À mes parents

ACKNOWLEDGEMENTS

RÉSUMÉ

Les couches minces fonctionnelles jouent un rôle prépondérant dans la plupart des secteurs industriels actuels. Ils peuvent aussi bien être une partie intégrante d'un dispositif (cellule solaire, diode électroluminescente, photodétecteur, Laser, capteur thermosolaire, cellule thermoélectrique et bien d'autres), ou bien y amener de nouvelles fonctionnalités (revêtements résistants à la corrosion, l'usure et l'érosion, revêtement antireflet). La montée rapide de cette science est à l'origine d'un développement tout aussi rapide des techniques de dépôt et de synthèse de couches minces. Aujourd'hui, la croissance d'une couche mince avec une précision au nanomètre peut être effectuée par un simple couchage à lame au sein d'un laboratoire de recherche aussi bien que par des techniques d'évaporation dans des chambres à vide industrielles à grande échelle.

La facilité d'accès aux techniques de dépôt ainsi que l'envergure des applications scientifiques et technologiques font des couches minces une solution potentielle pour beaucoup d'enjeux technologiques et de sociétés. Certainement, un des plus grands enjeux actuels est le problème de la consommation énergétique à travers le monde et qui peut seulement qu'empirer si aucune solution convenable n'est adoptée. Une approche afin de contrer cette consommation énergétique est de modifier les vitrages architecturaux dans les bâtiments commerciaux et résidentiels en revêtant une fenêtre avec une couche réfléchissante la chaleur afin de réduire de façon drastique les charges de chauffages et de refroidissement. Le recouvrement des fenêtres par de fines couches optiques se fait par des chambres de dépôts montées en ligne, souvent jumelées avec la production du verre flotté. Bien que le maintien et l'installation de ces systèmes de dépôt est d'un grand intérêt et pose de nombreux défis, le travail de recherche présenté dans cette thèse se penche sur le mécanisme de croissance des couches minces d'argent déposé en phase vapeur par assistance plasma pour les filtres à basse émissivité. Le projet est mené en collaboration avec *Guardian Industries* dans le cadre des vitrages à économies d'énergie.

Les couches minces d'argent possèdent des propriétés physiques changeantes dépendamment de leur mécanisme de croissance ainsi que de leur épaisseur. Elles ont tendance à croître en îlots en dessous d'une épaisseur critique et convergent vers une couche réfléchissante la radiation infrarouges. Cette épaisseur critique se nomme le seuil de percolation et dépend fortement de la couche sous-jacente. De plus, le caractère catalytique de l'argent fait en sorte qu'il est hautement

susceptible aux espèces réactives présentes dans le plasma ainsi que les groupes carboxylés présents dans l'atmosphère. De ce fait, une couche protectrice doit être employée afin de protéger les propriétés optiques et électriques de ces couches d'argent. Afin de mieux comprendre le processus de croissance de ces couches minces, nous avons développé une méthode optique non invasive afin de déterminer le moment précis de la transition des nanoparticules d'argent en couche continue. Cette étape est mieux connue sous le nom de seuil de percolation et est caractérisée par un changement drastique des propriétés optiques et électriques. On démontre que les surfaces ayant une énergie plus élevée (ou un caractère plus métallique) promeuvent une croissance par couche tandis que les surfaces possédant une énergie moins élevée (un caractère diélectrique) facilitent la croissance de l'argent par îlot. À titre d'exemple, en utilisant une couche de stannate de zinc on peut réduire le seuil de percolation par 18% comparativement à l'oxyde de zinc et de 80% comparativement au dioxyde de silicium.

Les atomes d'argent réagissent aisément par échange d'électrons afin de former des composés moléculaires. Le sulfure d'argent est un exemple de composé qui se forme lorsqu'un atome de soufre et d'argent forment un lien covalent. On démontre la formation d'une couche mince d'argent sur une monocouche à base de thiol, le 3-mercaptopropyl)trimethoxylosilane (MPTMS). La formation de lien chimique sur la surface inhibe la formation d'îlots et permet la formation de couches ultraminces d'argent. À partir de ce traitement, il est possible d'obtenir des couches minces possédant des propriétés d'argent massif pour des épaisseurs de seulement 7 nm, beaucoup moins que ce qu'on aurait pu obtenir en utilisant des couches de croissance possédant une haute énergie de surface. De plus, on a démontré la formation de la monocouche de liens thiol sur une couche de nitrure de silicium afin de créer un empilement à trois couches à basse émissivité avec d'excellentes propriétés de réflexions de radiation infrarouge. L'environnement plasma utilisé pour déposer les couches minces peut être riche en espèces réactives et autres contaminants. Suite au dépôt de la couche d'argent, une couche protectrice est nécessaire avant de déposer des couches d'oxydes. Si les espèces réactives telles que l'oxygène dissocié à l'intérieur du plasma parviennent à la couche d'argent à travers la couche protectrice, des dommages irréversibles peuvent être amenés à la couche d'argent. En utilisant des techniques de caractérisation de surface précises, on démontre que ce processus de dégradation est initié par la migration des atomes d'argent à travers la couche protectrice, un processus très similaire à l'effet Kirkendall. De plus, on démontre qu'en utilisant

un traitement de surface de MPTMS afin de créer les liens soufre-argent, la migration des atomes d'argent est hautement réduite (jusqu'à 20x) comparée à une surface non traitée.

Finalement, nous développons une méthode de suivi optique afin de contrôler les propriétés optiques de nanoparticules d'argent en changeant de façon précise leur environnement diélectrique ainsi que leur distribution de tailles. On démontre ainsi une façon simple de synthétiser des nanoparticules à enveloppe en plaçant des nanoparticules d'argent incorporées dans une couche protectrice dans un plasma réactif. En contrôlant de façon précise la passivation de la couche externe, on démontre qu'il est possible d'obtenir des nanostructures de type noyau-enveloppe. De plus, nous démontrons l'effet de la température du substrat sur croissance et diffusion des nanoparticules. En dessous d'une certaine température, les atomes d'argents peuvent se détacher des agglomérats pour continuer de diffuser sur la surface jusqu'à atteindre un site de nucléation stable. Au-dessus de cette température, les atomes d'argent atteignent un équilibre et la diffusion en surface est inhibée.

ABSTRACT

Functional thin films play a key role in almost all industries today. They can either form an integral part of a device (as heat-reflectors, solar cells, light-emitting diodes, photodetectors, lasers, thermal collectors, thermoelectric cells and many more) or bring additional coating functionalities (such as corrosion, wear and erosion resistance and antireflective coating). The rapid development of thin film science has led to the equally fast growth of thin film deposition techniques. The coating of a surface with precisions in the nanometers can be conducted by simple blade coating in a laboratory setting or large-scale vacuum chambers in heavy industrial environments. Moreover, the rapid rise of thin film science can also be attributed to progresses in characterization techniques.

The accessibility of thin film deposition techniques and their wide-ranging scientific and technological applications make thin film science appear as an attractive answer to many industrial and societal challenges. Probably the greatest of these challenges is the energy consumption problem present in large parts of the world and which can only amplify in time if no suitable solutions are adopted. One approach to decrease this energy consumption is to alter glazing units in commercial and residential buildings by coating one side of the window pane with a heat-reflecting layer in order to drastically reduce heating and cooling loads. These glass panes are manufactured by large, in-line vacuum coaters that can be found on the glass production site. Even though the configuration and maintenance of such systems is of great interest and brings important challenges, the research work conducted throughout this thesis is focused in the growth mechanism of very thin silver films inside a low-emissivity stack deposited by plasma-assisted physical vapour deposition, with collaboration with Guardian Industries in the context of energy-saving glazing.

Silver thin films have unique varying physical properties attributed to their distinct growth mechanism. They tend to progressively grow as light-absorbing agglomerated clusters below a certain thickness to infrared heat-reflective, continuous films. The main challenge in the context of silver film growth is the inability to obtain heat-reflecting properties below a certain thickness. This thickness is determined by the surface properties of the underlying layer, limiting the possible options available for silver film coating. Moreover, the catalytic nature of silver makes them highly susceptible to reactive oxygen present inside the plasma and carboxyl groups in ambient atmosphere, therefore protective means need to be employed to preserve their optical and electrical

integrity. To better understand the growth process of very thin layers of silver, we have developed a non-invasive optical method to determine the precise moment when silver clusters evolve to a continuous layer. This step is known as the percolation stage and is characterized by drastic changes in the thin film optical and electrical properties. We find that surfaces with increased surface energy (or more metallic character) are better suited to continuous silver film growth (inhibiting the cluster formation) while surfaces with lower surface energy (more dielectric character) are more suited to island formation. As an example, we find that by using zinc stannate we decrease the percolation thickness by 18% compared to zinc oxide and 80% compared to silicon dioxide.

One way to obtain very thin conductive metallic silver film is by surface modification of the underlying layer. We demonstrate the formation of silver-sulfur bonding by coating an oxide layer with a (3-mercaptopropyl)trimethoxylosilane (MPTMS) thiol-based chemical treatment. The chemical bonding on the surface creates nucleation sites that inhibit island growth formation and permit the formation of ultra-thin silver films. Using this treatment, we obtain thin silver films with bulk optical properties at only 7 nm thickness, much less than what could be obtained using high-surface energy seed layers. We also demonstrate thiol formation on a nitride film to create a dielectric/metal/dielectric symmetric low-emissivity stack with enhanced heat-reflecting properties. Moreover, the plasma environment used to deposit the thin films necessary in low-emissivity coatings can be rich in reactive species and other contaminants. After the successful deposition of a continuous silver layer, a top protecting layer is mandatory before depositing additional oxide layers. If reactive species such as reactive oxygen reaches to the silver through the protective coating, irreversible damage can be sustained on the silver layer which promptly degrades. Through very precise surface characterization techniques, we find that the degradation process is initiated by silver atom migration through the top barrier coatings, a process akin to the Kirkendall effect. We demonstrate that by using an MPTMS surface treatment to bind the silver atoms onto the seed layer, the silver migration is greatly reduced (up to 20x) compared to an untreated surface.

Finally, we develop a direct optical monitoring method to tailor the optical absorption properties of silver nanoparticles by accurately changing their dielectric environment and size distribution. We demonstrate one way to easily synthesis core-shell nanoparticles by exposing silver nanoclusters embedded by a sacrificial layer and exposed to a plasma. By carefully controlling the

passivation of the outside shell we obtain these core-shell nanostructures. Moreover, we show the effect of substrate temperature on the shape relaxation of nanoclusters post-deposition. Below a certain critical temperature, silver atoms can detach from clusters continue diffusing on the surface until they reach a thermodynamically stable nucleation site. Above this temperature, silver atoms reach this equilibrium position and the post-deposition surface diffusion is inhibited.

TABLE OF CONTENTS

LIST OF TABLES

LIST OF FIGURES

LIST OF SYMBOLS AND ABBREVIATIONS

List of abbreviations

AC	Alternating Current
AFM	Atomic Force microscopy
DC	Direct Current
IEA	The International Energy Agency
MPTMS	(3-Mercaptopropyl)trimethoxysilane
OECD	Organisation for Economic Co-operation and Development
PVD	Physical Vapour Deposition
RF	Radiofrequency
SF	Solar Factor
SHGC	Solar Heat Gain Coefficient
TOF-SIMS	Time-Of-Flight Secondary Ion Mass Spectroscopy
XPS	X-ray photoelectron spectroscopy

Materials

Ag	Silver
Ar	Argon
Au	Gold
AZO	Aluminum doped zinc oxide
BiOx	Bismuth Oxide
FTO:	Fluorine-doped tin oxide

H	Hydrogen
ITO	Tin-doped Indium Oxide
Li	Lithium
N_2	Nitrogen molecule
NbO_x	Niobium oxide
NiCr	Nickel Chromium
O_2	Oxygen molecule
SiN	Silicon nitride
Ti	Titanium
VO_2	Vanadium dioxide
WO_3	Tungsten oxide

Physical constants

ε_0	Free space permittivity
μ_0	Free space permeability
h	Planck's constant
k_B	Boltzmann's constant
c	Speed of light in vacuum

Symbols

α	Spectral angular absorptivity
A	Spectral absorbance
A_{sol}	Solar absorbance
ε	Spectral angular emissivity

D_{65}	Spectral distribution of illuminant *D65*
I_B	Spectral radiance of a blackbody
I_{sol}	Solar irradiance
P_b	Planck distribution for blackbody radiation
Q_{amb}	Ambient radiative heat
Q_{em}	Re-emitted radiative heat
Q_s	Emitted thermal radiation from surface
R	Spectral reflectance
R_{sol}	Solar reflectance
S_{sol}	Spectral distribution of solar radiation at sea-level
T	Spectral transmittance
T_c	Critical temperature
T_{sol}	Solar transmittance
T_{vis}	Visible transmittance
V_{ph}	Spectral luminous efficiency for photopic vision

LIST OF APPENDICES

CHAPTER 1   INTRODUCTION

Due to massive urbanization during the two previous centuries, the question of energy management can't be dissociated from the energy consumption of residential and commercial buildings as the urban population density increases. Efforts towards research and technological developments for the purpose of reduced energy consumption in buildings are increasing on a global scale. One important development is the architectural glazing unit made of very thin optical layers to modulate the incoming solar radiation, allowing for significant reduction in the space heating or cooling energy consumption.

The use of thin film technology for energy saving is relatively new and has found tremendous success due to industrial scaling of effective coating methods and research interest in the wealth of possible applications inherent to the properties of thin films. However, this established, but yet open field, will require novel ideas to overcome the gap between today's building energy management and the next generation of green, sustainable and even energy producing buildings. The doctoral project described in this thesis has been performed in collaboration with *Guardian Industries* and includes scientific research pertaining to the design, fabrication and optimization of low-emissivity (low-e) coatings performance using vapour phase deposition techniques. The present chapter will provide a brief overview of the problematics in the field of low-emissivity windows and the future trends that are to be expected in this field.

1.1 Problem definition

1.1.1 Worldwide energy consumption

The building sector accounts for approximately 35% of the world's delivered energy consumption (among the industrial, transport and agriculture sectors) and for one-third of total energy-related CO_2 emissions. With the ongoing urbanization of developing countries, the net energy consumption of buildings (in the form of electricity and natural gas) is expected to increase by 32% until 2040 [1]. Thus, at the current rate, the energy consumption grows faster than the world's population. A significant part of this consumption is related to the energy required to regulate the heat inside the building: cooling during summer in generally warm climates, and heating during winter or in generally cold climates.
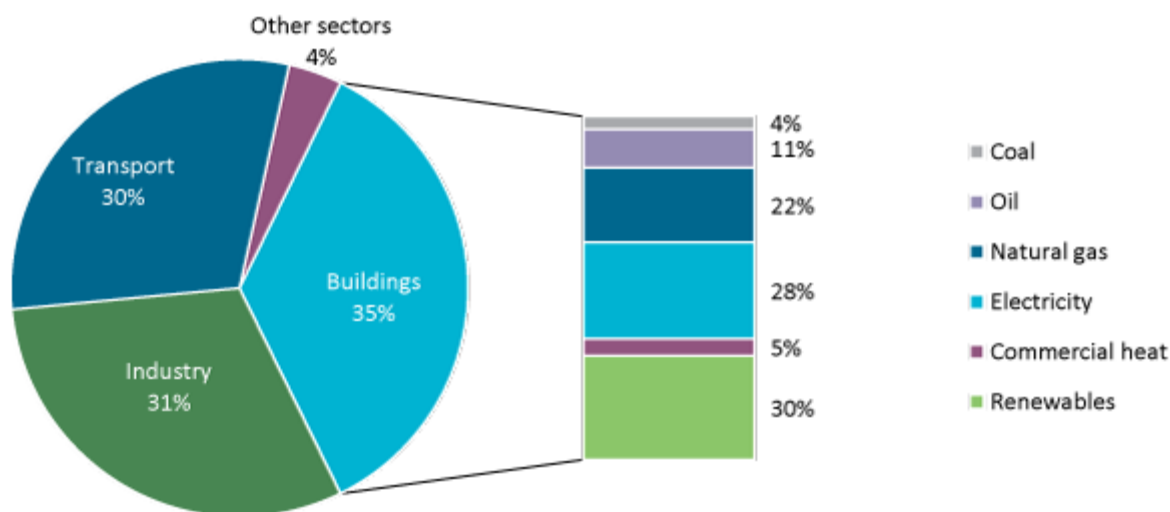
Figure 1.1 : Final energy consumption by sector and buildings energy spread. From [2].

Figure 1.1 shows the energy consumption by sector for member countries of Organisation for Economic Co-operation and Development (OECD). We see that half of the energy demands of buildings is provided by electricity and natural gas. Therefore, a reduction in the global building energy consumption results in direct decrease of electricity usage as well as a reduction in the global CO_2 emission. Moreover, as the world population continues to grow, we can expect these numbers to increase as well. The International Energy Agency (IEA) is expecting the energy consumption related to space heating to increase by a total of 150% in developed countries and up to 600% in developing countries by 2050 [3].

The energy needed to heat or cool a building is dictated by the building envelope: This encompasses the roofing, wall, windows and foundations. An optimal building envelope must include proper sealing aimed for low air insulation, high reflective surfaces (in hot climate) such as white-coloured roof and high-performance windows with climate-appropriate solar heat gain coefficient (SHGC). It has been estimated that a high-performance building envelope necessitates only 20% of the average energy currently required to heat a building in a cold climate (for an OECD country member). In hot climates, the energy savings from reduced energy needs for cooling can go up to 40% [2]. The goal is to eventually reach the 'energy-zero code' building, where the yearly total consumption of the building amounts to the total energy gained from renewable energy sources stemming from the design and technologies utilized in the building; this includes even a positive

energy balance building which is not only self-sustainable but can also store and generate usable energy. Moreover, besides the need for new regulations for future building construction, it is estimated that up to 90% of the present infrastructures in the northern hemisphere will be operational in 2050 [4] and will necessitate modern renovations to meet new building code standard. Most building can last well over 100 years and the retrofitting can be costly; therefore, an appropriate design of the building envelope from the ground up is a vital requirement for long-term sustainability.

One of the key aspects of energy management in buildings resides in the glazing unit chosen for beneficial heat conservation or rejection by regulating the incoming solar radiation. The housing paradigm has shifted from residential buildings with a low glazing area to edifices with high glazing area, to benefit from increasing lighting comfort. Unfortunately, clear, untreated float glass is highly emissive and is responsible for solar radiative heat entering the building during the day in hot climates and interior blackbody radiation leaving the building at night in cold climates, causing excess charges in cooling and heating requirements. Figure 1.2 shows the world map divided into regions of low, moderate and high demands of heating or cooling. The map is divided into 17 different zones according to the annual demand in heating and cooling. We see that a very large portion of the maps relies solely on only heating or only cooling building demands.
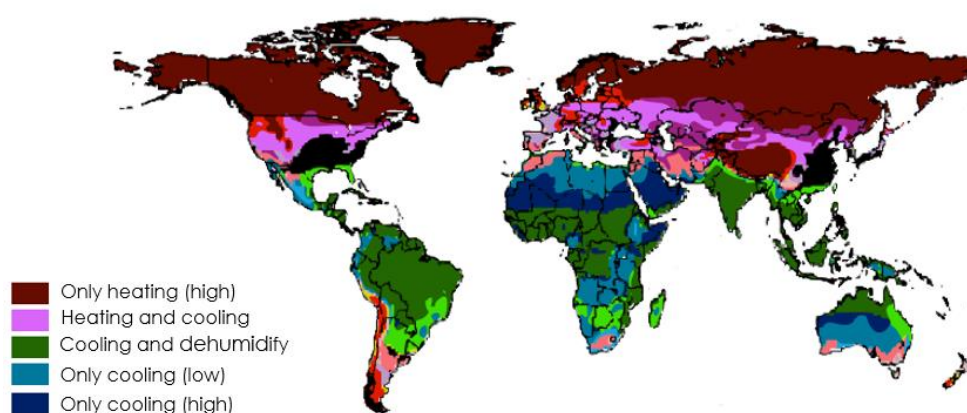
Figure 1.2: World map of different climate zones according to the energy demands for heating or cooling. Modified from [5].

By using low-emissivity glazing in specific regions, the building units can benefit from coating treatments that convert a highly emissive float glass to a functional, energy efficient window. The technologies required to achieve this feat are vacuum-based technologies and the mechanisms behind the energy savings of low-emissivity coatings are related to the physics of thin films. Passive, low-emissivity coatings carefully designed for filtering the incoming energy radiation can be applied on single, double or triple glazing units and provide significant energy savings. Figure 1.3a shows the incoming solar radiation at sea level. Approximately half of the total radiation is in the visible spectrum (380-780 nm) and the other half lies in the near-infrared. The main challenge of the low-emissivity glazing is to achieve a high level of comfort and aesthetics (by providing high transmission and neutral color) and at the same time filter the desired amount of infrared radiation.

The working principle of a low-emissivity stack is to filter the incoming radiation by reflection from a thin, conductive transparent layer so that only a fraction of the total radiation is transmitted inside the building, as shown from the filled blue and green spectra in Figure 1.3a. In a hot climate, we want most of the solar radiation to be reflected outside by using a 'low solar gain' design. In a cold climate, we want a good portion of the solar radiation to be transmitted inside, while preventing the ambient blackbody radiation to escape at night, by using a 'high solar gain' design. Energy savings using this approach can be substantial over time. The US National Research Council estimated that low-emissivity glazing units were responsible for 1.79 trillion kW•h of cumulative savings in residential heating energy consumption from 1983 to 2005, which amounts to $37 billion (in 2003 dollars) in direct energy cost savings. The complete architecture of a low-emissivity device includes a very thin silver film (of the order of 8 to 10 nm) encapsulated by various metal-oxides to obtain the highest performance. Figure 1.3b shows a typical design for a low-emissivity coating, where a thin, infrared heat reflective silver layer is encapsulated between two transparent thin films. The blocking layer prevents ionic diffusion from the float glass production line into the layers. The seed layer helps the growth of the silver film, which acts as a passive heat reflector.
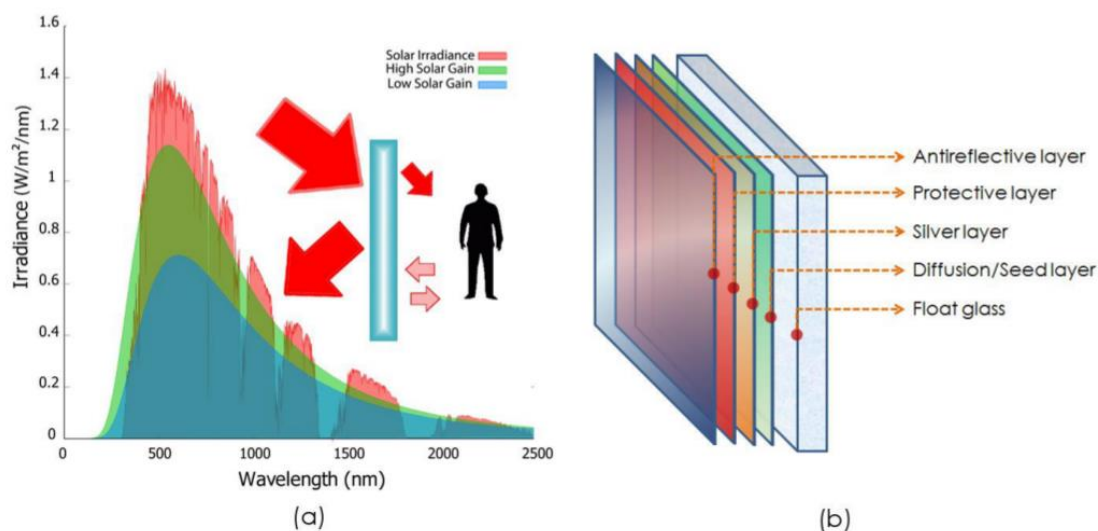
Figure 1.3: (a) Transmission spectra of high and low solar gain low-emissivity coatings against the incoming solar radiation at sea level (b) low-emissivity stack

The protective layer prevents damage made to the silver layer during the deposition process where reactive species generated inside the deposition chamber can corrode the silver film. Finally, the antireflective coating increases the visible transmission by reducing the reflection from the coated side using optical interference. This architecture acts as a guideline for a low-emissivity design but can be altered to bring additional functionalities (such as self-cleaning and resistance to erosion) of the glazing unit. The fundamental aspect of the thin-film stack is to maintain high visible transparency while lowering the overall emissivity. In that regard, reducing the silver film thickness while maintaining excellent electrical properties could not only achieve better optical properties but provide substantial economic savings (even a 10% reduction in silver film thickness can be sizeable when scaled over hundreds of millions of square meters.)

1.1.2 Silver growth and percolation

The use of silver at the nanoscale has extended over recent years to the development of applications such as low-emissivity windows [6, 7], transparent conductive electrodes (TCEs) [8-10], photovoltaics [11, 12], and studies on subwavelength confinement of light [13-15]. The extremely small scale at which silver films (or nanoparticles) are optically and electrically active makes the devices' overall performance highly dependent on the choice of substrate and underlayer, surface

treatment, and growth mechanisms [16-19]. The growth mechanism during the deposition of silver and other transition metals on oxide surfaces has been explained as a surface diffusion, nucleation, and coalescence process in which the initial nucleation sites form and expand to nanoclusters (or nano-islands) by ad-atom capture, while subsequently forming a thin continuous film [20, 21].

The properties of the silver layers are expected to be very different at the various stages of growth as also reflected by the wide variety of applications based on silver on the nanoscale. The agglomeration of silver particles or clusters on the surface can be seen as a localized concentration of free electrons, which absorb incoming electromagnetic radiation. As aggregates expand, they connect to neighbouring clusters to eventually form a continuous film, a transition labeled the percolation threshold. This transition also marks the evolution between separated nanoclusters into a continuous, conductive film with heat-reflecting properties.

Various strategies have been employed eliminate cluster formation by modifying the surface beneath the silver film (the 'seed' layer). For example, a sub-nanometer Cu or Ge layer can provide nucleation sites for silver atoms, reducing their diffusion time on the surface which lead to the formation of a smooth silver film by suppressing nanoclusters formation [22]. Similarly, using a high-surface energy transparent film such as ZnO or PEDOT:PSS [23] one can inhibit the diffusion of evaporated silver atoms and produce thin, continuous films. Figure 1.4 shows the effect of a sub-nanometer Ge film on the silver growth. With the Ge seed layer, we obtain a continuous silver film whereas without the Ge layer we have separated nanoclusters for the same amount of deposited silver material.
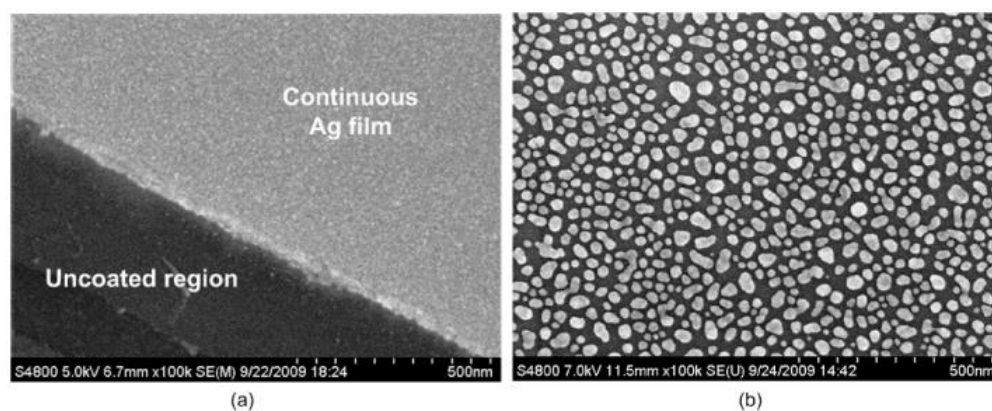
Figure 1.4: Comparison between a 6 nm silver layer with (a) and without (b) a Ge wetting layer. Reprinted with permission from [22]

Similarly, a sub-nanometer Nb helps with early percolation and surface roughness reduction of silver films. Fig. 1.5 shows a 25 nm Ag film deposited on a TiO_2 and Nb-coated (0.1 nm nominal thickness) TiO_2.
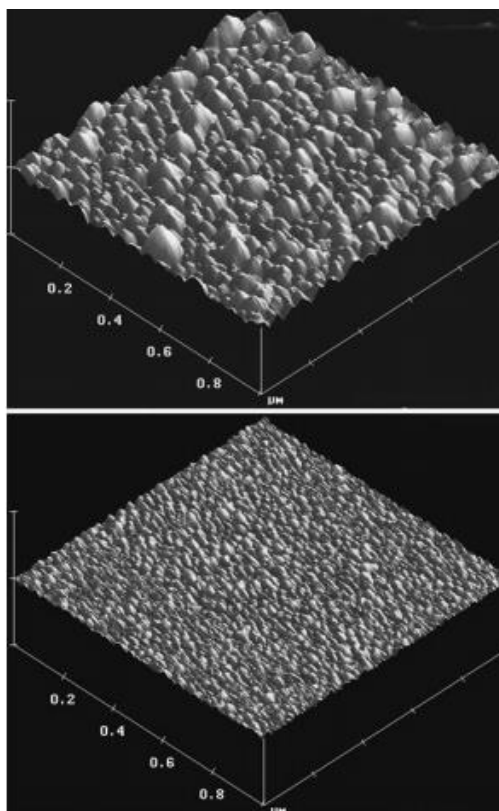
Figure 1.5: AFM pictures (1 μm ×1 μm) of a 25 nm Ag layer deposited without Nb (top) and 0.1 nm Nb on TiO_2 (bottom). Reprinted with permission from [24].

The concept of metal-seeding has been extended to various elements such as Ti, Ni, Cr, Ta and Mo [24]. In some extreme case, the percolation threshold of a Au layer has been reduced to 1 nm using a sub-nanometer Cu seed layer [25]. The pre-inclusions of these metals cover the otherwise uniform oxide surface with nucleation sites that stop the diffusion of silver atoms through preferential binding. Nucleation of Ag on these metal seeds and subsequent thin film formation may be seen thermodynamically as a minimization of the surface free energy. If the interfacial free energy γ_{int} (between the metal adatom and the substrate) is larger than the free surface energy mismatch between the bare substrate γ_{sub} and bare metal γ_m free surface energy, then island growth is

favoured. In other words, if $\Delta\gamma = \gamma_m + \gamma_{int} - \gamma_{sub} > 0$, island formation is favoured and for $\Delta\gamma < 0$, wetting of the metal layer occurs [24, 26]. In other words, a substrate with free surface energy similar (or higher) than the deposited adatom will decrease the residual free surface energy $\Delta\gamma$ and a layer-by-layer growth is initiated [27].

To understand the phenomena inherent to Ag growth, one can also use percolation theory. In this description, an arbitrary number of sites on a square lattice (or substrate) have a probability p of being occupied and a probability 1-p to be unoccupied, as shown in Fig. 1.6. In case of a conductive material, unoccupied sites represent insulating regions whereas occupied sites represent conductive regions. The growth of aggregates is not favourable to the formation of smooth, transparent conductive films and therefore we want to minimize the transition between separated clusters to a conductive film. Low melting point metals such as silver, gold and copper tend to have high diffusion coefficient when they are evaporated on a dielectric surface, owing to their high mobility. In the percolation theory picture, one way of reaching the critical density is to increase the probability p for each site by limiting atomic diffusion on the surface.

<div align="center">

p = 0.2   p = 0.59   p = 0.8

</div>
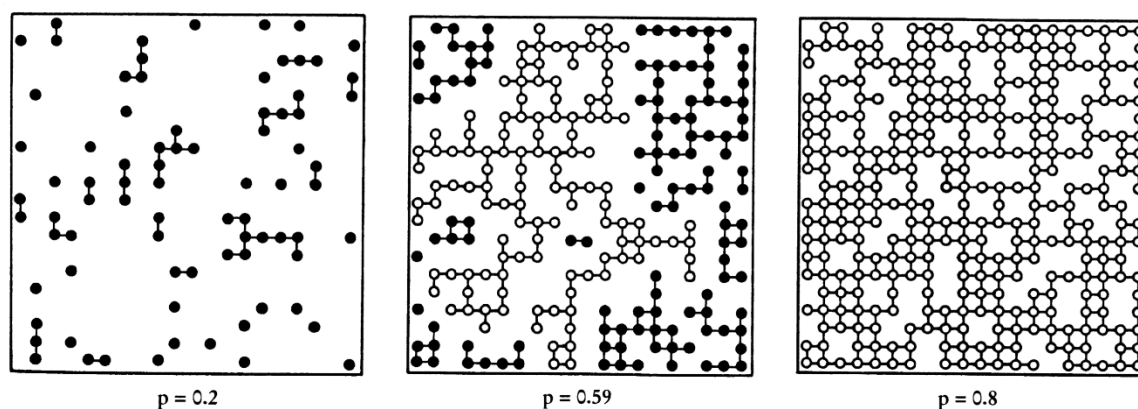
Figure 1.6: Probabilistic percolation theory. Each site on the square lattice has a probability p to be occupied. The filled dots represent discontinued clusters while the empty dots represent continuity from one edge of the lattice to another. Reproduced with permission from [28].

The critical density of nucleation points is reached when there is a continuous path from one side of the substrate to the other. This moment is labeled the critical density and represent the transition between a dielectric and a conductive layer with a finite filling probability p_c is associated with this

transition. Many physical properties of a metallic film such as their optical and physical properties can be linked to percolation. Since surface conductivity occurs at the percolation threshold, for $p > p_c$ the d.c. conductivity σ_{dc} is proportional to $|p - p_c|^u$, where u is a constant based only on the dimension of the lattice (substrate). For a two-dimensional film, u is equal to 1.30 and 1.99 for three-dimensional systems [28, 29]. Since surface filling probability p is linked to the film nominal thickness, we can state that $\sigma_{dc} \propto |d - d_c|^{1.3}$ for a two-dimensional thin silver film, for film thickness d greater than the percolation thickness d_c [28].

1.1.3 Silver degradation and the Kirkendall effect

Like other transition metals in the periodic table, silver physical properties (conductivity, ductility and electronegativity) are caused by its electronic configuration ($[Kr]4d^{10}5s^1$) characterized by a single electron in the $5s$ orbital and an unfilled d-orbital in its ionic form (Ag^{2+}). This particular electronic configuration makes silver widely used as catalyst in many applications, and at the same time susceptible to form compounds that can potentially lead to the degradation of the film. The various degradation routes of silver have been reported as thermal decomposition, oxidation and atmospheric degradation. Silver degradation in ambient conditions is due mainly to the formation of silver sulfide (Ag_2S) and silver chloride ($AgCl$), as well as carbonate compounds (Ag_2CO_3). Oxidation of silver, however, does not occur in ambient conditions (even at high temperatures). A thin oxygen adsorbate layer can form on the silver layer, but no direct reaction with oxygen will occur. To form oxide compounds (Ag_2O_2, AgO, Ag_2O), atomic oxygen or oxygen ions found in low-earth orbit or deposition chambers, for example, are required.

When exposed to reactive oxygen, silver oxides will initially nucleate on the exposed silver surface. Due to a different diffusion coefficient between silver oxide outer layer and silver ions, the mobile Ag ions will start migrating outwardly through the oxide shell. The two materials (the silver oxide barrier and the silver layer) will migrate at a different rate. This different rate of diffusion will generate voids to compensate for the silver ions migrating outward, adding porosity to the material. Figure 1.6 shows an example of Ag nanowire exposed to an oxygen plasma. We can see that the exposure of the nanowires to the reactive oxygen generates increased porosity over time. This increase in porosity in the silver film in addition to the oxidation will drastically decrease silver film performance. The migration of two different materials through the interface separating them

and void generation has been known as the Kirkendall effect and has been exploited to create exotic nanostructures [30].
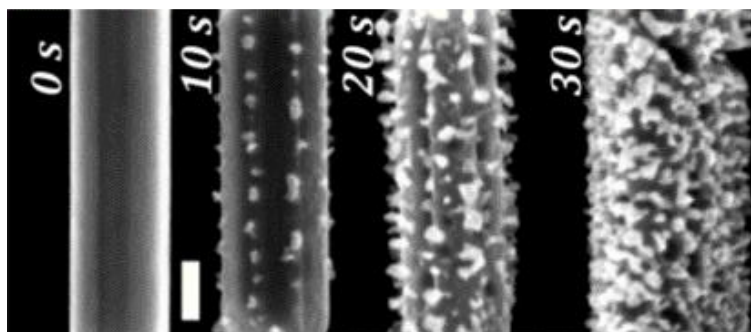
Figure 1.7: Ag nanowires (175 nm diameter) exposed to air plasma. Scale bar: 100 nm. Reprinted with permission from [31].

The Kirkendall effect is not only restricted to nanostructures such as nanoparticles or nanowires but can also occur for a planar configuration (dielectric/metal/dielectric). Figure 1.7 shows the interfaces between a silver film and TiO_2 layers before and after exposure to an oxygen plasma.
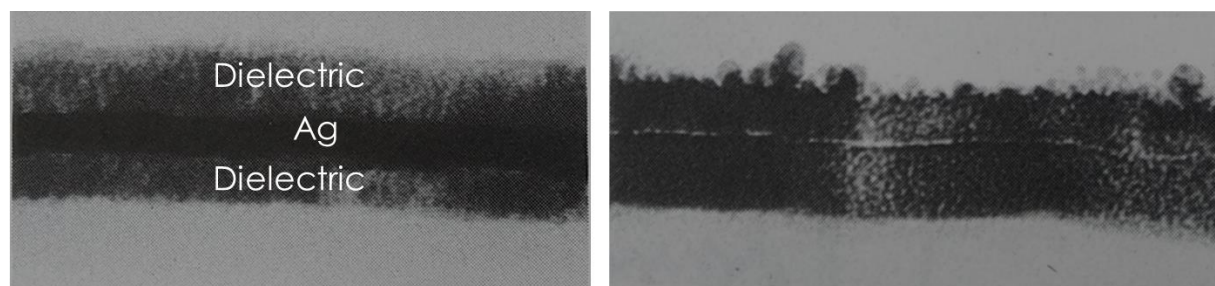
Figure 1.8: TiO_2 (20 nm)/Silver (14 nm)/TiO_2 (20 nm) film degradation following exposure to oxygen plasma. We see a clear interface separating the layers before the oxidation and interface mixing after the degradation. Reprinted with permission from [32]

Therefore, to obtain durable low-e coatings, we must control the growth of silver in order to get a rapid transition into the percolation threshold to obtain a smooth, continuous layer and protect the silver film from reactive oxygen.

1.2 Objectives

The central objective of this thesis is to optimize silver thin film properties by exploring new ways to obtain the thinnest possible continuous silver layers while maintaining their optical and electrical performances. By working on a set of novel monitoring tools and hybrid fabrication steps, we seek to obtain high performance and durable low-emissivity coatings that could help to cover the technological gap between today's building design and high-performance envelopes. To achieve our central objective, this thesis present four sub-objectives, stated as follows:

1. Develop real time, *in situ* optical monitoring tools to understand the impact of deposition parameters on the evolution of the growth of metallic films on the nanoscale and detect the percolation threshold by using an all optical method.

2. Investigate thin silver films properties with improved heat rejecting performances by combining chemical surface modification and vapour deposition techniques.

3. Use surface treatment to prevent silver thin film degradation by atomic migration through the protective layers and void propagation caused by reactive oxygen during plasma-based process.

4. Develop optically dense and tunable plasmonic core-shell metallic nanostructures with industrial vapour deposition techniques for use in tinted, glare reducing and optically selective coatings.

1.3 Outline

The thesis is divided into 9 chapters, starting with the present chapter. In chapter 2 we will give an overview of the state-of-the-art energy saving thin film technologies, with a focus on current progresses and avenues in low-emissivity thin film stacks. Chapter 3 lays down the theoretical background for thin film deposition and growth in plasma-based processes. Chapter 4 reviews the experimental apparatus used to obtain the results presented in the thesis. Chapters 5 to 8 are the core results of this thesis. In chapter 5 we present a novel method to monitor silver thin film growth by measuring Stoke's parameters in real-time. We show how to determine the percolation threshold of thin silver films using this method and test the growth of silver on different substrates. In chapter 6 we combine physical vapour deposition and chemical surface treatment to produce a high-quality, minimalistic SiN/Ag/SiN low-e architecture and demonstrate that a non-wetting surface can be

converted to a wetting layer using this treatment. In chapter 7 we investigate the degradation mechanism of silver in the presence of reactive oxygen and we present a solution on how to protect against this degradation. We observe that the deterioration process is akin to the nanoscale Kirkendall effect, where silver ions migrate towards the flux of diffusive oxygen within the thin film stack, even in the presence of a metallic barrier. In chapter 8 we demonstrate the fabrication of tunable core-shell nanoparticles deposited by magnetron sputtering using *in-situ* oxidation in a plasma. Moreover, we study the effect of temperature on the nano-islands distribution using *in-situ* ellipsometry to enable the fabrication of tunable solar-spectre selecting coatings. Finally, in chapter 9 we give a general discussion and outline the perspectives of the impact of our work on this field.

CHAPTER 2   LOW-EMISSIVITY WINDOWS

2.1 Historical development

The use of thin silver films (with nanoscale dimensions) as a heat-reflective element can be dated back to 1916 with the invention of a 'transparent screen' mask for foundry furnace workers [33]. The function of this mask was to protect the workers from

> "[…] the action of the ultra-violet rays at one end of the spectrum, and the infra-red or heat rays at the other end, for the eye is not injured by the mid-spectrum white light of moderate intensity."

The prototype mask was designed to have a glass substrate coated using cathodic arc deposition with a thin metallic film (copper, gold, tungsten or nickel) and joined to a secondary slab of glass using a transparent resin, in order to protect the thin metallic film from mechanical degradation. The theoretical framework for this heat-rejecting effect was developed based on the well known effect that the reflectivity R of a conductor at a certain electromagnetic frequency ω is related to its direct current (DC) conductivity σ through the Hagen-Rubens relation [34]:

$$R = 1 - 4\sqrt{\frac{\omega \pi \varepsilon_0}{\sigma}} \tag{2.1}$$

where ε_0 is the free space permittivity. For electromagnetic frequencies lower than the mid-infrared, the above relation holds well (Figure 2.1). As the frequencies increase to near-infrared and the visible range, other phenomena govern the optical response of the material (as we will see in Chapter 3).
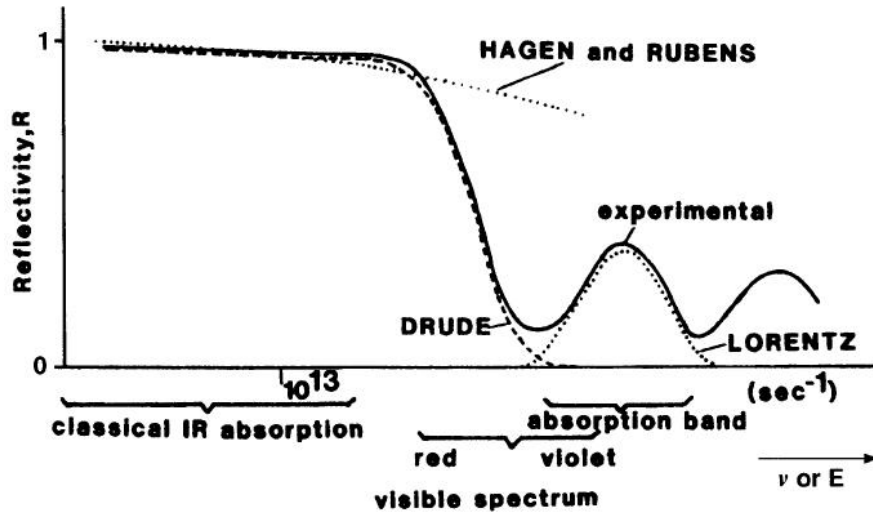
Figure 2.1 : Schematic frequency dependence of the reflectivity of metals, experimentally (solid line) and according to three models. Reproduced with permission from [35].

Similarly, the study of radiative emission from a heated object and the relation between the radiation emitted by an object relative to the amount of radiation absorbed dates back to the 19th century; it can be well understood through the Kirchhoff's radiation law [36]:

$$\varepsilon(\theta, \lambda) = \alpha(\theta, \lambda) \tag{2.2}$$

stating that at thermal equilibrium, the spectral angular emissivity $\varepsilon(\theta, \lambda)$ over a hemisphere above the surface area and electromagnetic wavelength λ, is equal to the spectral angular absorptivity $\alpha(\theta, \lambda)$, and that a low absorbing medium (such as a highly reflective surface) would also demonstrate low emissive properties. The emissivity is a crucial parameter to determine Q_s, the emitted thermal radiation from the sample at a specific temperature T, given by [36, 37]

$$Q_s(T) = \int d\Omega_s \cos\theta \int_0^\infty d\lambda I_B(T, \lambda)\varepsilon(\theta, \lambda) \tag{2.3}$$

where $\int d\Omega_s = \int_0^{\pi/2} d\theta \sin\theta \int_0^{2\pi} d\varphi$ is an integral over the hemisphere above the emitter with the azimuthal angle φ and polar angle θ. The spectral radiance of a blackbody I_B at a specific temperature T is given by

$$I_B(T,\lambda) = \frac{2hc^2}{\lambda^5}\left[e^{hc/(\lambda k_B T)} - 1\right] \tag{2.4}$$

Where h is the Planck's constant, c the speed of light in vacuum and k_b Boltzmann's constant.

It was only in 1937 that the first patent for a heat-reflecting roller-blind was issued for the specific use for energy saving in a residential building [38]. The invention prescribed the use of a thin silver film to filter out the infrared portion of the light and to transmit only the visible portion. However, no companies at the time saw the potential of these heat-reflecting devices, nor was there an incentive for replacing clear glass as fenestration units.

Throughout the following decades, major advances in coating technologies enabled the study of thin gold (Au) films embedded in bismuth oxides (BiO_x) films. The BiO_x films were deposited by alternating current (AC) sputtering and the gold film by thermal evaporation. It was promptly observed that gold films deposited on BiO_x seed layers had much better quality than when deposited directly on glass [39], and that the transmission of a $BiO_x/Au/BiO_x$ system was higher than with a single Au layer alone. These two concepts, namely the improvement of the thin metallic film quality through the underlayer (seed layer) and the increase of the visible transmission by induced transmission are still some of the main research focus of low-emissivity coatings.

The energy crisis of 1973 was a serious incentive to revise the energy policy for countries that were heavily dependent on oil. During the crisis, the price of oil and coal nearly quadrupled [40], which had a significant impact on buildings that were relying on heating oil for furnaces and coal for electricity. From that point on, numerous companies tried marketing low-emissivity windows as a solution to reducing the costs of heating and cooling inside buildings. The first one was the German company FLACHGLAS, in 1975. They first tried silver as the reflecting layer but due to various problems went back to gold layers [41]. Moreover, the gold layer embedded in BiO_x films gave a green tint in transmission, that was deemed too unpleasant by the market which was still relying on air-insulated panes using only clear glass. The next challenge was therefore to find a color-neutral low-emissivity stack. The solution was found in the 1980s when it was demonstrated that silver (Ag), rather than gold, embedded in an asymmetrical configuration (that is, dielectrics of different thicknesses) could achieve the same infrared heat rejecting performance while possessing color neutrality [41, 42]. The first proposed stack was $SnO_2/Ag/NiCr/SnO_2$ coated on glass. The

nickel-chromium (NiCr) layer was introduced as a sacrificial layer which is essential to protect the Ag film from oxidation during the deposition process. Reaching this color-neutral, high transmittance low-emissivity coating was a milestone in the glazing industry and set the trend for the subsequent decades. Since then, more than 100 in-line magnetron coaters are operated worldwide to produce more than 500 million square-meters of coated low-emissivity glass every year.

Since the shift from gold to silver and the use of an asymmetrical design of the low-e coatings, challenges other than color neutrality are still present. Among these challenges we can mention long-term durability of the stack, the degradation of silver during the deposition process, the effect of heat on the mechanical and optical properties of the films in tempered glass, angular selectivity of double and triple silver coatings, inhibiting island growth during silver deposition to obtain ultra-thin continuous silver films, and many more. Nevertheless, silver-based low-emissivity glazing are still the most widespread technology for energy saving as they offer performance and reliability that other emerging or established technologies do not yet possess.

2.2 Solar Heat Control Coatings

As we have previously mentioned, the principal function of a low-e stack is to transmit a high portion of the visible spectrum while rejecting the near-infrared radiation. It can be thought of as a high-pass filter where the cut-off frequency is determined by the plasma frequency of the thin metallic film and the thicknesses of the dielectric layers. The amount of solar radiation transmitted through the glass, $T_{sol}(\theta, \lambda)$ can be expressed by [43]:

$$T_{sol}(\theta, \lambda) = \frac{\int_{\lambda=300}^{2500} T(\theta, \lambda) S_{sol}(\theta, \lambda) \, d\lambda}{\int_{\lambda=300}^{2500} S_{sol}(\theta, \lambda) \, d\lambda} \tag{2.3}$$

where $T(\theta, \lambda)$ is the spectral transmittance and $S_{sol}(\theta, \lambda)$ the spectral distribution of solar radiation at sea level. The T_{sol} can be as low as 0.14 for a single layer silver, 0.11 for a double-silver coating, and 0.03 for a triple-silver coating [44]. These coatings can provide substantial energy saving compared to simple float glass which has a T_{sol} value of 0.85. Float glass is highly absorbent in the infrared region above 4 µm and therefore highly emissive in the same region. Therefore, most of the absorbed radiation (both from the incident solar and room ambient radiation) inside the glass

is re-emitted equally in all direction. We saw in eq.2.3 how $\varepsilon(\lambda, T)$ was necessary to calculate the radiative heat emitted from a surface. The emissivity can be obtained using the following equation:

$$\varepsilon(\lambda, T) = 1 - \frac{\int_0^\infty R(\lambda) P_b(\lambda, T_b) d\lambda}{\int_0^\infty P_b(\lambda, T) \, d\lambda} \tag{2.4}$$

where $R(\lambda)$ is the reflectivity and $P_b(\lambda, T_b)$ is the Planck' distribution for blackbody radiation at temperature T_b, given by [45]:

$$P_b(\lambda, T_b) = \frac{8\pi hc}{\lambda^5 (e^{hc/(\lambda k_B T_b)} - 1)} \tag{2.5}$$

The emissivity of soda lime glass has been measured to be 0.87 [46] and that of a silver film to be 0.02 [47]. In addition to the solar heat directly transmitted through the window, the ambient temperature inside the room also plays a role in the heating energy balance by radiating in the mid-infrared (with the blackbody radiation distribution centered at 9 μm at room-temperature). The glass substrate is highly absorbing at those wavelengths and therefore it is highly emissive in that region. We saw from Kirchhoff's law (eq.2.2) that a body at thermal equilibrium will radiate an amount of energy that it has absorbed. Since the absorption is isotropic, the re-emitted radiation is equal in every direction. However, the silver layer that prevents a portion of the near-infrared to be transmitted inside the room from the outside will also prevent the ambient heat to leave the interior by fully reflecting it back inside.

The metric for the performance assessment for energy saving is the Solar Heat Gain Coefficient (SHGC), also known as the Solar Factor (SF), given by [48]:

$$SHGC(\theta, \lambda) = T_{sol}(\theta, \lambda) + \sum_i F_i \cdot \alpha(\theta, \lambda)_i \tag{2.6}$$

where F is a fraction of the heat re-emitted inside the room and $\alpha(\theta, \lambda)$, the solar absorption of the coated glass. This absorbed emission is re-radiated in all directions, but due to geometrical factors and possible thin film interactions, only a fraction of the light reaches the interior. This fraction of re-emitted light (F in eq. 2.6) has been evaluated to 0.46 for a silver-coated glass pane [49]. In presence of multiple glazing units, the expression $F_i \cdot \alpha(\theta, \lambda)_i$ is summed over all glass panes. The

$SHGC$ value can be as low as 0.42 for a single layer silver, 0.18 for a double-silver coating, and 0.11 for a triple-silver coating [44].

This heat-trapping effect is beneficial in colder regions where we would aim for a higher SHGC to let more solar radiation throughout the day and benefit from the heat-trapping during the night. In warmer climates, a glazing unit with a low SHGC is preferred to limit the amount of solar radiation passing through the window during the day. However, even for a low SHGC, the heat trapping effect still occurs but the overall heat gain is greatly reduced compared to clear glass [50]. Like the solar transmittance, the visible transparency of a window pane is quantified through the T_{vis} coefficient, given by

$$T_{vis}(\lambda) = \frac{\int_{\lambda=380}^{780} T(\lambda) D_{65}(\lambda) V_{ph}(\lambda) \Delta \lambda}{\int_{\lambda=380}^{780} D_{65}(\lambda) V_{ph}(\lambda) \Delta \lambda} \tag{2.7}$$

where $T(\lambda)$ is the spectral transmittance, $D_{65}(\lambda)$ is the relative spectral distribution of illuminant $D65$ (given in Appendix A.1), and $V_{ph}(\lambda)$ is the spectral luminous efficiency for photopic vision. T_{vis} for clear (uncoated) glass is 0.89, and for a low-emissivity coating it can be as high as 0.86, denoting that we are able to achieve the same levels of visual transparency using a low-emissivity coating.

Figure 2.2 shows a simplified schematic of the various interactions between the solar radiation and the subsequent radiative heating pathways for a coated pane. The incident solar radiation undergoes multiple partial transmission and reflection at the interface of each of the thin films and the glass substrate. The sum over all partially reflected light is denoted by R_{sol}. The solar radiation transmitted through the coating is also transmitted through the glass substrate where a portion of near-infrared radiation is absorbed (A_{sol}). The radiation transmitted through the glazing unit (substrate + coating) is denoted by T_{sol}. The ambient radiative heat is denoted by Q_{amb} and the re-emitted heat by Q_{em}.
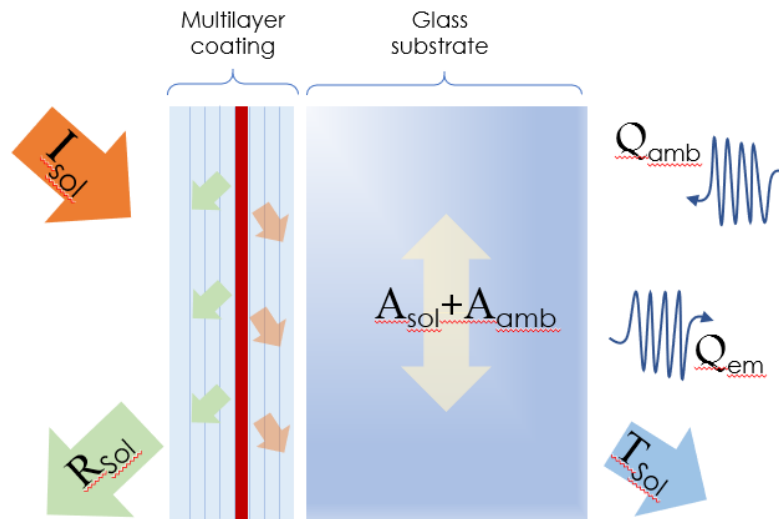
Figure 2.2 : Schematic of different radiative heating pathways. The solar irradiance (I_{sol}) is divided into R_{sol}, T_{sol} and A_{sol} according to the amount reflected, transmitted and absorbed by the glazing unit (multilayer + glass substrate). The ambient heat Q_{amb} originating from the blackbody radiation emanating from inside the room is absorbed by the glass substrate (A_{amb}), in addition to some of the transmitted solar infrared radiation. This absorbed radiation is re-emitted inside the room (Q_{em}) and contributes to the overall heat balance.

2.3 State of the art glazing units

Limiting the incoming solar radiation is the main role of an energy saving glazing unit. Besides leading to substantial energy savings, achieving a lower SHGC can also be a matter of increased health and comfort [51, 52]. Maximizing the incoming natural sunlight reduces the need to use artificial lighting (and hence reduce the electricity consumption), but too much lighting and glare over long periods of time can be a cause of visual discomfort and create sub-optimal working conditions [53, 54].

Besides low-emissivity coatings, many other strategies are available to reduce solar heat gain. In this section we will give an overview of two other technologies that could one day replace the low-emissivity glazing as the most produced eco-energetic glazing worldwide.

2.3.1 Electrochromic coatings

In an electrochromic device, an electrical potential applied between two electrodes drives a flow of ions from a reservoir (generally hydrogen (H^+) or lithium (Li^+) ions) to an active layer where an intermediate phase is formed [55-57]. This intermediate phase absorbs light in the visible range and hence limits the transit of light through the glass. One very important aspect of an electrochromic device is its ability to change from a transparent to an absorbing state by applying the reverse potential and extracting the ions from the intermediate phase layer. This operation must be achievable over a few thousand cycles in order to have a satisfactory product lifetime. Figure 2.3 shows the transmission curves of a tungsten oxide based electrochromic device in the bleached and coloured state.

One great advantage of an electrochromic layer is that it possesses intermediate absorbing states that are controlled by the ion insertion into the electrochromic layer, giving the user total control of the amount of radiation getting inside the room. Moreover, in terms of comfort and well-being, it has been demonstrated that an electrochromic device is superior to a mechanical blind or curtains as it doesn't physically separate the user from the exterior world [51, 58, 59].
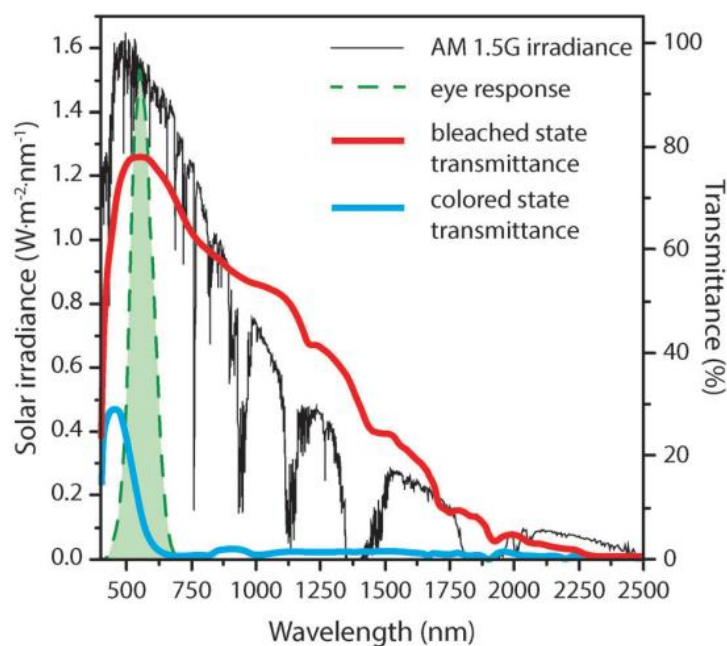
Figure 2.3 : Solar spectrum depicted alongside the photopic response of the human eye. The transmittance curves for a tungsten oxide based electrochromic are shown. Modified from [60]

From an energetic standpoint, the glazing requires an electrical circuit in order to apply the potential, but only to insert or extract the ions. Once the insertion or extraction is completed, the glazing doesn't require an electrical potential to maintain the fully colored, bleached or intermediate state. Figure 2.4 shows a schematic for a typical electrochromic device. The transparent electrode is usually tin-doped indium oxide (In_2O_3:Sn, or ITO) but it can also be replaced by fluorine-doped indium oxide (FTO) or aluminum-doped zinc oxide (AZO). A typical material for the electrochromic layer is tungsten oxide (WO_3), which is well known to form an opaque layer in the presence of H^+ (in a solid-state device) or Li^+ (using a liquid electrolyte membrane), forming H_xWO_3 or Li_xWO_3 bronzes.
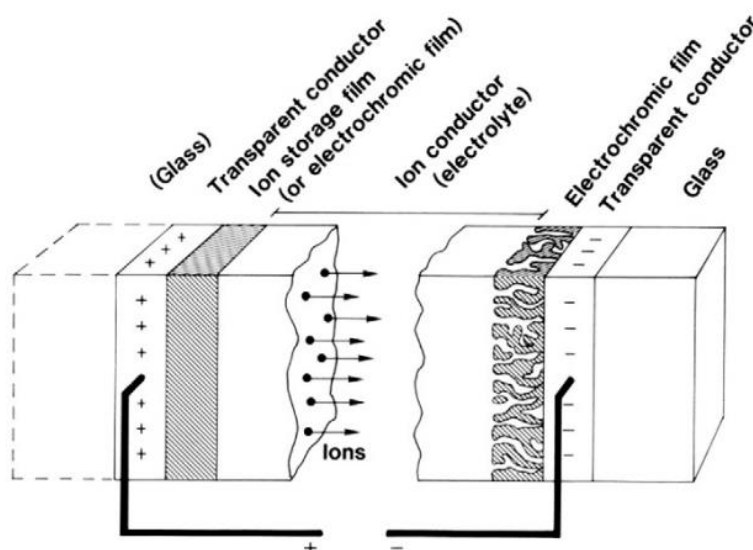
Figure 2.4: Electrochromic device configuration. Reproduced with permission from [61].

The charge insertion (ions and electrons) creates additional energy levels in the valence band of the newly formed compound that absorb the incident visible light [62]. However, the repeated ion insertion and removal cycles can leave behind trapped charges at the interface. It has been recently demonstrated that these charges can be removed by a galvanostatic device to apply a constant loading current [63, 64], providing a longer lifetime to the electrochromic stack.

The substrate can either be float glass, in which case the electrochromic device is coated directly on the glass pane, or it can be made of polymer, in which case the electrochromic device is produced using roll-to-roll coating technology and the film can be applied directly on glass [65]. It has been demonstrated that the durability of WO_3 coatings can be increased by changing the film

structure to a nanoporous, nanocrystalline layer [66], which interestingly also influences its ionic and electric conductivity [67].

For a commercial solid-state electrochromic device, the SHGC value can be as low as 0.1 with a T_{vis} of 2% (in a fully colored state), and a SHGC value as high as 0.47 with a T_{vis} of 62% [55]. For comparative purposes, a triple-silver low-e glass pane can achieve a SHGC of 0.3 with a T_{vis} of 66%, and for clear glass a SHGC of 0.85 and a T_{vis} of 89% [68].

It has recently been demonstrated that one could also modulate the near-infrared spectrum of the light by capacitively charging ITO nanoparticles [69]. Unlike ion insertion inside WO_3 films, charge accumulation around the ITO nanocrystals interacts with the localized surface plasmons which affects the response in the near-infrared region. This idea was later exploited to create NbO_x films doped with ITO nanocrystals [70, 71]. The films would benefit both from visible modulation following Li^+ ions insertion and the infrared modulation of the ITO nanocrystals. The confinement of light in the near-infrared region has also been shown with monoclinic tungsten oxide (m-WO_3) nanowires which exhibit a strong localized surface plasmon [72, 73]. When incorporated inside an electrochromic film, such as NbO_x, these nanowire-based devices are absorbing in both the visible and near-infrared regions. The latest research on active coatings points toward the development of these 'dual-band' electrochromic devices where the user can regulate both the visible and the infrared portions of the incoming radiation, and it certainly represents a promising future for active/smart coating technologies [58, 74].

2.3.2   Thermochromic coating

An alternative active coating technology that can regulate the SHGC of a glazing unit is the well-established vanadium dioxide (VO_2) coating. This material is known to undergo a phase transition from monoclinic phase to rutile phase at a critical temperature T_c which changes its optical and electrical properties from a semiconductor to a metal. A great advantage of a VO_2 based thermochromic coating is the ability for the glazing to transform from a neutral state to a low-e state above the critical temperature. Also, in contrast to the electrochromic glazing, the VO_2 coating can in principle operate a free-standing layer and does not require additional films.

However, a few challenges must be addressed before VO_2 based thermochromic coatings become deployed on a large scale, namely

- A transition temperature within 10-15° C of ambient temperature,
- A high T_{vis} in both states, as the VO_2 film has a small optical band-gap and absorbs in the visible with a yellowish tint,
- Increase the difference in the solar heat gain coefficient between the two phases.

Many solutions have been proposed to address the challenges faced by the VO_2-based thermochromic coatings. Metal-dopants inclusions using transition metals have shown ability to reduce T_c. This occurs when an additional electron from the dopant is added to the new vanadium phase ($M_xV_{1-x}O_2$) d-band which facilitates the transition to the metallic state [75]. Metallic dopants known to reduce T_c are cerium, molybdenum, silicon and tungsten. A T_c close to room temperature and even below can be achieved with a tungsten doping concentration of 1-2% [76]. One drawback with the doping strategy is that, as the material gains a metallic character with increasing doping concentration, the difference in the SHGC from the two phases below and above T_c decreases, and the layer loses its modulating properties. Figure 2.5 shows the transmission spectra for a $W_xV_{1-x}O_2$ (x=0.0098) with a T_c close to 35 °C.
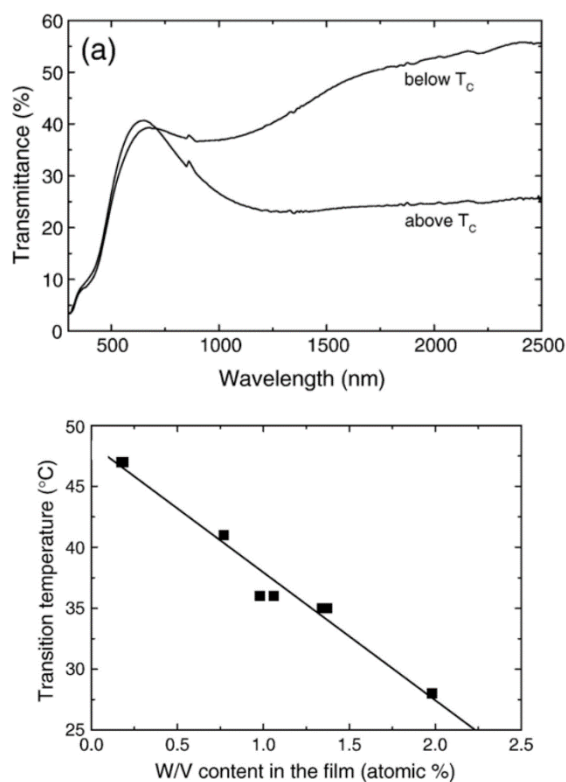
Figure 2.5: (top) Transmission spectra above and below T_c for a $W_{0.00098}V_{0.9902}O_2$ film (bottom) transition temperature as a function of W dopant in the VO_2 film. Modified from [77].

Due to a relatively small bandgap (around 1.75 eV), undoped VO_2 absorbs light in the visible region which gives the films an unpleasant yellowish color [78]. It is possible to diminish the amount of light absorbed by reducing the film's thickness, however, the thermochromic performance by phase transformation strongly depends on the film thickness. Once again, it is possible to change the optical bandgap of the VO_2 film by doping it with metals such as aluminum [79], manganese [80-83] and zinc [78]. Figure 2.6 shows the increase of T_{vis} as a function of Mg-dopant inclusion.
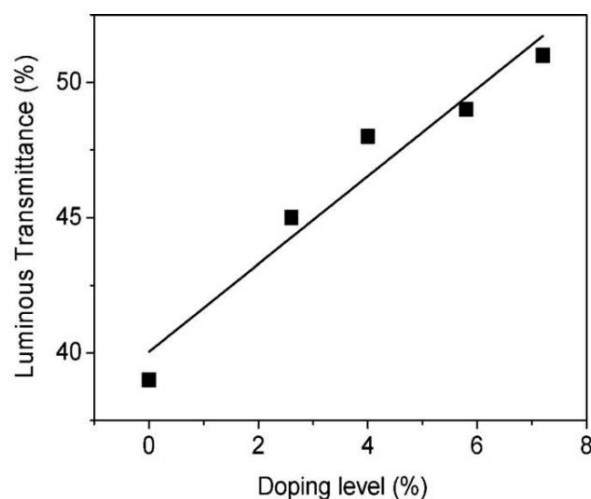
Figure 2.6 : Luminuous transmittance of $Mg_xV_{1-x}O_2$ films as a function of Mg doping concentration. Reproduced with permission from [83].

With $W_xV_{1-x}O_2$ films, one must be careful that the addition of dopant does not alter the thermochromic properties of the film, and one can achieve a compromise between high T_{vis}, low T_{sol} following the film's phase change, and T_c in the vicinity of the room temperature. The most promising avenue for thermochromic coatings today appears to be nanostructured VO_2 films, and embedded VO_2 nanoparticles [82, 84]. It has been demonstrated that spherical VO_2 core/shell nanoparticles (VO_2 core) can exhibit higher change in T_{sol} following phase transformation as well as generally higher T_{vis} when embedded inside a shell of SiO_2 or TiO_2 [85, 86]. Moreover, similar to the doped VO_2 films, it has been shown that Mg-doped VO_2 nanoparticles possess a lower T_c [87]. An interesting concept employing VO_2 nanoparticles alongside TiN nanoparticles was developed to lower T_c using the plasmonic absorption and local heating by the TiN nanoparticles to bring the film's temperature closer to T_c [88]. Using these plasmonic nanoparticles can be envisioned in order to also alter the visible optical properties of VO_2 films and to obtain a more pleasant film color. Additionally, it has been demonstrated that combining VO_2 films with a single, thin Ag layer enhances the thermochromic properties of the stack and improved overall energy saving performances [89].

As we have seen throughout this chapter, the purpose of the different types of glazing technologies is to reduce the effect of the incoming solar radiation, even when drastically different operating principles are at play. The strength of thin film technologies also lies in combining various types

of layers for added multifunctional characteristics or alter the nanoscale microstructure to bring in new or enhanced properties, as we saw in various examples. In that regard, other thin film-based technologies pertaining to energy saving could in principle be incorporated in one glazing unit, such as a semi-transparent plastic solar cell [90] or a perovskite solar cell exhibiting thermochromism, going from a transparent state to a direct band-gap solar cell [91]. Following the recent research trends, it seems certain that the future of glazing lies in nanostructured, multilayered, and multifunctional stacks. In the following chapters, we will describe the deposition techniques and processes leading to the desired thin film growth to obtain these layers.

CHAPTER 3   THIN FILMS FOR ARCHITECTURAL GLAZING

3.1 Foreword

The science and technology of thin films comprises all aspects related to the growth and properties of thin films as well as their functionalities in a multi-layer stack. The study of thin film properties at various scales is led and stimulated by the progress and development of new and existing deposition techniques and in-depth understanding of the growth process. This chapter will cover the various steps of thin film deposition and the physical properties arising from the growth process. We will first give an overview of plasma-based deposition principles for thin films. Then, we will see how the deposition parameters can impact the growth process on the atomic scale to understand physical properties of optical thin films.

3.2   Sputter deposition

To meet the demand for vacuum glazing in the architectural sector, today's deposition systems must be adapted to coat float glass substrates with an annual uptime of 6000 hours [92]. This means that the fabrication process must assure silver films of 8-12 nm and numerous other layers with a few angstroms' uniformity over large glass panes 6 x 3.2 meters in size. The thin films constituting a typical transparent low-emissivity device are typically not thicker than a few tens of angstroms to a few tens of nanometers. Therefore, a deposition technique that guarantees uniform deposition rate for different types of materials at the nanoscale must be used.

The coating technologies capable of this feat are grouped under the appellation of physical vapour deposition (PVD) techniques. These processes are based on the evaporation or sputtering of a target material under vacuum (10^{-3} to 10^{-10} Torr, typically) to reduce ambient contamination of deposited thin films. In a PVD process, vaporized material from a solid target is transported through a vacuum (or plasma) environment and condenses into a thin film on a substrate placed inside the process chamber. In a plasma based PVD process, charge carrying particles and other reactive species are involved in the deposition process, thin film growth and other surface phenomena. These charged particles react collectively to electromagnetic fields in various configurations used for target

sputtering, film densification, etching or for surface cleaning and surface modification. In this section, we will give an overview of plasma properties, the magnetron sputtering configuration as well as surface phenomena occurring in the presence of a plasma.

3.2.1 Plasma properties

A plasma can be defined as a collection of charged species (electrons and ions) displaying a collective behaviour. Inside a process chamber, the plasma can be ignited using a remote source (electrodeless plasma) or using a series of electrodes. We first investigate the plasma characteristics of the DC diode configuration, where a DC voltage is applied between two electrodes in presence of a background gas. The plasma characteristics of more practical and efficient sputtering techniques such as radiofrequency (RF) magnetron configuration can then be well understood from these principles.

To ignite the plasma, an inert gas, usually Argon (Ar), is initially introduced inside the deposition chamber. A negative potential applied at the cathode (the target) will cause any stray electrons to acquire kinetic energy. If an electron acquires enough kinetic energy to ionize a neutral gas atom, a positive ion is created, and an additional electron is emitted:

$$e^- + A = A^+ + 2e^- \tag{3.1}$$

The creation of an additional electron will contribute to this ionization cycle. The plasma generated in the DC diode configuration (also known as a glow discharge plasma) is a low-pressure gas (in the range of 10-100 mtorr) [93]. At pressures below, electron-atom collisions rarify, hindering the ionization cycle, and sustaining the plasma becomes more difficult, while at higher pressures, collisions become too frequent which prevents the electrons from acquiring enough kinetic energy. For the practical range of pressure that we have mentioned, a voltage of a few hundreds to a thousand volts is enough to sustain the plasma.

An important property of the plasma is its charge neutrality on macroscopic scales, meaning that the number of negatively charged electrons is approximately equal to the number of positively charged ions. In such plasma, the thermal mobility of electrons and ions can be quite different due to their mass difference and their respective velocities can differ by a few orders of magnitude. Indeed, the electron energy has a typical range of 1-10 eV, while ions and neutrals have energies

close to 0.04 and 0.02 eV, respectively [94]. Finally, charged species inside the plasma constitute only a small fraction of the neutral atoms present inside the plasma (typically between 10^{-1} and 10^{-5}). At a low-pressure end of 10 mtorr, the gas density can be estimated to 3×10^{20} m^{-3}, for which a reported ionization fraction of 10^{-4} yields an electron density in the range of 10^{16} m^{-3}.

It can be demonstrated that in the presence of an important collection of charged species, the electrostatic field $\Phi(r)$ (over a distance r) of individual charges is damped exponentially by a factor $\frac{r}{\lambda_D}$ where λ_D is called the Debye' length, i.e.,

$$\Phi(r) = \frac{1}{4\pi\varepsilon_0}\frac{q_e}{r}e^{\left(\frac{-r}{\lambda_D}\right)} \tag{3.2}$$

where ε_0 is the free space permittivity and q_e is the elementary electric charge. Debye's length λ_D is given by[95]

$$\lambda_D = \sqrt{\frac{\varepsilon_0 k_b T_e}{n_e q_e^2}} \tag{3.3}$$

for negligible ion velocities, where T_e is the electron temperature and n_e the electrons density. In other words, the electrical field of individual charges is effectively screened outside a sphere of radius λ_D, and the plasma is said to be 'quasi'-neutral if the number of particles inside the plasma is large compared to the number of charged species inside the Debye' sphere ($N \gg \frac{4}{3}\pi\lambda_D{}^3 n_e$).

For electron temperatures T_e in the range of 1-10 eV and electron densities n_e between 10^{16}-10^{17} m^{-3}, λ_D can be estimated between 0.2 and 0.02 mm. On scales in the order of λ_D, local perturbations can occur but are quickly compensated for by fast electron displacements. This generates an oscillating motion known as the plasma frequency. The plasma frequency ω_p scales with $n_e{}^{1/2}$ and is another main characteristic of the plasma:

$$\omega_p = \sqrt{\frac{n_e(q_e)^2}{\varepsilon_0 m_e}} \tag{3.4}$$

where m_e is the electron mass. This collective motion will shield all applied electric fields at frequencies below ω_p, and most of the local charge interactions occur on time scales in the order of $\omega_p{}^{-1}$.

Electrons inside the plasma have energies in the range of molecular excitation or atomic bonding, therefore a surface in contact with the plasma or the background gas molecules are exposed to a high degree of chemical activity. The constant motion of electrons leads to frequent collision with neutral gas molecules which cause the generation of excited states that lead to intense glowing due to radiative relaxation. The brightest region in the plasma is where the excitation through collisions is the most frequent. Depending on the gas molecules present inside the chamber, radiation can be emitted in the visible as well as the UV. Therefore, one must be careful to not expose photosensitive material directly to the plasma to avoid sustaining damage.

A plasma generated inside the process chamber is confined by the chamber's boundaries and develops regions with varying potential. A surface in contact with the plasma will rapidly charge negatively due to fast-moving electrons inside the plasma [94]. Electrons leaving the plasma at a higher rate than the ions will create an increase in the net positive charge inside the plasma. Eventually, the positive charge will prevent further electron loss to the boundaries and reach an equilibrium between the plasma potential and the boundaries. This region of voltage drop is labeled the sheath and has dimension of several Debye' length. Figure 3.1 shows schematically sheath formation at the boundary of the plasma. Therefore, to sustain plasma in the DC diode configuration, there must be a continuous electrons and ion charge generation to account for lost charges at boundaries and inside the plasma as well. The potential build-up at the boundary (V_b) is a few volts lower than the plasma potential V_p, due to the negative charge accumulation at the boundary. Typical sputtering discharges are excited in the DC, pulsed-DC (until about several hundreds of kHz), and RF (13.56 MHz) modes.
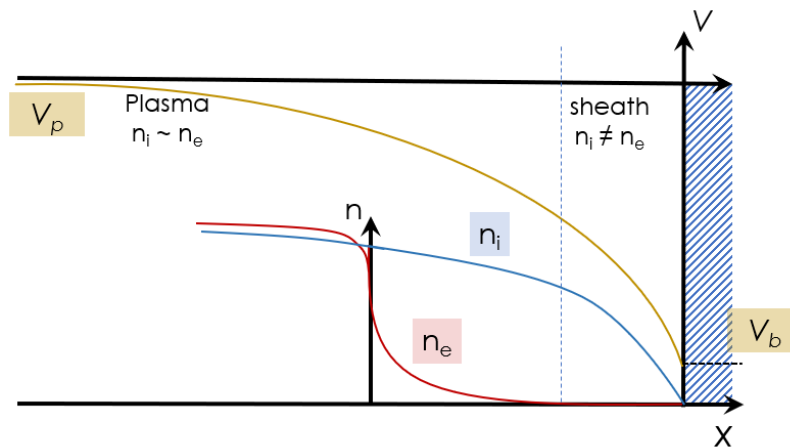
Figure 3.1 : Schematic of plasma sheath formation at the boundary.

3.2.2 Diode sputtering

3.2.2.1 DC sputtering

The DC voltage applied to the cathode to first ignite the plasma will attract positive ions generated by the ionization cycle. Positive ions accelerated toward the cathode will cause sputtering through momentum transfer to the target surface. Moreover, impact of the ions on the surface causes secondary electron emission which get accelerated away from the cathode and contribute to the ionization cycle. Therefore, the sputtering process helps to maintain the plasma discharge by continuous secondary electron emission from the target material. Similar to the plasma sheath created at the boundaries of a plasma, charge separation due to the negative voltage applied to the cathode creates a region characterized by a potential drop across its length, labeled cathode sheath. Most of the energy acquired by the ions occurs inside this region, where they are accelerated towards the cathode to initiate the sputtering process.

The measure of the removal rate of atoms from the target's surface is labeled the sputter yield and is calculated by the ratio of sputtered atoms to incident number of ions. Since atoms are removed from the target by energy transfer from the incoming ions, the sputtering yield depends on the mass and velocity of incoming ions generated inside the plasma, the mass of the target atoms, the surface

binding energy and the interaction cross-section [93]. Depending on the energy of the incoming ion and the surface binding energy of the target, surface atoms can be ejected after a single collision (a 'knock-on' event) close to the target surface (for lower energies) or trigger a linear series of collisions (a linear cascade) at higher energy, which leads to a single or multiple atoms being released, as shown schematically on Figure 3.2.
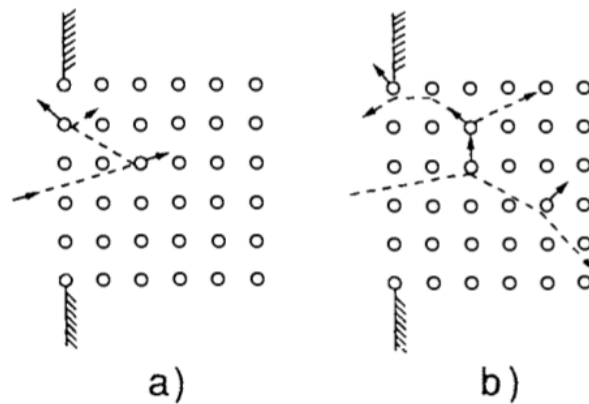
Figure 3.2 : (a) Single collision (knock-out) and (b) Multiple collisions events happening during sputtering. Modified from [93].

As a general estimate, ions with only a few eV will simply be reflected or adsorbed on the cathode. It's only at energies of tens of eV up to a few keV that the sputtering process starts as shown in Figure 3.3.
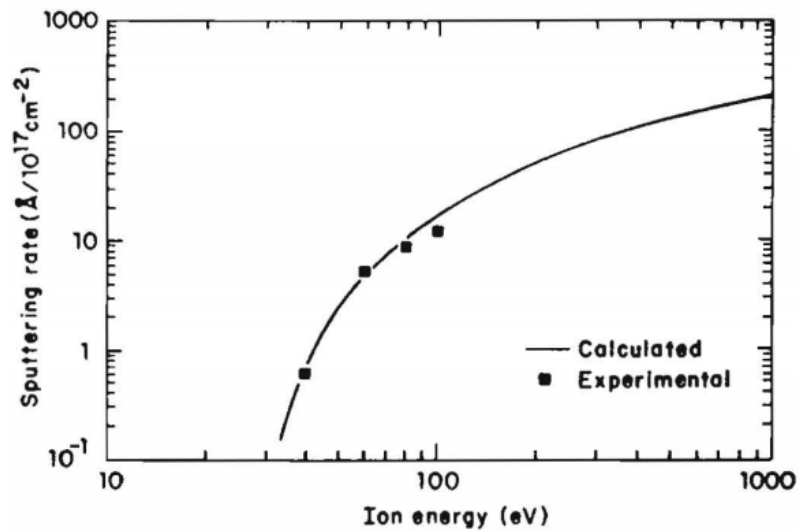
Figure 3.3 Sputtering rate of SiO_2 vs Ar+ ion energy. Reproduced with permission from [96]

An increase in the sputtering yield does not necessarily translate to an increase in film formation rate on the substrate. At too high pressures, sputtered atoms have an increased chance to undergo collisions with background gas atoms and ions, which will decrease the deposition rate. In the DC diode configuration, secondary electron generation is essential to maintain ionization cycle and keep the plasma charge neutrality by accounting for the charges lost at the boundaries. Therefore, higher pressures are required to sustain plasma discharge.

3.2.2.2 RF sputtering

One way to bypass the need of high working pressures is by using an AC power supply to generate a voltage difference at the electrodes. The operating principle remains similar to the DC diode configuration, with the difference that the polarity of the applied potential varies with time, changing a few properties of the plasma. First, at sufficiently high frequencies (at RF frequencies above 1 MHz), electrons absorb most of the applied power as ions can't follow the alternating cycles. The changing polarity between the cathode (the sputtering target) and the anode (the substrate and chamber wall) means that electrons are less likely to be lost to the wall boundaries, as they are repelled every half-cycle. Correspondingly, as electrons oscillates between the chamber walls and the cathode, the probability of ionizing a neutral gas atom increases, and secondary electron generation at the cathode is not a requirement. Therefore, the plasma can be sustained at

lower pressure, increasing the mean-free-path of the sputtered species, which leads to increased deposition rate, higher energies of arrival of sputtered atoms and in general denser films.

The use of RF frequencies for sputtering (the standard frequency is set to 13.56 MHz) implies that the plasma has a resistance and reactance component to which the power supply needs to be matched by a series of capacitors and inductors. It is common practice to place a capacitor in series with the cathode to allow the formation of DC bias. Since the electron mobility is much higher than the ion, during the positive half of the cycle, there is an excess electron current accumulating at the target compared to the ions during the negative half of the cycle (Figure 3.4a). The voltage is shifted to a lower potential due to negative charge accumulation so that the net current average over one cycle is zero (Figure 3.4b). The shift in potential is called the self-bias and is a characteristic of RF diode discharges. This self-bias acts as a DC voltage applied on the target which attracts positive ions generated inside the plasma for the sputtering process and allows for sputtering of both metallic and insulating targets (contrary to DC sputtering).
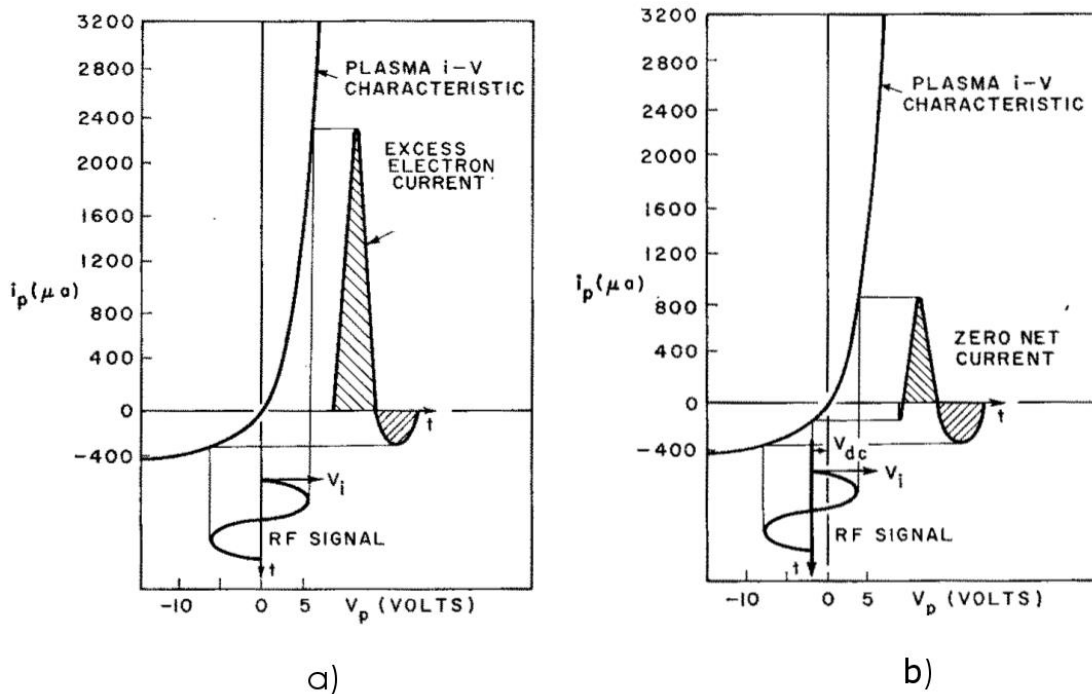
Figure 3.4 : Schematic of RF self-bias formation. Modified from [97]

3.2.2.3 Magnetron configuration

We saw that we can obtain higher charge densities in a plasma and operate at lower pressures (and hence obtain denser film formation) by supplying RF power to the target through a matching unit. Another path to increase the electron-ion collisions is to apply magnetic field lines parallel to the target surface with a permanent magnet (Figure 3.5). The magnetic field lines in combination with the electric field cause trapped electrons in the vicinity of the target to experience a spiraling, hopping motion and drift in a closed loop above the target surface, which increases the probability of electron-ion impact and creating an erosion track on the target [94].

The magnets configuration has a strong influence on electron confinement and hence plasma dynamics. In a 'balanced' configuration setup, similar magnets are placed below the target so that field lines are symmetrical above the target (Figure 3.5a). In this configuration, ion density is high near the target but very low at the substrate, which prevents ion generation near the substrate.
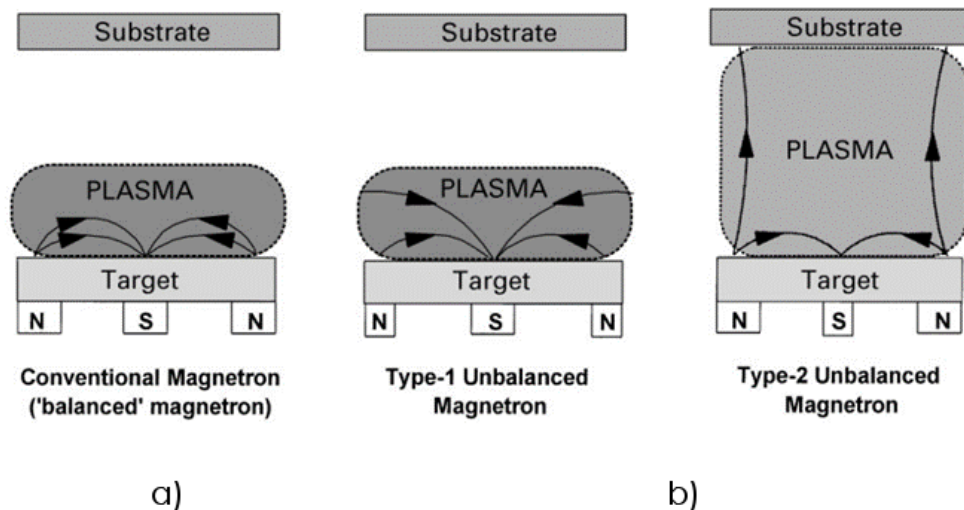
Figure 3.5 : Schematic of plasma confinement in a DC magnetron sputtering discharge with (a) balanced and (b) unbalanced magnetron configuration. Modified from [98].

By placing magnets of different strength, it is possible to obtain open field lines (Figure 3.5b) that allow some electrons to escape and ionise neutrals far away from the plasma. In this condition, it becomes possible to use an external applied potential on the substrate to bombard the surface, to influence the growth and properties of the deposited thin film.

When the electric and magnetic fields are properly configured, the discharge plasma is known to provide a highly uniform lateral density, yielding very uniform depositions over a few meters squared even when generated by very large cathodes [99], making sputtering a key process in the industrial sectors since many years.

3.2.3 Surface reactions

We saw how various diode configurations can be used to deposit metallic or dielectric thin films by means of controlling the plasma properties. To complete the discussion on sputter deposition of thin films, we will now describe the chemical reactions that occur inside the plasma. As we have already mentioned, the electrons inside the glow discharge have sufficient energy to ionize neutral gas atoms. They can also neutralize ions by recombination, molecule dissociation, bring atoms to excited states or modify surface states by electrostatic charging. Energetic ions can also influence the chemical state of other species through charge transfer. Therefore, we can see the plasma as an inhomogeneous medium where each constituent is physically and chemically affected by various processes.

One widespread deposition process is reactive sputtering, where the desired film is a compound (usually an oxide or a nitride) that is deposited from a single element target, such as TiN films from a Ti target or ZnO films from a Zn target. Many advantages can stem from deposition from a metallic target, namely:

- Elemental targets can be obtained with greater purities than compound targets.

- Metallic targets dissipate heat more efficiently to avoid damage to the target due to temperature increase from ionic bombardment.

- The film stoichiometry can be adjusted in a controlled manner.

- Deposition of insulating films at a high rate.

To do so, we insert a secondary gas (such as N_2 or O_2) at a partial pressure of the main Ar gas. Upon dissociation and/or ionization, the atomic gas can interact with the sputtered atoms inside the plasma or at the surface of the substrate, forming an oxide or a nitride compound. The final stoichiometry of the thin film is determined by the sputtering yield of the target and the partial

pressure of the secondary gas. Likewise, it is possible to obtain oxy-nitride films (SiO_xN_y, for example) at the desired stoichiometry by inserting both gases and carefully adjusting the deposition parameters.

The main drawback of reactive sputtering is target poisoning. As the reactive gas dissociates in the plasma, oxygen (or nitrogen) atoms and ions are generated alongside the argon ions and are accelerated toward the target. The surface becomes modified by an exterior oxide (or nitride) layer forms which decreases both the deposition rates and the ionic current flow to the target. If the process continues, increasingly higher power is needed to compensate for the decreased current flow and arcing can appear, which can damage the system. Eventually, it becomes impossible to sustain the plasma. One solution to avoid target poisoning is use of pulsed-DC generators, cycling between a high negative voltage and a low positive voltage with frequencies up to 100 kHz. The negative cycle is used to perform the sputtering whereas the positive cycle is used to bring the electrons to neutralize the surface and avoid charge build-up.

Finally, we saw in the previous section that the substrate can interact with species in the plasma such as electrons, affecting surface chemistry or dissociated reactive gas and ions produced close to the surface. These reactive species can be source of film contamination and have a strong impact on the film integrity. Figure 3.6 shows the *in-situ* monitoring of a 3 nm thick Ti film deposited by DC magnetron sputtering exposed to a plasma mixture of $Ar:N_2$ (1:6 ratio) at a working pressure of 10 mtorr. The change in optical properties come from the TiN film formation (as Ag does not form nitrogen compounds). Experimental details are given in section 4.3. We will see in Chapter 7 and 8 how these surface reactions can damage thin metallic film during deposition and how they can be exploited to create novel nanostructures.
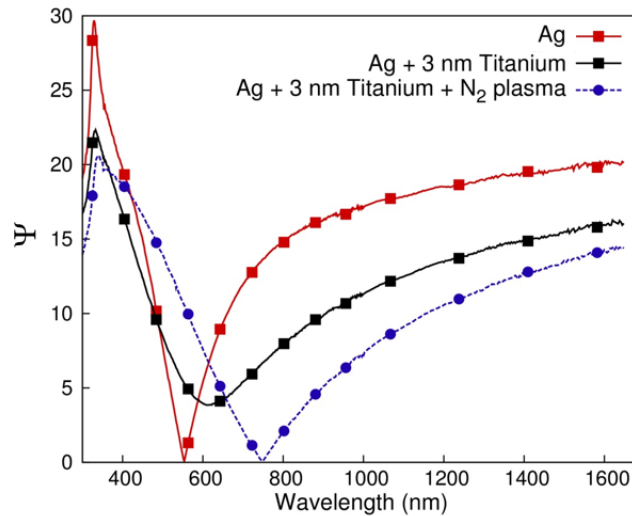
Figure 3.6 : In situ measurement of the optical properties of a Ti thin film after exposure to a plasma of Ar:N$_2$ measured in-situ

3.3 Thin film growth

The physical properties of thin films evolve during growth stages. As an example, we can mention the noble metals such as silver [100-102] and gold [103-105], which have plasmonic properties as nanoparticles (1-4 nm effective mass-thickness) and transparent electrodes when they form a thin film (8-20 nm) [106-109]. Therefore, to obtain desired properties for energy saving devices one must carefully control and monitor the thin film growth process. In this chapter, we will describe the early stages of growth and will see how we can influence the quality of resulting films regarding their desired properties.

3.3.1 Adatom adsorption and diffusion

Physical vapour processes involve the ejection of atoms from a source toward a substrate, and the very first steps of nucleation can be described as condensation of gas on a surface. In a laboratory setting, when using a high vacuum process chamber (ranging from $\times 10^{-6}$ to the $\times 10^{-10}$ torr), the sticking probability for an atom to condense on a surface applies to residual gases present inside the chamber or for atoms ejected from a source. When the sputtered atoms are in contact with the substrate, they first lose energy to phonons and stay on the surface in a highly vibrational level, away from the equilibrium binding position between the atom and the substrate. The atoms will

then gradually lose more energy to the surface vibrations and by lateral diffusion, until they reach lower energy levels and become adsorbed on the surface [110-118].

This very first stage of nucleation in PVD processes depends only on the temperature of incoming atoms and the temperature of the surface. When atoms reach the equilibrium energy level, they are said to be accommodated. This accommodation coefficient has been described as,

$$\alpha = \left| \frac{T_{in} - T_{ev}}{T_{in} - T_s} \right| \tag{3.5}$$

where T_{in} is the temperature of the incident atoms, T_{ev} the temperature of re-evaporation from the substrate and T_s the temperature of the substrate [119]. This coefficient measures how likely it is for atoms to reach thermal equilibrium with the substrate. If T_{ev} is much higher than T_c, the sputtered atoms are more likely to stick to the surface (large accommodation coefficient). On the contrary, if the T_c is much higher than T_{ev}, atoms are likely re-evaporated back and the accommodation coefficient is very small, meaning that very few atoms will condensate on the surface.

There are therefore two competing processes in the initial stage of nucleation, the accommodation of atoms on the surface on one hand and the re-evaporation on the other. As a result, we can define the likelihood of metal atoms to stick on the surface by a sticking coefficient β, defined as the ratio of the capture rate R_c on a surface over the arrival rate R_a of atoms [120]:

$$\beta = \frac{\#\ atoms\ adhering}{\#\ atoms\ arriving} \tag{3.6}$$

The capture rate R_c can be thought of as the number of atoms per unit time that have been accommodated on the surface and are in their equilibrium position on the substrate. The adhesion mechanism can be physical or chemical in nature. For a physisorption process, the attraction between the incoming neutral atoms and the surface is due to electrostatic forces, arising from the interactions between the long-range columbic attraction and short-range electronic repulsion. The bonding energy of two atoms can be expressed in the form of the Mie potential $\phi(r_{ij})$ [119]:

$$\phi\left(r_{ij}\right) = -\frac{\phi(r_0)}{(n-m)} \left[n \left(\frac{r_0}{r_{ij}} \right)^m - \left(\frac{r_0}{r_{ij}} \right)^n \right] \tag{3.7}$$

where n and m are integers, r_0 the equilibrium distance between the two atoms, for which $\frac{d\Phi}{dr_{ij}} = 0$.

In the case of the atom sticking on a surface, the potential felt is the sum of the potentials of each individual neighbouring atom,

$$\Phi_d = \sum_l \phi_l \tag{3.8}$$

or from dipole attractions (Van der Waals forces). In the case of chemisorption, there is an electron transfer process between the adsorbate and the surface. In both cases, attractive forces are characterized by the adhesion energy E_a. We will see later in Chapter 5 and Chapter 6 how the surface energy can be related to adhesion energy and how it governs the wettability of thin silver films.

To describe the initial nucleation process, we first neglect adatoms interactions and assume a homogeneous distribution of surface sites. It has been found experimentally that there is an average lifetime τ_e for which the adsorbed atoms can re-evaporate and can be expressed in terms of the thermodynamic quantity $\left[\frac{E_a}{k_B T_s}\right]$, where T_s is the temperature of the substrate. We use Arrhenius' equation to define the desorption rate R_e as

$$R_e = v_0 \, e^{\left\{-E_a/k_b T\right\}} \tag{3.9}$$

Experimentally, v_0 has been determined to correspond to values close to the frequency of lattice phonon vibration ($\sim 10^{-13}$ s). The average lifetime for an adsorbate on the surface is then given by [121]

$$\tau_e = \frac{1}{R_e} \tag{3.10}$$

For condensation to occur on a surface, R_a must be greater than R_e for a sticking coefficient β greater than 0. Moreover, we have seen that the desorption rate is related to the surface vibration frequency and therefore related to surface temperature. If we consider only the adhesion energy of an atom on the surface, for a low E_a and/or a high surface temperature the rate of re-evaporation R_e will be high.

Atoms impinging on the surface will always diffuse to some extent. In general, they will diffuse until they stick to the surface, re-evaporate, adhere to a previous adsorbate or collide with other diffusing atoms to form clusters. The mean diffusion rate R_d is a thermodynamic property, given by

$$R_d = v_D \, e^{\left\{-E_D/k_b T\right\}} \tag{3.11}$$

where v_D is the jump frequency of a diffusing atom to the nearest site and E_D the energy required for the atoms to move laterally on the surface [122]. The diffusion energy can be thought of as the potential that the atom has to overcome in order to move from one site to another. These sites can be described as periodically spaced regions of equipotentials (Figure 3.7a.). In other words, for a constant v_D, a significant lateral diffusion will be present if the energy of the impinging atoms is greater than E_D.

We distinguish three kinds of diffusion sources, namely intrinsic, kinks and terraces [123]. The intrinsic diffusion depends on the energy of impinging atoms and the activation energy for diffusion E_D and represents the lateral movement of atoms on a uniform surface. For low deposition rates and negligible adatoms interactions, the intrinsic diffusion can be expressed by the random walk process [124] where an atom adsorbed on the surface will randomly diffuse to neighbouring sites until it meets a cluster [125] or becomes a nucleation site. A more accurate picture of the potential energy variation in two dimensions is surface contour of equipotentials that are felt by the atoms that are adsorbed on the surface. Figure 3.7 shows a schematic of those contour in case of an ionic crystal [126].

Moreover, on real surfaces, defects that might be present will alter the diffusion process [127]. These surface defects and kinks become favourable nucleation sites for diffusing atoms because they require higher energy to surpass them (Figure 3.8). At very high substrate temperatures, the surface energy becomes so high that the diffusion atoms acquire enough energy to overcome defect barriers and terraces.
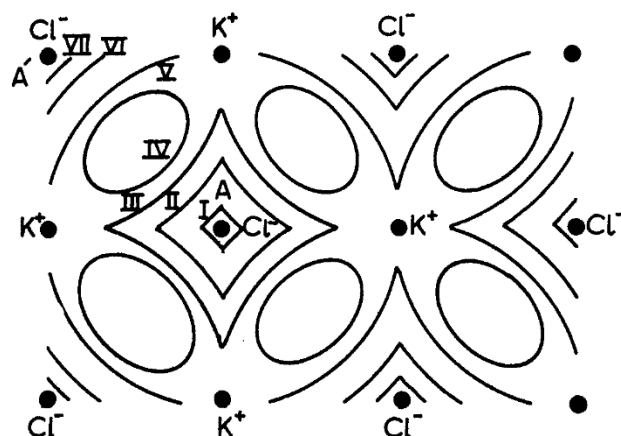
Figure 3.7 Equipotential contours for adsorption of argon on KCl. Modified from [119]

Moreover, clusters of atoms are mobile on a surface and they may join a bigger cluster over a long period of time even in absence of a deposition flux [111, 128-130]. This process is termed Ostwald ripening that is responsible for atomic rearrangement when the thin film growth is in the nucleation stage.
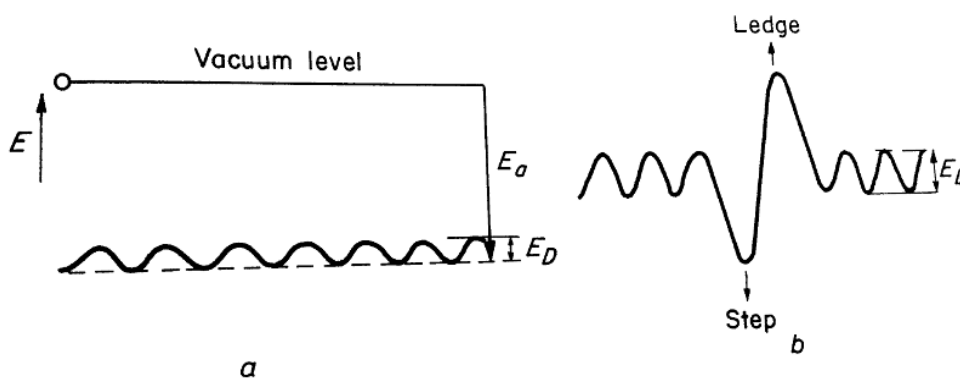
Figure 3.8 Potential energy distribution on (a) smooth surface, (b) around a step. Modified from [119]

3.3.2 Nucleation and capture rate

The atomistic approach to the nucleation process can become burdensome due the great numbers of surface phenomena that can affect the growth process. A simplified approach to describe the

nucleation process is by the use of an equation that describes the formation of nuclei as a function of the deposition time[124]:

$$\frac{dn_1}{dt} = R_a - {n_1}/{\tau_e}$$

(3.12)

Here n_1 is the number of single atom nuclei on the substrate and we assume that re-evaporation is the only means for nuclei to disappear. Integrating Eq.3.12 with the starting conditions $n_1 = 0$ and $t = 0$ yields

$$n_1 = R_a \tau_e \left[1 - e^{-t/\tau_e}\right]$$

(3.13)

The adsorption energy for silver atoms on a silicon oxide substrate has been estimated as 0.36 eV [131]. If we use this value to find τ_e using eqs. 5-6, we find 1.07×10^{-7} seconds for the average re-evaporation time. For any reasonable experimental time scale, $t \gg \tau_e$ so that equation 3.13 can be written [132] as:

$$n_1 = R_a \tau_e$$

(3.14)

However, in most cases, re-evaporation of atoms is not the sole mechanism for the loss of nuclei. A more complete nucleation rate model has been developed by Ozawa et al. [133] who assume that during the nucleation process, the adatoms on the surface can stick to a preferred site to form a nucleus, or by random collision of adatoms diffusing on the surface. Their model is given by:

$$\frac{dn}{dt} = \frac{dn_R}{dt} + \frac{dn_P}{dt} - \frac{dZ}{dt}$$

(3.15)

where $\frac{dn}{dt}$ is the rate of formation of clusters on the surface and $\frac{dn_R}{dt}$ and $\frac{dn_P}{dt}$ are the rates of formation due to random collisions and preferred site, respectively. The term $\frac{dZ}{dt}$ represents the rate of change of the surface coverage Z during the sputtering process. Naturally, for the formation of a thin film a full surface coverage is desirable. Therefore there is a time in the evaporation or sputtering process where the formation of nuclei on the surface slows down, comes to a halt, and decreases as the deposition continues [134]. Figure 3.9 shows a typical plot of the nucleus density on a surface as a function of deposition time. We see that the rate of formation becomes negative after a certain

deposition time. Therefore, when the term $\frac{dZ}{dt}$ outweighs the two other terms, the nucleation rate becomes negative and we reach the percolation threshold point.
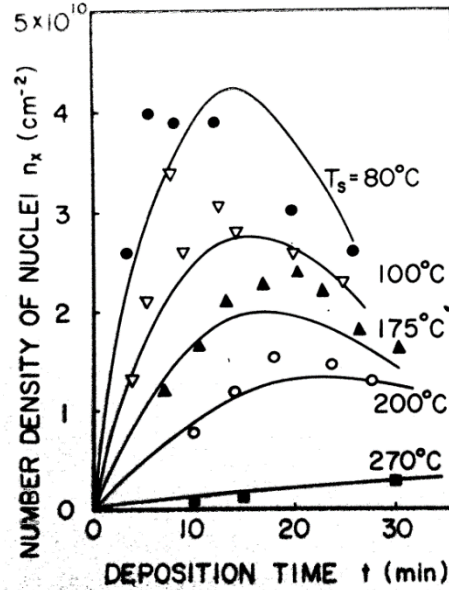
Figure 3.9 : The time variation of the number density of Pb nuclei deposited onto SiO_2 substrates for various temperatures; the data plots were obtained from electron micrographs. Reproduced with permission from [133].

The rate of change of the nucleation process provides a useful view for the growth process of metallic films. The atoms that first adhere to the surface undergo surface diffusion until they reach an energetically stable position, or a pre-existing nucleation site. As more atoms undergo this process, small clusters begin to form with island-like shape on the surface [135, 136]. The dimensions of the islands depend greatly on the ability of the incoming atoms to overcome kinks and terraces present on the surface. Eventually, the nucleation process gives way to coalescence and film formation through crystal growth and grain growth [137].

3.3.3 Coalescence and growth

With the definition of these new terms, we see that we can obtain a nucleation process if the re-evaporation rate R_e is negligible compared to R_a. In the case of a high surface diffusion rate R_d, nuclei will form across the sample and act as a sink for other atoms, and therefore grow in size as

more atoms diffuse on the surface [138]. The deposition process becomes a competition between nucleation sites formation and coalescence [139]. When the clusters of atoms reach a critical density, their numbers start to steadily decrease as they coalesce and reach the percolation threshold. This step is characterized by a steady increase of the surface coverage by the atoms. This surface coverage and subsequent growth will determine the final properties of the deposited thin film.

On the macroscopic level, the tendency of the growth mode has been described in terms of the surface free energy of the substrate (σ_s), of the interface (σ_i), and of the deposited layer (σ_l). The type of growth described previously has been described in the literature as the Volmer-Weber growth mode, where the island formation precedes the formation of a continuous layer. In this model, the surface energy inequality can be written as

$$\sigma_l > \sigma_s + \sigma_i \qquad (3.16)$$

meaning that the deposited layer will have a tendency to agglomerate rather than wet on the surface [140]. As described previously, this type of growth mode is also characterized by high diffusion rate and adatom mobility on the deposited surface. On the other hand, a layer by layer growth mode (Frank-van der Merwe growth mode), can be described by

$$\sigma_l < \sigma_s + \sigma_i \qquad (3.17)$$

meaning that the adatoms rather stick on the surface and have no tendencies to agglomerate. This mode of growth is represented by metal on metal or semiconductor on metal systems. Figure 3.10 shows a schematic for the Volmer-Weber growth mode.
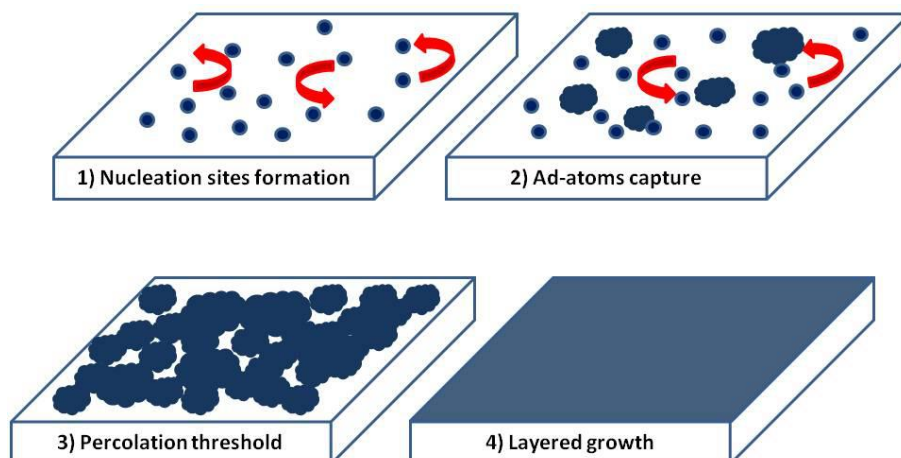
Figure 3.10 : Schematic representation of Volmer-Weber growth mode. The impinging atoms first create nucleation sites (1) that gradually form nano-islands (2). As the thin film grows, the islands formation converges to the percolation threshold (3) and finally a thin film is obtained (4)

For the sputtering technique, the microstructure resulting from the various growth models will vary depending on the process parameters, such as the working pressure, energy of arriving particles and substrate temperature. The influence of these parameters on the microstructure of the resulting thin film can be found in the literature under the appellation of the Structure Zone Model [141-143].

3.4 Thin film properties

Architectural glazing units require both dielectric and metal films to filter sunlight in an energy efficient manner. While performance of these glazing is based on the quality of the deposited film, the understanding of the physical phenomena responsible for the properties of the thin films is of great scientific interest and constitutes an active rea of research. Optical thin films are essential in the field of solar energy saving devices, where the modulation of the incoming solar radiation is made possible by the appropriate choice of the material. Evidently, interactions between electromagnetic waves and matter are the basis of the operation of such devices in relation to the amount of radiation reflected, transmitted and absorbed. In this section, we describe the theoretical development for the interaction of solar radiation with a thin silver film embedded between different dielectric layers.

3.4.1 Optical properties of dielectrics

The transit of an electromagnetic wave inside matter is governed by its interactions with the material. For dielectrics, the interactions arise from tightly bound electrons to the positive nucleus, making the dielectric a uniform distribution of induced dipoles made of the positive ion core and the bound electrons. The response of the dielectric to an external field is represented by the polarization vector $\vec{P}$, which for linear materials is proportional to the electric field strength $\vec{E}$ by the electric susceptibility χ:

$$\vec{P} = \varepsilon_0 \chi \vec{E} \tag{3.18}$$

and the displacement vector $\vec{D}$

$$\vec{D} = \varepsilon_0 \varepsilon_r \vec{E} \tag{3.19}$$

$$\varepsilon_r = 1 + \chi \tag{3.20}$$

where ε_r is the relative dielectric constant of the material. For dielectrics and in absence of external charges, we can set $\nabla \cdot D = 0$. We find the wave equations inside a dielectric:

$$\nabla^2 E = \mu_0 \varepsilon_0 \mu_r \varepsilon_r \frac{\partial^2 \vec{E}}{\partial^2 t} \tag{3.21}$$

where μ_r is the relative permeability of the material. The phase velocity given by

$$v_p = \frac{1}{\sqrt{\mu_0 \varepsilon_0 \mu_r \varepsilon_r}} = \frac{c}{\sqrt{\mu_r \varepsilon_r}} \tag{3.22}$$

This describes the fact that the propagation speed of an electromagnetic wave inside a dielectric is different from the propagation speed in vacuum c by a constant, arising from the presence of the atomic dipoles. The value by which the speed of propagation differs from the speed of light is the refractive index n, defined by:

$$n = \frac{c}{v} = \sqrt{\mu_r \varepsilon_r} \tag{3.23}$$

At optical frequencies and for non-magnetic materials we set $\mu_r = 1$. As we will see, the knowledge of the refractive index governs the optical modeling of thin film structures. In the

classical model, the absorption of light by a medium is explained as a coupling between the oscillation frequency of atomic cores and their bound electrons to the frequency of light. The polarization vector $\vec{P}$ responds to an external field $\vec{E}$ according to the dielectric function $\varepsilon_r(\omega)$, which depends on the frequency of the external field. All the light-matter interactions in this classical view can thus be obtained if we find an expression for the dielectric function. To do so, we will start by the equations of motions of bound electrons and ionic cores from a classical standpoint. In one dimension, the equation of motion of an electron inside the material under the influence of an external electric field $\vec{E}$ is given by:

$$m_0 \frac{d^2 x}{dt^2} + m_0 \gamma \frac{dx}{dt} + m_0 \omega_0 x^2 = -q_e \vec{E} \tag{3.24}$$

where the second term corresponds to the damping (slowing) of the electron of mass m_0 by γ (damping rate) and the third term the restoring force due to the ion core. We will express the electric field by the real part of the incoming electromagnetic field:

$$\vec{E} = \hat{\imath} R\{E_0 e^{-i\omega t}\} \tag{3.25}$$

where $\hat{\imath}$ is a particular direction of the field. We thus look for a solution for the displacement of the electron in the form of:

$$x(t) = \alpha_0 \hat{\imath} R\{e^{-i\omega t} e^{-\vartheta}\} \tag{3.26}$$

where ϑ is the phase constant to account for a delay between the oscillation of the electron and the field. Substituting equation 3.25 into equation 3.26, we obtain the following expression for the displacement of the electron:

$$X_0 = \frac{-q_e E_0}{m_0(\omega_0^2 - \omega - i\gamma\omega)} \tag{3.27}$$

The oscillation of the electron produces a dipole moment given by

$$p = -q_e X_0 \tag{3.28}$$

The overall polarization takes all N dipoles per unit volume, such that

$$P = Np \tag{3.29}$$

$$P = \frac{Nq_e{}^2}{m_0} \frac{1}{(\omega_0^2 - \omega - i\gamma\omega)} E_0 \tag{3.30}$$

Using eqs. 3.19, 3.20 and 3.30, we obtain the following relations:

$$\varepsilon_0\varepsilon_r\vec{E} = \varepsilon_0\vec{E} + \vec{P} \tag{3.31}$$

$$\varepsilon_0\varepsilon_r\vec{E} = \varepsilon_0\vec{E} + \frac{Nq_e{}^2}{m_0} \frac{1}{(\omega_0^2 - \omega - i\gamma\omega)} E_0 \tag{3.32}$$

$$\varepsilon_r(\omega) = 1 + \frac{Nq_e{}^2}{\varepsilon_0 m_0} \frac{1}{(\omega_0^2 - \omega - i\gamma\omega)} \tag{3.33}$$

The above equation is the resonant formula for Lorentz oscillators, with the real and imaginary parts given by:

$$\varepsilon_1(\omega) = 1 + \chi + \frac{Nq_e{}^2}{\varepsilon_0 m_0} \frac{\omega_0^2 - \omega^2}{(\omega_0^2 - \omega^2)^2 + (\gamma\omega)^2} \tag{3.34}$$

$$\varepsilon_2(\omega) = \frac{Nq_e{}^2}{\varepsilon_0 m_0} \frac{\gamma\omega}{(\omega_0^2 - \omega^2)^2 + (\gamma\omega)^2} \tag{3.35}$$

In the case of a medium having multiple resonances corresponding to the various excitation modes of the atoms, eq. 3.34 can be expressed as

$$\varepsilon_r(\omega) = 1 + \frac{Nq_e{}^2}{\varepsilon_0 m_0} \sum_l \frac{f_l}{(\omega_{0l}^2 - \omega - i\gamma_l\omega)} \tag{3.36}$$

where f_l represents the oscillator strength of each resonance. It can be shown that the complex part of the refractive index corresponds to the extinction (or absorption) inside the medium. For a plane wave travelling in the z direction and the refractive index n expressed as a complex quantity given by $\tilde{n} = n + i\kappa$, where κ is defined as the extinction coefficient. In this case, we define the phase by $(kz - \omega t)$, where $k = \frac{2\pi}{\lambda}$ is the wavevector.

$$\vec{E}(z,t) = E_0 \exp\left[\left(i\left(\frac{2\pi\tilde{n}}{\lambda_0}z - \omega t\right)\right)\right] \tag{3.37}$$

$$\vec{E}(z,t) = E_0 \exp\left[\left(i\left(\frac{2\pi\{n + i\kappa\}}{\lambda_0}z - \omega t\right)\right)\right] \tag{3.38}$$

$$\vec{E}(z,t) = E_0 \exp\left[i\left(\frac{2\pi n}{\lambda_0}z - \omega t\right)\right]\exp\left[-\frac{2\pi\kappa z}{\lambda_0}\right] \tag{3.39}$$

This means that the plane wave decays with by an exponential factor proportional to the extinction coefficient κ. With this, we have covered the basics of the behavior of electromagnetic waves in presence of a polarization field. So far, we have restricted ourselves to non-absorbing dielectric materials. We will now investigate the optical properties of conductors.

3.4.2 Physical properties of metals

The optical properties of a metal are drastically different from the properties of a dielectric. Clearly, this related to the fundamental differences between an insulator and a conductor. The free electron model of metals views a conducting material as a collection of free electrons, the conduction electrons, which can move freely within a material at room temperature but are bound by the surface from which they are reflected. In this model, the energy is assumed to be purely kinetic and the electrostatic attraction between ions and free electrons is neglected. Finally, the energy of the conduction electrons is assumed to follow a Maxwell-Boltzmann distribution at finite temperatures. We will start with this simple model to predict the optical and electrical behavior of thin films.

From the equation of motion of electrons oscillating in the presence of an alternating electric field and the polarizability of the medium, we find the expression for the dielectric function $\varepsilon_r(\omega)$:

$$\varepsilon_r(\omega) = 1 - \frac{n_e q_e^2}{\varepsilon_0 m_0}\frac{1}{\omega^2 + i\frac{\omega}{\tau}} \tag{3.40}$$

where n_e is the free electron density of the medium, m_0 the free electron mass, and τ the characteristic time between two electron scattering events. We recognize from this equation the plasma frequency ω_p previously defined in eq. 3.4 ($\omega_p = \sqrt{\frac{n_e q_e^2}{\varepsilon_0 m_0}}$).

Classically, the plasma frequency represents the frequency of collective motion of free electrons in the metals oscillating due to the presence of positive ionic background [144]. The dielectric function (eq.3.40) can be separated into its real and imaginary parts as

$$\varepsilon_1(\omega) = 1 - \frac{\omega_p^2 \tau^2}{1 + \omega^2 \tau^2} \tag{3.41}$$

$$\varepsilon_2(\omega) = \frac{\omega_p^2 \tau}{\omega(1 + \omega^2 \tau^2)} \tag{3.42}$$

The above equations are the real and imaginary parts of the 'dielectric' function for the Drude model. For low frequencies, $\varepsilon_2(\omega) \gg \varepsilon_1(\omega)$ and the oscillations of the free electrons are responsible for the opacity and shiny appearance of metals. For higher frequencies, $\varepsilon_1(\omega) \gg \varepsilon_2(\omega)$, making $\varepsilon_r(\omega)$ a real function. In fact, at frequencies higher than ω_p, the motion of the electrons can't follow the oscillations of the electromagnetic field and thus the metal becomes transparent to those frequencies.

Figure 3.11 shows the reflective properties of an undamped Drude metal ($\tau = 0$) for frequencies above and below ω_p. The metallic medium is transparent to frequencies above its plasma frequency, and the incoming radiation is transmitted through the film, unperturbed by the free electron oscillation. For frequencies below, the medium is opaque to the incident radiation and reflects most of the light.

Table 3.1 shows the bulk plasma frequency and resistivities of different transition metals obtained from optical measurements [145, 146]. We see that for the selected metals, the plasma frequency ω_p is in the UV region, hence all the visible and infrared frequencies are reflected.
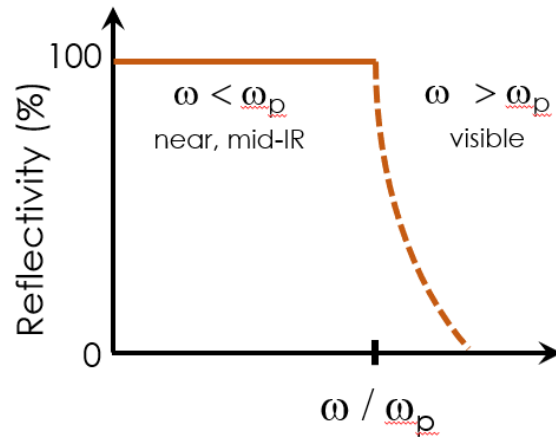
Figure 3.11 : Reflectivity of an undamped Drude metal as a function of frequency. For most metals, frequencies below ω_p include the near-infrared and frequencies above include the visible range.

Evidently, an opaque mirror can't function as a window inside the visible range. When the silver layer thickness is reduced to 15 nm or less, light in the visible spectrum is transmitted through, but the layer is still opaque to the near and far infrared (as shown in Figure 3.12). This makes the use of silver thin films possible in energy saving glazing.

Table 3.1 : Plasma frequency and resistivity of transition metals

Metal	Plasma wavelength (nm)	Resistivity ρ ($\Omega.cm$)
Ag	137.9	1.609×10^{-6}
Au	136.5	2.201×10^{-6}
Al	158.3	2.733×10^{-6}
Cu	156.3	1.696×10^{-6}
W	206.6	5.530×10^{-6}
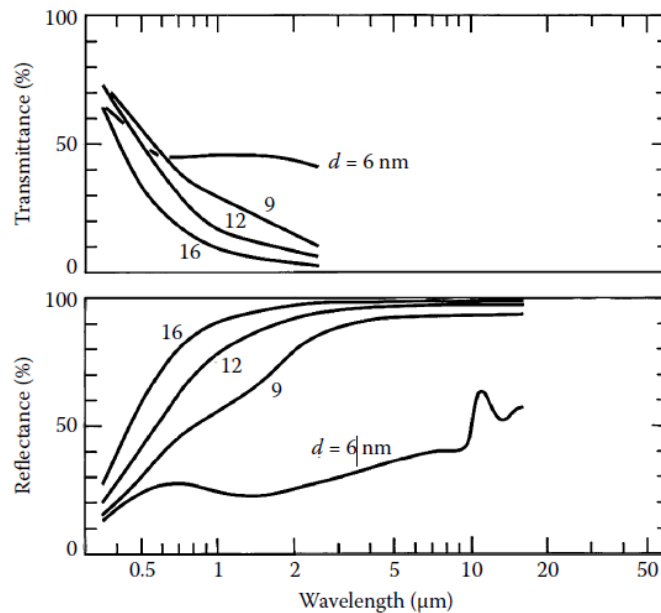
Figure 3.12 : Spectral normal transmittance and near-normal reflectance measured for Ag films on glass. The film thickness is denoted d. Modified from [147]

It must be noted that in the case of noble metals such as silver and gold, for incoming electromagnetic radiation with frequency $\omega \sim \omega_p$, the optical behavior of the material is governed by the interband transitions of valence bands to the conduction bands. These transitions must be taken into account when modeling the optical properties of a thin film (Figure 3.13). Thus, the dielectric function of a metal is given by the interband optical transitions below the plasma frequency, while the Drude model applies to frequencies above ω_p.
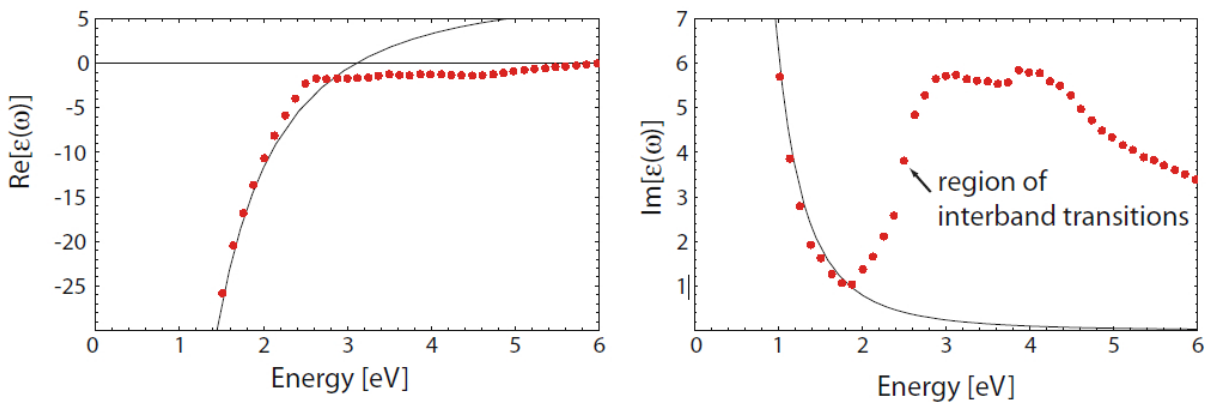
Figure 3.13 : Theoretical values (black lines) for $\varepsilon_r(\omega)$ based on the Drude model and experimental values (red lines) as a function of frequency. Reprinted with permission from [148]

The optical and electrical properties of a metallic film have strong correlation, resulting from the high density of free electrons present inside the film. In the presence of an external electric field $\vec{E}$, the free electrons will acquire a velocity $\overrightarrow{v_d}$, called the drift velocity. The displacement of the electrons between two scattering events is given by the mean free path λ_m:

$$\lambda_m = \overrightarrow{v_d}\tau \tag{3.43}$$

We express the force on the electron by

$$q_e\vec{E} = m_0\vec{a} \tag{3.44}$$

where $\vec{a}$ is the acceleration of the electron in the external field. The average velocity of the electrons is then given by

$$\langle\overrightarrow{v_d}\rangle = \vec{a}\tau = \left.q_e\vec{E}\tau\middle/m_0\right. \tag{3.45}$$

The current density $\vec{J}$ is defined as the flow of electrons inside the material,

$$\vec{J} = nq_e\langle\overrightarrow{v_d}\rangle = \frac{q_e n^2 \tau(\omega)}{m_0}\vec{E} \tag{3.46}$$

The proportionality constant is labeled the conductivity:

$$\sigma(\omega) = \frac{q_e n^2 \tau(\omega)}{m_0} \tag{3.47}$$

which for very low frequencies represents the DC conductance. For a two-dimensional system, in which a conductive film of thickness d on a surface with a width W and length L, that are much larger than the thickness of the film (Figure 3.14), it is better to quantify the electrical properties by the sheet resistance, which measures how current flows across the surface rather than through the film. The sheet resistance is given by

$$R_s = \frac{W}{\sigma L} \tag{3.48}$$

The resistivity of a thin metallic film can diminish from the perfect theoretical value in various ways [149]. First, the thickness of the silver film confines the motion of the electrons in one

direction, and the grain boundaries in the two other directions impact the resistivity of the thin film by diminishing the scattering time of the free electrons.
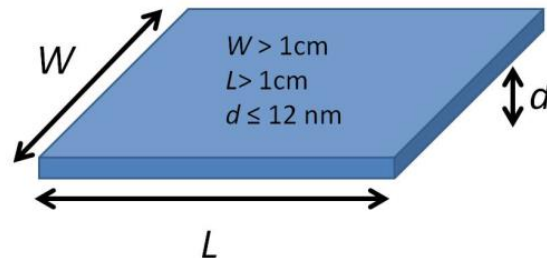
Figure 3.14 : Two-dimensional film

Second, the vibration of the silver ions at room temperature will create collision with the free electrons. Finally, the presence of impurities and defects in the silver film creates scattering centers for the free electrons, impeding once again on the resistivity of the silver film. The combination of all these effects on the scattering time results in an increase of the total resistivity, given by

$$\Omega_{\text{total}} = \Omega_{\text{boundaries}} + \Omega_{\text{temperature}} + \Omega_{\text{impurities}} + \Omega_{\text{defects}} \qquad (3.49)$$

Therefore, it is common to obtain electrical resistivity that are higher than the bulk values when the metallic medium is confined to a thin film. It becomes clear that a contamination-free environment as well as optimal film structure is needed in order to decrease any type of impurities and intrinsic defects during the synthesis of a silver thin film. The study of thin silver film growth will be the focus of Chapters 5, 6, and 7.

CHAPTER 4   EXPERIMENTAL METHODOLOGY

Characterization tools are an integral part of thin film sciences and are essential to understand and quantify nanoscale phenomena. The characterization methods can be either involved with surface phenomena or bulk properties and reveal information on the structural and chemical properties of each layer. In this chapter, the relevant methods used to characterize the silver-based samples will be described in detail.

4.1 Deposition chamber

All the sputter depositions were conducted inside a commercial *Kurt J. Lesker* CMS-18 process chamber (Figure 4.1). The deposition chamber uses a "sputter-up" configuration, with four magnetron heads facing the substrate. The magnetrons can hold 7.6 cm diameter targets and generate closed magnetic lines. Moreover, each magnetron can be connected to a DC or an RF power supply. Argon, oxygen and nitrogen gas flowing into the system are controlled by an MKS mass flow controller. The system is mounted with an M-2000 ellipsometer facing the 15 cm circular substrate holder at an angle of 70° via an optical feedthrough. The substrates can be heated to 800 °C using IR quartz lamp and rotate at a maximum rate of 50 revolutions per minute.

The main chamber is kept at a base vacuum of 10^{-7} torr using a turbo-molecular pump (Maglev turbo pump) and the samples are inserted through a load-lock kept at a base vacuum of 10^{-6} torr. During gas insertion, the gate valve between the chamber and the turbo pump is set at a fixed throttle position to enable pressure build-up inside the chamber.

The deposition conditions relative to each set of experiments (such as total pressure, partial pressure of reactive gases and power densities) is given in their respective sections in chapters 5, 6, 7 and 8.
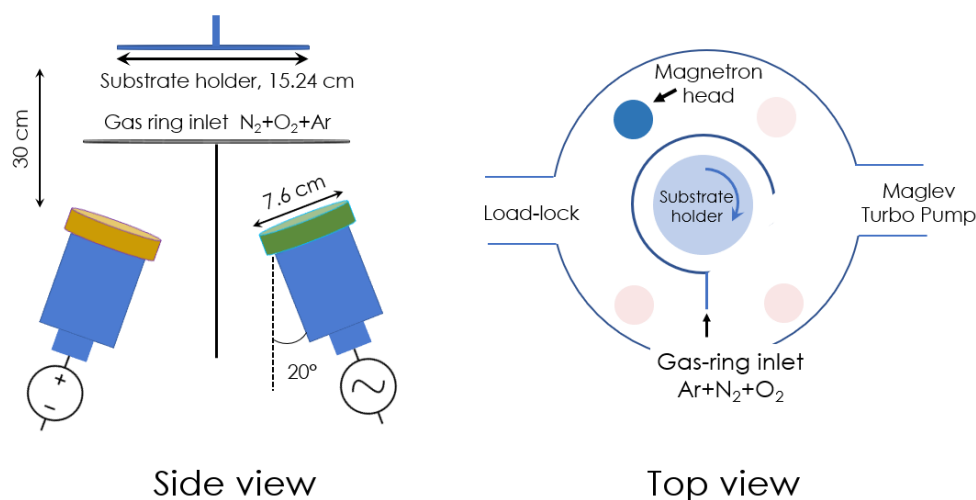
Figure 4.1 : Schematic drawing of CMS-18 deposition chamber.

4.2 Optical characterization

Light/thin-film interactions can reveal a wealth of information regarding the optical behavior of a single film, crystal or interfaces. Depending on the thin film chemical composition (stoichiometry, impurities, dopants), surface and interface characteristics (roughness, interface mixing) and thickness (density gradient, optical interference), the incident, probing light will be transmitted or reflected with a different intensity and polarization state that can then be used to determine the thin film(s) properties. In this sub-section, we will describe the optical tools used to characterize thin silver films as well as various dielectrics.

4.2.1 Spectrophotometry

For the optical characterization of low-e samples as well as absorbing, selective solar control thin films a *Perkin Elmer Lambda 1050* spectrophotometer was used. The *Lambda 1050* is a dual-beam spectrophotometer using a tungsten halogen lamp as well as a deuterium lamp to cover the UV-vis-NIR spectrum (covering from 175 to 3300 nm). A monochromator grating spectrally selects different wavelengths that are split in two different paths, one going through the sample (sample

beam) and one going through a reference sample (reference beam), and collected by a series of photodetectors:

- High sensitivity Photomultiplier Tube (PMT)
- 3-stage Peltier Cooled InGaAs
- Temperature stabilized PbS

For transmission spectra of low-emissivity coatings on a glass substrate, the reference beam is going directly to the detector. In that case, the reference beam is set at 100% of the full intensity, and the sample beam determines what percentage of the light goes through the sample. In the reflection measurement setup, a white standard plate (or an aluminum mirror, providing maximum reflection in the desired range) is placed at the end of the optical path as a sample, which will reflect the light to the detector. The white reference is then replaced by the sample and the measured spectra reveals the percentage of light that is reflected compared to the standard plate. The absorption was calculated by subtracting the transmission et reflection values from unity.

The transmission and reflection spectra of various samples were measured in the specular mode at 6° of incidence between 350 and 2500 nm with a 1-nm spectral resolution and used to calculate the common low-e glazing metrics such as T_{vis} and T_{sol}.

4.2.2 Ellipsometry

The ellipsometry technique has been the preferred approach for the characterization of thin films for many years [150, 151]. The advantage of ellipsometry is to provide a non-destructive method to monitor the optical quality and thickness of very thin films. The technique is based on the measurement of the polarization state of light upon reflection with a thin film and its interfaces. There exist multiple ways to measure and quantify the polarization state of a propagating electromagnetic wave and the operating principles of these measurements are summarized in Figure 4.2.
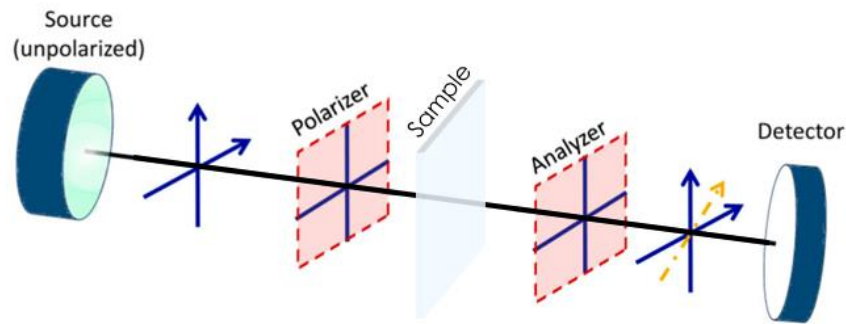
Figure 4.2 : Optical components along the optical axis in the cartesian coordinates needed to measure the polarization state of light.

Light produced from a source passes through a series of optical elements to either generate polarized light or to find the polarization state of the light. The optical elements are the polarizer and the analyzer. A polarizer placed in front of an unpolarized light source will give the incident field a specific polarization. For visible and UV light, a prism made of an anisotropic crystal is generally used. The anisotropic character of the prism ensures that only linearly polarized light is transmitted through the prism.

Optionally, it is possible to induce a phase delay between two polarized states by using a prism that acts as a waveplate, inducing a path difference between one of the polarization axes. Such optical component is labeled a retarder. The retarder (or compensator) is usually used to turn diagonally polarized light into circular polarized light. Moreover, by rotating the compensator, intermediate polarization state can be obtained. Thus, by placing these two optical components in front of an unpolarized light source, it is possible to produce any desired polarization state. By placing the same optical components in front of a detector, it is possible to extract the polarization state of the incoming light. For example, a rotating analyzer placed before the detector plane will allow the passage of only a certain polarization at a certain angle of rotation. In ellipsometry, a combination of these optical components is used to produce diagonally polarized light that is reflected off a sample.

Using the real part of eq. 3.37, we can mathematically describe two electromagnetic waves polarized in the *x-y* plane and propagating in tthe *z* direction:

$$E_x(z, t) = E_{0x} \cos(kz - \omega t + \delta_x) \tag{4.1}$$

$$E_y(z, t) = E_{0y} \cos(kz - \omega t + \delta_y) \tag{4.2}$$

It can be demonstrated the eq. 4.1 and eq. 4.2 can be re-arranged into the following equation,

$$\frac{E_x^2}{E_{0x}^2} + \frac{E_y^2}{E_{0y}^2} - 2\frac{E_x E_y}{E_{0x} E_{0y}} \cos \delta = \sin^2 \delta \tag{4.3}$$

the equation of a conical section, with $\delta = \delta_y - \delta_x$.

To simplify eq. 4.3, we introduce the following substitutions, $\varsigma = \frac{1}{E_{0x}^2 \sin^2 \delta}$, , $\varrho = \frac{1}{E_{0x}^2 \sin^2 \delta}$, and

$\vartheta = \frac{2 \sin \delta}{E_{0x}^2 E_{0y}^2 \sin^2 \delta}$ alongside with $\Theta = \sqrt{\frac{2\vartheta}{\varsigma}}$ and $\Gamma = \sqrt{\frac{2\vartheta}{\varrho}}$ to finally obtain

$$\frac{E_x^2}{\Theta^2} + \frac{E_y^2}{\Gamma^2} = 1 \tag{4.4}$$

the equation of an ellipse. Figure 4.3 shows a representation of this ellipse, from which we can extract

$$\tan \Psi = \frac{\Gamma}{\Theta} = \frac{E_{0x}}{E_{0y}} \tag{4.5}$$
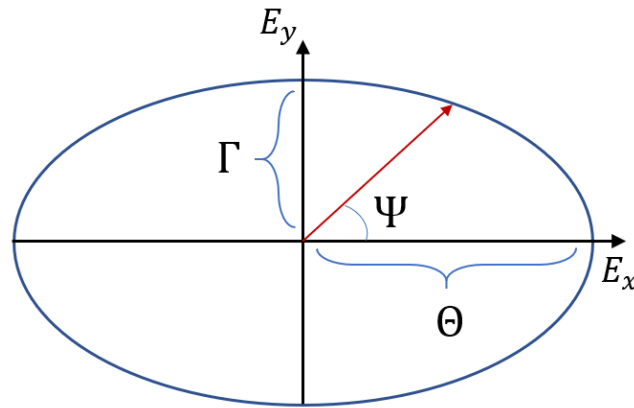
Figure 4.3: Representation of the polarization ellipse

When a beam of linearly polarized light is directed toward a stack of thin films, the reflected light phase and intensity will change based on the thickness and the refractive index of the layers inside the sample. The phase change induced by the optical path $\varphi = kd \cos \theta$, where k is the wavevector of light inside the medium and d the thickness of the thin film, is given mathematically by $\varphi e^{i\varphi}$.

Figure 4.4 shows a transparent layer deposited on a transparent substrate and demonstrates how to calculate the reflection coefficient of this layer-substrate system. The reflection coefficient may be calculated as a sum of the reflected and transmitted light at each interface, so that in the case depicted in Fig. 4.4 the reflection coefficient is

$$r = r_{a \to b} + t_{a \to b} \cdot r_{b \to c} \cdot t_{b \to a} \cdot e^{i2\varphi} \tag{4.6}$$
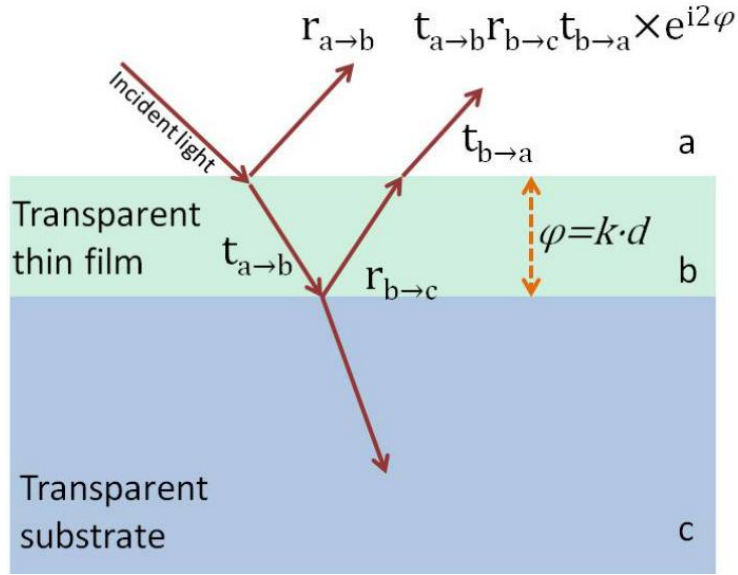
Figure 4.4 : Schematic drawing of the reflection and transmission coefficients in presence of a layer-substrate model.

Using the same approach in 1889, Paul Drude developed the equation of the reflection coefficient for *s*- and *p*-polarized light of a thin film deposited on a metallic surface

$$r_{s,p} = \frac{r_{s,p}^f + r_{s,p}^m \cdot e^{-i2\varphi}}{1 + r_{s,p}^f \cdot r_{s,p}^m \cdot e^{-i2\varphi}} \tag{4.7}$$

where $r_{s,p}^f$ is the reflection coefficient for the film deposited on a metallic substrate and $r_{s,p}^m$ the reflection coefficient at the film-substrate interface. We can rewrite eq. 4.7 as

$$r_{s,p} = \frac{I_{s,p}^r}{I_{s,p}^i} \cdot e^{-i\delta_{s,p}} \tag{4.8}$$

where $I_{s,p}^r$ is the intensity of the reflected light wave, and $I_{s,p}^i$ the intensity of the incident light wave. The absolute phase shift of the *s*- and *p*-polarized wave is denoted by $\delta_{s,p}$. We can then link the ellipsometry variables Ψ and Δ to the measured intensity:

$$\tan \psi = \frac{E_{0r,p}}{E_{0r.s}} = \frac{|r_p|}{|r_s|} \tag{4.9}$$

$$\Delta = \delta_p - \delta_s \tag{4.10}$$

The *ex-situ* characterizations were made using a RC2 (J.A. Woollam Co. Inc.) variable angle spectroscopic ellipsometer. This ellipsometer uses a quartz tungsten halogen lamp and a deuterium lamp. The light is collimated to pass through a polarizer element. The polarized light passes through a rotating compensator rotating with a frequency of 10 Hz. Upon reflection, the changes in polarization are measured by the receiver unit made of a second rotating compensator, rotating with a frequency of 6 Hz, and an analyzer. The detector unit is made of two internal spectrophotometers. The spectrophotometers are a Si CCD detector for the 193-1000 nm range and an InGaAs photodiode array for the 1000-1700 nm range. All analyzed samples were sputtered film on a borosilicate transparent substrate. The backside of the glass substrate was covered with an adhesive tape to supress reflection from the backside of the glass sample. The RC2 ellipsometer was set to take measurements at multiple angles of incidence (45, 55, 65 and 75°). All analyses are done using the *CompleteEase* software, where the user can provide the architecture of the sample (ellipsometric model) (number of layers, initial set of oscillators), and the software's algorithm will be set to find the best fit to the polarization data.

The *in-situ* characterizations were made by an M-2000 ellipsometer (J.A. Woollam Co. Inc.) at a fixed angle of 70°. The M-2000 differs from the RC2 by having only one compensator. The spectral range of the detectors is 250-1700 nm. During the *in-situ* monitoring, the M-2000 was set to take a measurement every 2.5 seconds. This allowed a good signal to noise ratio in the region of interest. Thus, it becomes a very useful tool to

monitor the thickness and/or properties of a film in real-time.

4.3 Surface and elemental characterization

The surface state of a thin film or the interface separating two layers can often be constrained to a few monolayers; therefore, surface sensitive techniques are often better adapted tools to correctly characterize the atomic composition above and below the surfaces. We will see in subsequent chapters how the surface composition plays a vital role in the growth mechanism of thin films and how a better control of the interface separating various layers can lead to better properties. In this subsection, we will describe three main characterization methods for surface and film elemental composition and morphology.

4.3.1 X-ray Photoelectron Spectroscopy

The X-ray photoelectron spectroscopy (XPS) is a powerful technique to probe the chemical composition of the surface of a thin film. The XPS technique is based on the generation of photoelectrons by X-ray generated in ultra-high vacuum with core electrons of atoms, and their subsequent detection, as shown in Figure 4.5. The apparatus used for the surface elemental analysis is the VG ESCALAB 3 MKII. The analyzed surface was 2 mm × 3 mm and the Mg Kα source was either perpendicular to the sample or at grazing angle of 70° to reduce to probing depth from ~5-10 nm to ~1 nm. When required, the surface of the samples was etched using an Ar^+ gun inside the vacuum chamber in order to clean the surface or perform sequential depth profiling on the samples. The survey scans were taken at 1 eV steps up to 1200 eV.
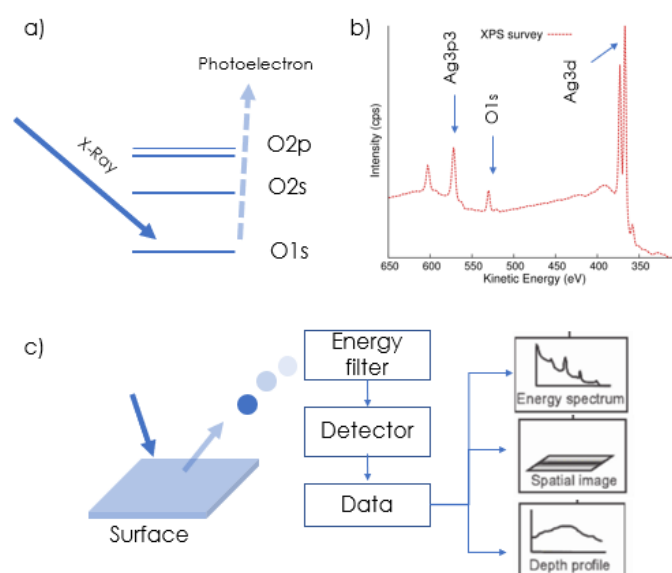
Figure 4.5 : Schematic example of (a) the photoelectron process with the various energy levels, (b) XPS survey spectra collected from a silver thin film deposited on glass with various elements identified on the surface from their atomic orbitals, and (c) the basic components of an XPS instrument along with the data formats that can be implemented. Modified from [152]

An X-ray with an impacting energy hv generates a photoelectron with the kinetic energy E_{kin}. If the energy hv is greater than the binding energy of the electron (E_b), the photoelectron will be collected at the analyzer after passing the work function barrier of the analyzer (φ_A).
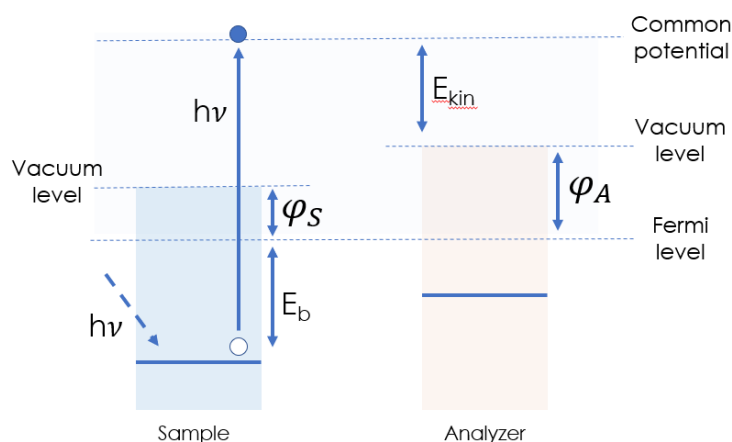
Figure 4.6 : Schematic explanation of relevant energy terms in XPS of solid surfaces. An X-ray with energy, hυ, generated a vacancy in a core electron level with a binding energy, E_b.

From Figure 4.6, the equation determining the kinetic energy of the emitted electrons is given by

$$E_{kin} = h\nu - E_b - \varphi_A \qquad (4.11)$$

Two operating modes are available for data acquisition, survey scans and high-resolution scans. A survey scan will reveal the elements present on the surface based on the energy signature of photoelectrons emanating from the atomic orbitals. In a high-resolution scan, the chemical state and bonding properties of each element can be revealed due to chemical interaction with their surrounding. The XPS technique has been used extensively to probe the surfaces of thin metal films and nanoparticles [153-156].

4.3.2 Time-of-flight Secondary Ion Mass Spectrometry

For elemental depth profiling, Time-of-flight Secondary Ion Mass Spectrometry (TOF-SIMS) was used. This powerful surface technique provides a surface probing sensitivity of 1-2 nm and an elemental detection sensitivity of ~1 ppm. An ION-TOF SIMS IV using a 25 kV Bi^+ primary ion source used in bunched mode with an average ion current of 1.37 pA is first used to sputter a raster area on the sample, leaving a crater. The depth profiling is then performed using a Cs^+ (O^{2-}) source for positive (negative) ion taken over an area of inside the crater, away from the edges, as shown in Figure 4.7a.
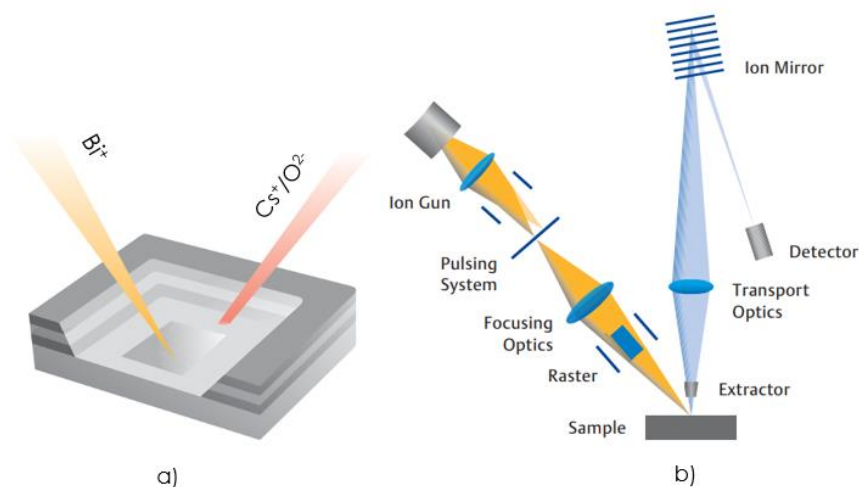
Figure 4.7 a) Dual-beam configuration for depth profiling where a crater is etched using a Bi^+ ion gun and a Cs^+ (O^{2-}) beam is used for secondary ion mass spectroscopy, b) schematic of a TOF-SIMS apparatus and operation. Modified from [157]

This process is conducted in a dual-beam configuration, where each beam is continuously pulsed to obtain the depth profiles. The Cs^+ (and O^{2-}) ions have shown to generate a large amount of secondary ion yields (both negative and positive) and a lower residual chemical damage to the sputtered atoms [158]. The sputtered atoms and molecules are accelerated in ultra-high vacuum where a time-of-flight analyzer is used to measure their masses. Figure 4.7b shows a schematic of a TOF-SIMS instrument.

4.3.3 Atomic force microscopy

The atomic force microscope (AFM) is another widely used tool to probe the surface topography, of thin films [159]. This technique has improved over the past years to a non-destructive technique capable of reaching atomic resolution [160]. The AFM that has been used in this work for surface topography is the Bruker D3100. The operating principle behind this AFM is depicted in Figure 4.8.
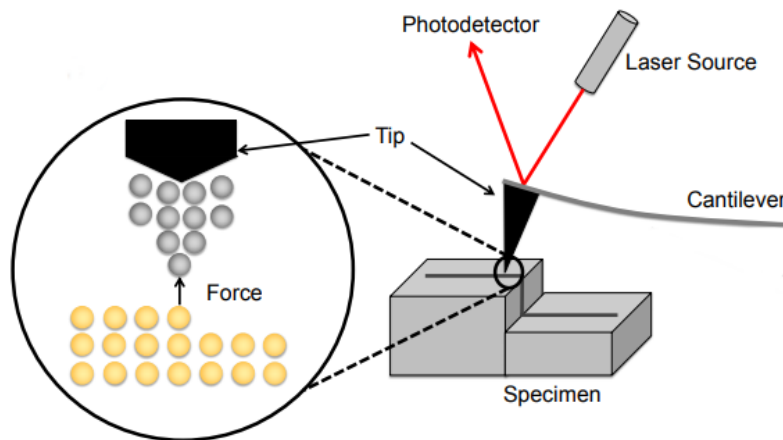
Figure 4.8 *:* AFM in tapping mode. Modified from [161]

A cantilever supporting a tip is set into an oscillating motion with a piezoelectric support fed with an electric signal. The oscillating motion is probed at all time with a laser. The tip oscillates with an amplitude of a few nanometers which is maintained constant with a feedback loop system. The tip is then brought near the sample where it starts to gently tap the asperities on the surface. As the tip sweeps the surface, the detection of the change in amplitude of the tip provides an image of the topography of the surface. Moreover, the change in the surface potential affects the natural resonant frequency of the tip, which leads to a mapping of the surface force gradient. The AFM technique is a very efficient tool to obtain the shape and size distribution of silver clusters that form during the sputtering process [162, 163] as well as the surface roughness of thin films.

CHAPTER 5   PERCOLATION THRESHOLD DETERMINATION OF SPUTTERED SILVER FILMS USING STOKES PARAMETERS AND IN SITU CONDUCTANCE MEASUREMENTS

5.1 Foreword

This chapter presents a straightforward approach to determine the percolation threshold of silver thin films deposited by magnetron sputtering on various oxide layers at room temperature. The proposed method is based on the observation of the coupling of p-polarized light with local surface plasmons. By measuring the first Stokes parameter in real time, one can determine the moment at which the nano-islands of silver begin to coalesce into a continuous film. We confirm the results by in situ and ex situ conductance measurements. The method is then used to assess the percolation threshold on different oxide seed layers such as ZnSnO, ZnO, TiO_2, and SiO_2

5.2 Introduction

Silver growth in vapour phase undergoes a surface diffusion and nucleation process which lead to the growth of nano-clusters (or nano-islands). These nano-islands can be represented by ellipsoid-like shapes in which a dipole resonance can arise in both axes of the ellipse. In this approximation, the dipole resonance couples more strongly to p-polarized light [164]. The transition between the nano-islands to a continuous film is an essential point for many reasons. First, the oscillating opposite charges give rise to a dipole moment that resonates in the presence of an incoming light wave with matching frequency [165]. As the nano-islands grow in size, the dipole interactions shift to greater wavelengths and the oscillations become weaker. Although theoretical assumptions based on the shape of these nano-islands and their mutual spacing could be used for modeling the light–plasmon interactions [166-168], the following proposed methodology is based on the direct

observation of the extinction of *p*-polarized light and its shift to lower frequencies to detect the onset of nanoparticle coalescence.

Second, there is a transition from a quasi-dielectric film to a conductive film as the nano-islands grow to form metallic pathways on the surface [169, 170]. Therefore, the transition marks the separation of the applications based on visible light absorption (research in plasmonics) and the applications based on a continuous thin film (low-e windows, TCEs, etc.). This transition point is referred to as the percolation threshold, and its dependence on the thin film growth mechanism and on the process conditions is of great interest. One of the experimental approaches to identify the percolation threshold is *in-situ* real-time conductance measurements. This method consists of placing two electrodes on the substrate on which the silver is deposited, applying a voltage, and measuring the current as a function of silver deposition time. The percolation threshold can then be defined as the transition between a dielectric film and a conductive film due to the silver formation of a conduction path from one electrode to the other [169-172]. A second approach is the use of real-time in situ ellipsometry to determine the optical constants of the growing film using a Drude–Lorentz model and finding the percolation threshold based on the transition of the optical constants [173-175]. The reliability of the results is, however, dependent on the accuracy of the model used to fit the parameters. Finally, a third approach to optically monitor the growth of the silver nano-islands in real time is to measure the relative variation of the samples' reflectivity. This technique is known as surface differential reflectivity spectroscopy (SDRS) and was recently demonstrated in [176]. In this work, we present a new approach based on *in-situ*, real-time polarimetry measurements using ellipsometric constants to monitor the growth evolution of silver nanoparticles and their coalescence into a continuous film. The use of polarimetry has previously been demonstrated to be of great interest to characterize electrically conductive thin films. The analysis is usually based on the detection of surface plasmon resonance [177] or plasmon excitations [178] by comparing the reflection coefficients of *p*-polarized and *s*-polarized light. Here, we specifically study a method to find, in a straightforward manner, the percolation threshold by monitoring the Stokes parameters on various metal oxide layers, without the need for an optical model. In addition, the results are supported by in situ and *ex-situ* conductance measurements.

5.3 Stokes parameters

The superposition of two orthogonal, coherent polarized electromagnetic (EM) waves results in diagonally polarized light. The two EM waves are referred to as *s*-polarized and *p*-polarized light according to the oscillation of the electric field with respect to the plane of incidence. The phase constants (δ_x, δ_y) and amplitudes (E_{0x}, E_{0y}) of the *p*-polarized and *s*-polarized light will determine the polarization state of the resulting EM wave. In ellipsometry, diagonally polarized light is sent onto a sample, and the resulting amplitudes and phase changes are measured. The results are usually given by the two ellipsometry parameters Ψ and Δ:

$$\Psi = \tan^{-1} \frac{|E_{0x}|}{|E_{0y}|} \tag{5.1}$$

$$\Delta = \delta_x - \delta_y \tag{5.2}$$

to represent light in terms of the intensity of the polarization constituents, we see from Eq. (5.1) that

$$E_{0x} \propto \sin \Psi \tag{5.3}$$

$$E_{0y} \propto \cos \Psi \tag{5.4}$$

so that

$$I_x \propto \sin^2 \Psi \tag{5.5}$$

$$I_y \propto \cos^2 \Psi \tag{5.6}$$

For a full description of polarized light in terms of the polarization's intensity I_x and I_y, the Stokes parameters (S_0, S_1, S_2, and S_3) are expressed as [151]:

$$S_0 = E_{0x}^2 + E_{0y}^2 = I_x + I_y \tag{5.7}$$

$$S_1 = E_{0x}^2 - E_{0y}^2 = I_x - I_y \tag{5.8}$$

$$S_2 = 2E_{0x}E_{0y}\cos\delta \tag{5.9}$$

$$S_3 = 2\,E_{0x}E_{0y}\sin\delta \tag{5.10}$$

where S_0 represents the total light intensity, S_1 is the dominance of I_x over I_y, or p-polarized light over s-polarized light, S_2 is the dominance of diagonal polarization over antidiagonal polarization, and S_3 is the dominance of the right circular polarization over the left circular polarization. We note from Eqs. (5.5) and (5.6) and Eqs. (5.7)–(5.10) that the Stokes parameters are related to Ψ and Δ by

$$S_1 = -\cos(2\Psi) \tag{5.11}$$

$$S_2 = \sin 2\Psi \cos\Delta \tag{5.12}$$

$$S_3 = -\sin 2\Psi \sin\Delta \tag{5.13}$$

Based on Eqs. (11)–(13), one can therefore recover the Stokes parameters using the ellipsometric constants. Note that these equations [Eqs. (5.11)–(5.13)] are valid for totally polarized light. In this case, S_0 represents the total light intensity (normalized to 1), and it is given by [35]

$$S_0 = (S_1^2 + S_2^2 + S_3^2)^{1/2} \tag{5.14}$$

The method developed in this chapter is based on the detection of the extinction of one of the polarization components (p-polarized light) at the resonant frequency rather than the evolution of the exact polarization state. Since the contributions of S_2 and S_3 are minimized at the resonant frequency, the measured light will be totally linearly polarized. Thus, in this work, S_0 is given by Eq. (5.14).

5.4 Sample preparation

5.4.1 Sputtering Condition

The Ag films were prepared by magnetron sputtering on B270 glass substrates and on the surfaces of four types of metal oxide films, namely SiO_2, TiO_2, ZnO, and ZnSnO. The oxides were sputtered in a fully automated, ultrahigh vacuum CMS-18 process chamber (K.J. Lesker Co. Inc.) with a base pressure of 5×10^{-8} Torr. The processes used were direct current magnetron sputtering (DCMS) and radiofrequency magnetron sputtering (RFMS) at a frequency of 13.56 MHz. The oxides and the silver films were deposited at pressures varying between 2 and 4 mTorr. The thicknesses and the optical properties (refractive index n and extinction coefficient κ) were modeled using spectroscopic ellipsometry and the CompleteEase software (J.A. Woollam Co. Inc.). A flow of O_2 gas was introduced inside the chamber, and the $Ar:O_2$ ratio was optimized to obtain transparent oxides with extinction coefficient $\kappa < 10^{-4}$ in the visible spectrum (380–780 nm). The thickness of each of the metal oxide seed layers was 10 nm. Table 1 summarizes the sputtering parameters of the oxide films.

Table 5.1 : Sputtering Parameters of the Seed Layers

Target	$Ar:O_2$	Pressure (mTorr)	Power Density (W/m^2)
SiO_2	10:1	2	6.0 (RFMS)
ZnSnO	10:1	2	3.1 (RFMS)
Ti	5:1	4	6.0 (DCMS)
Zn	10:7	2	2.1 (DCMS)

5.4.2 In situ Conductivity Measurements

To measure the conductance of the sputtered silver, a clean 2.5 cm $\times$ 5 cm B270 glass was masked, and 200 nm of aluminum film electrodes were sputtered on the exposed area (see Fig. 5.1). The mask was then removed, and the glass substrate was introduced inside the process chamber.
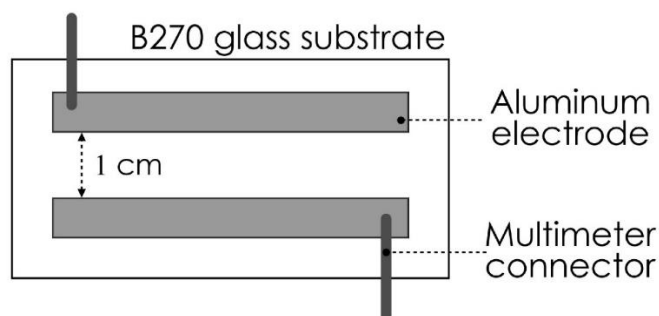
Figure 5.1 : Schematic representation of the sample prepared for *in-situ* ellipsometry and conductance measurements. The dimensions of the B270 substrate are 2.5 cm by 5 cm, and the distance between the electrodes is 1 cm. The multimeter is connected to the two aluminum electrodes.

Electrical measurements were performed with a Keithley 2100 Digital Multimeter (Keithley Instruments Co. Inc.), connected to the two aluminum electrodes. To avoid the electronic contribution of charged species inside the plasma, the silver film was sputtered in deposition sequences of 5 s before turning off the plasma generator. Current measurements were then made by varying the voltages from 0.1 to 1 mV under a vacuum of 5×10^{-8} Torr after each deposition sequence.

5.4.3 *In-situ* polarimetry

A M-2000 spectroscopic ellipsometer (J.A. Woollam Co. Inc.) fixed at an angle of incidence of 70° with a spectral range of 250–1650 nm and an acquisition time of 2.64 s was used to measure the polarization state of light reflected off the sample during the growth process. The Stokes parameters S_1, S_2, and S_3 were then found using the Ψ and Δ values obtained as previously described by Eqs. (5.11)–(5.13). To find the percolation threshold of silver sputtered on the glass substrate, real-time *in-situ* ellipsometry was used in conjunction with the conductance measurements. Each optical and electrical measurement was made independently after stopping

the deposition process every 5 s, for a total of 125 s. The delay between each deposition sequence was approximately 2 min to allow for completing the *in-situ* conductivity and optical measurements. The experiment was then repeated to find the percolation threshold on various seed layers using in situ ellipsometry during a continuous sputtering process of silver.

5.4.4 Ex situ Sheet Resistance Measurements

All ex situ electrical characterizations were made using the 737 PC-Based Monitor (Delcom Instruments Inc.). The measurements are contactless and permit us to keep the physical integrity of the sample. Contrary to the four-point method, one can thus avoid the necessity to puncture the surface with probes. Present-day contactless measurement techniques are based on the interaction of a (semi-)conducting layer with an alternating EM field. In this setup, an alternating magnetic field is generated across the conductive sample, inducing eddy currents inside the sample. The power absorbed in the production of eddy currents is proportional to the conductivity of the thin film. Thus, by calibrating using a test material with a known thickness and conductivity, it becomes possible to test for different conductive layers. The range of measurement for the samples using the 737 PC-Based Monitor is 0.1–1000 Ohm∕sq. with an error of 0.1%–1% from 0.1 to 100 Ohm∕sq. and 1%–10% from 101 to 1000 Ohm∕sq.

5.5 Results

As previously mentioned, the deposited silver will initially form isolated nano-islands possessing a specific free electron density. The density and the frequency of oscillations of these free electrons are expected to change gradually during the deposition of silver. Figure 5.2 shows the optical polarization response during the deposition of silver on a glass substrate, where the deposition was interrupted every 5 s to allow in situ current measurements. The optical response is analyzed by looking at the evolution of the Stokes parameters (obtained from the Ψ and Δ measurements). We see in Fig. 5.2(a) that for a wavelength of 1000 nm, the S_1 parameter reaches a value very close to -1 after approximately 55 s. According to Eqs. (5.8) and (5.14), the value of -1 for S_1 indicates that the reflected light must be completely linearly polarized with $I_x = 0$ and $I_y = 1$.

This extinction of I_x is due to the local plasmon frequency coupling to the p-polarized component of the light. In other words, nano-islands at that particular time in the deposition process give rise to a local plasmon resonance with an EM wave of 1000 nm. As the deposition process continues, the values for all three Stokes parameters diverge from the resonant values, and the collected light is thus elliptically polarized for this wavelength.
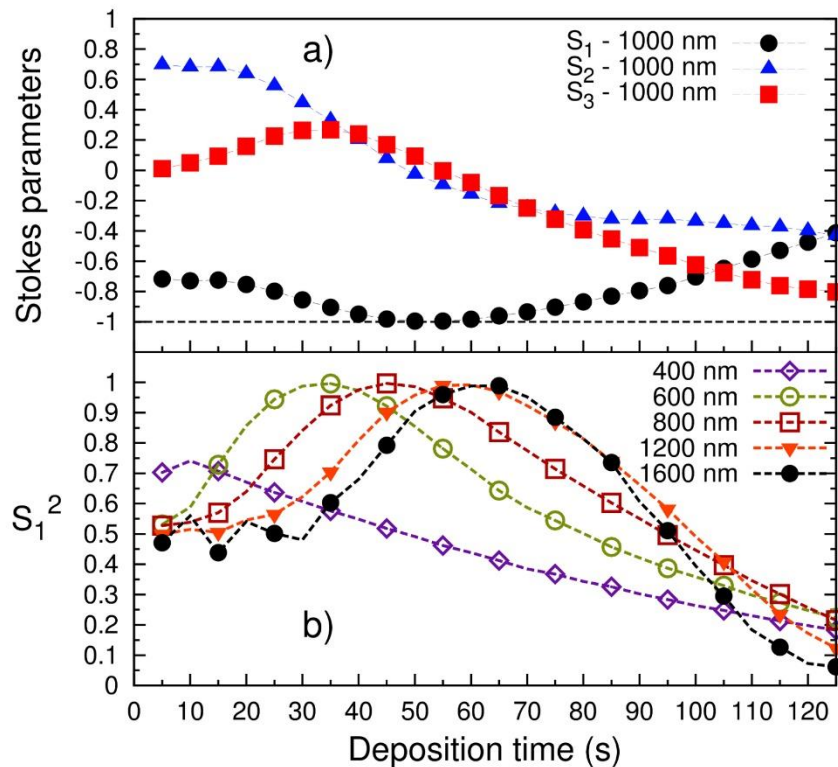
Figure 5.2 : (a) Evolution of the three Stokes parameters S_1, S_2, and S_3 for a wavelength of 1000 nm reflected off the sample during silver deposition on a B270 glass substrate. The first Stokes parameter S_1 equals -1 after approximately 55 s of silver deposition due to the extinction of the p-polarized light, as emphasized by the dashed line. (b) Evolution of the first Stokes parameter squared S_1^2 at multiple wavelengths.

Figure 5.2(b) shows the evolution of the first Stokes parameter squared at multiple wavelengths. The purpose of having a square value is to show the dominance of S_1 (the linear component of light) over S_2 and S_3 in S_0 [Eq. (5.14)]. We see that the maximum of S_1^2 for shorter wavelengths occurs earlier in the deposition process, and it occurs later for longer wavelengths in the near-

infrared due to a weakening of the frequency of free electron oscillations as the nano-islands grow in size. In other words, smaller nano-islands interact with shorter wavelengths and larger nano-islands interact with longer wavelengths. As the deposition continues, the resonant frequency given by the maximum of S_1^2 is confined in the near-infrared as more deposition time is required for S_1^2 to red shift to longer wavelengths. We define the point in time for which S_1^2 becomes stationary as the percolation threshold.

Figure 5.3 shows the deposition time for which the maximum of S_1^2 is reached for all wavelengths. To provide a numerical value for the percolation threshold, a function of the form

$$A - Be^{(-\lambda/c)} \tag{5.15}$$

was fitted to the experimental data, where λ represents the wavelengths from 370 to 1650 nm, and A, B, and C are the fitting parameters.
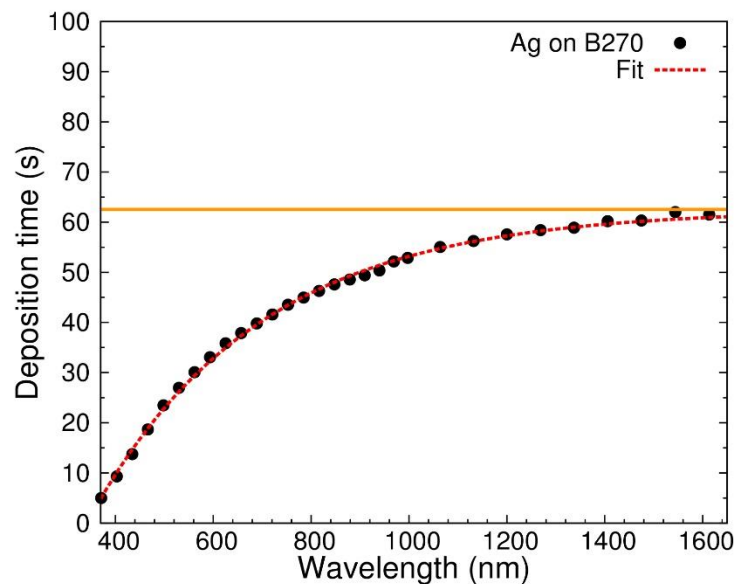
Figure 5.3 : Deposition time at which the maximum of S_1^2 is reached as a function of wavelength with the addition of the fitted function. The solid line is the value for A in Eq. (5.15) (62.5) and represents an upper estimate for the value of the percolation threshold in seconds.

The values obtained for the fit are given in Table 5.2. The value for A (62.5 ± 0.1) gives an upper estimate for the value of the percolation threshold as $\lambda \to \infty$.

Table 5.2 : Numerical Values for the Fitted Parameters of Eq. (5.15)

Parameter	Value
A	62.5 ± 0.1
B	168 ± 1
C	346 ± 2

Taking the midway point between the estimated upper limit (given by A) and the value of Eq.5.15 for λ 1650 nm (61.1 ± 0.1), we can obtain a reasonable estimate for the percolation threshold (61.8 ± 0.8 s). The deposition rate during the sputtering of silver was determined by ellipsometric measurements using a Drude–Lorentz model to be 0.1 nm per second.

As a means of confirming our previous method, the current between the two aluminum electrodes was measured under high vacuum between each deposition sequence. Figure 5.4 shows the current measured after each sequence using a semilog scale (Fig. 5-4(a)) and using a normal scale Fig. 5-4(b)). Significant currents can be obtained for all voltages after 60 s of deposition [Fig. 5.4(b)], and the measured current increases rapidly as the surface coverage increases. The percolation threshold is therefore between 60 and 65 s (62 ± 2.5 s) for this experiment. This is in accordance with the value found optically using the Stokes parameter S_1^2. The semilog scale Fig. 5-4(a)) for the measured current at 0.5 mV reveals two regimes of evolution of the conductance according to the point of inflection at 65 s separating two different curvatures. In light of what we have seen in Figs. 5-2 and 5-3, we know that regime II corresponds to the post-percolation growth. Regime I could correspond to thermally activated tunneling currents [169], where the electrons can travel from one island to another to finally reach the electrodes.
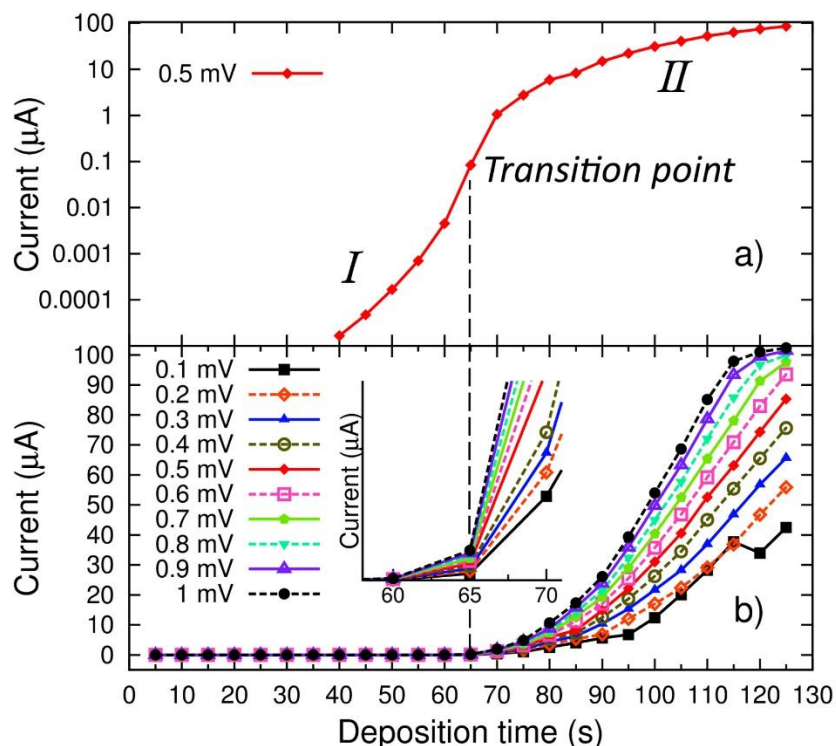
Figure 5.4 : (a) Measured current between two electrodes during silver film growth in semilog scale. There are two different current evolutions before and after the transition point at 65 s (labeled I and II), indicating two different evolutions of the electrical properties due to different growth stages. (b) Measured current in normal scale. There is a rapid increase of current occurring right after 60 s of deposition.

The experience was also repeated under continuous sputtering conditions to find the percolation threshold on glass and on various metal oxides. Figure 5.5(a) shows S_1^2 as a function of deposition time and for different wavelengths on a B270 glass substrate. The same plateau-like behavior observed in Fig. 5.2(b) can be seen here. However, the convergence occurs earlier in time, after approximately 50 s of deposition time, compared to 61.8 ± 0.8 s in the sequenced deposition mode.

It is reasonable to assume that the difference in the percolation time is the result of the difference between the processes. In the former experiment the deposition was interrupted every 5 s to measure the current between the two electrodes, allowing for extra diffusion time. Under continuous sputtering, there is a constant flux of silver atoms arriving on the substrate; therefore less diffusion time is allowed. The difference between the two spectra is presented in Fig. 5.5(b).
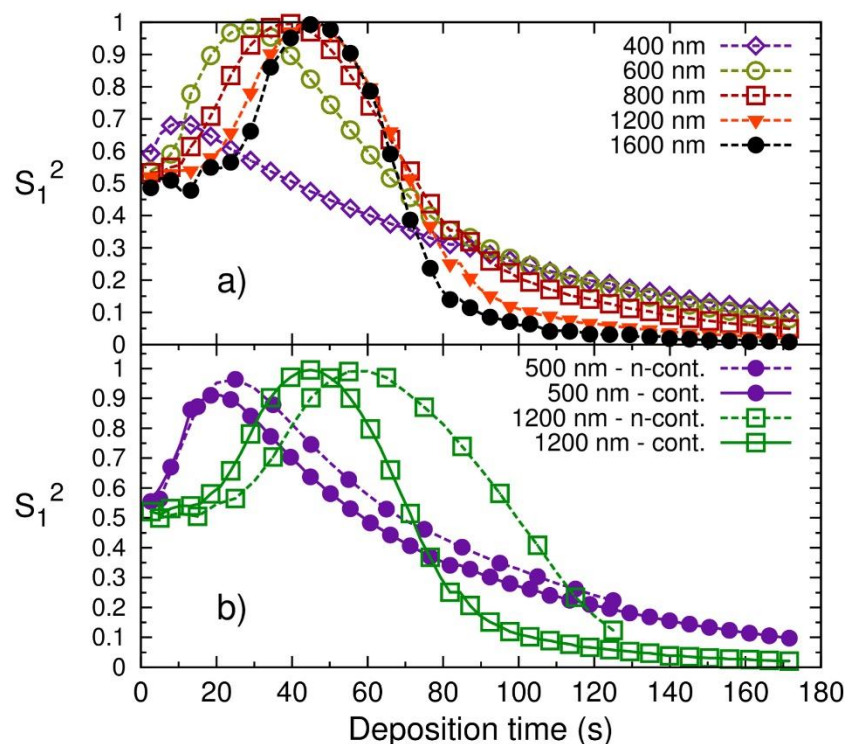
Figure 5.5 : (a) Evolution of the first Stokes parameter squared S_1^2 at multiple wavelengths on a B270 glass substrate. The maximum value of S_1^2 becomes stationary as a function of deposition time for longer wavelengths. The time for which S_1^2 becomes stationary for longer wavelengths is defined as the percolation threshold. (b) Evolution of S_1^2 at 500 and 1200 nm for a continuous (cont.) and noncontinuous (n-cont.) deposition process. The distribution for the n-cont. deposition appears to be broader and shifted to a longer deposition time.

Moreover, we can expect the percolation threshold to vary depending on the surface characteristics (such as surface energy and morphology) upon which the silver grows. By finding the time at which

the maximum occurs, we can determine when the percolation threshold occurs on glass and other seed layers, as shown in Fig. 5.6.
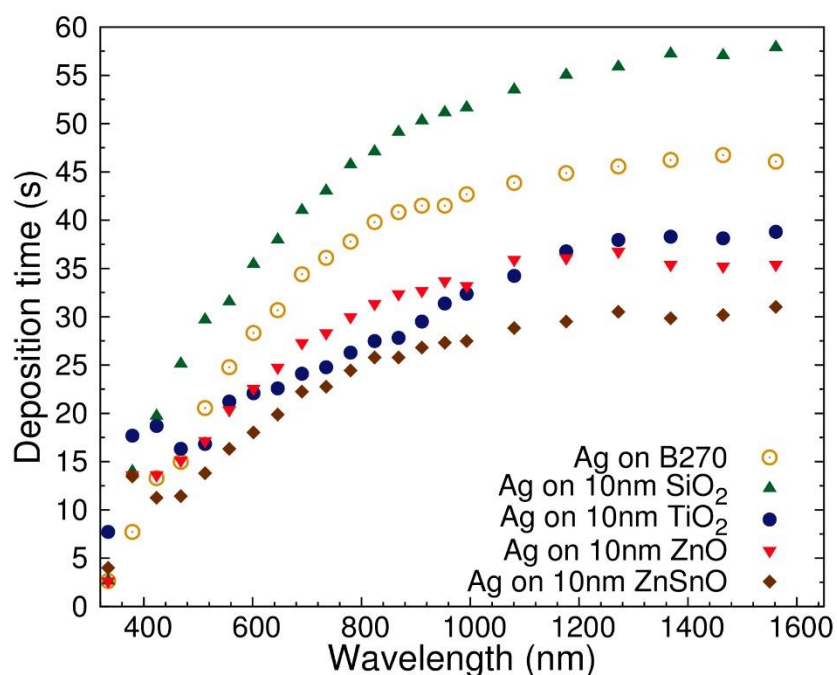
Figure 5.6 : Deposition time at which the maximum of S_1^2 is reached as a function of wavelength for a continuous deposition process. S_1^2 reaches a maximum according to what seed layer is beneath the silver layer. For example, the percolation threshold on a SiO_2 layer occurs much later in time than on the ZnSnO layer, due in part to the difference in surface energy between the two layers.

Table 5.3 shows the refractive index of the various oxides that have been tested for silver growth as well as their percolation threshold times, calculated as the midpoint between the upper limit and the value obtained numerically at a wavelength of 1650 nm, both obtained using Eq. 5.15.

The results clearly show that different percolation times are obtained for silver films deposited under identical process conditions but different underlying metal oxide layers. In order to provide more evidence for the validity of the proposed methodology for the continuous deposition of silver,

ex-situ conductance measurements were performed on various surfaces for different continuous deposition times, as shown in Fig. 5.7. The measurements were made using a contactless measurement monitor to assess the electrical properties of silver layers on various underlayers and for various silver film thicknesses. These measurements were taken immediately after removing the sample from the process chamber to avoid long exposures to atmospheric humidity. From Fig. 5.7(a), one can see that the sheet resistance of the silver film deposited on a B270 glass is very high for a deposition time past the percolation threshold (at 47 s), and it decreases rapidly as more silver is deposited.

Table 5.3 : Percolation Threshold and Refractive Indices Obtained on Various Seed Layers

Oxide	Percolation Threshold (s)	n @ 550 nm
SiO_2 (10 nm)	58.3 ± 0.6	1.47
B270	46.7 ± 0.2	1.52
TiO_2 (10 nm)	41 ± 1	2.38
ZnO (10 nm)	37.9 ± 0.5	1.94
ZnSnO (10 nm)	31.5 ± 0.5	2.01

Similarly, Fig. 5.7(b) shows the sheet resistance values for two other seed layers in comparison with the borosilicate glass substrate. For an equal amount of silver deposited, the layer will have better electrical properties and display a lower sheet resistance if it has coalesced sooner, leading to a more efficient conduction mechanism on the surface. As expected, the ZnO surface is better at promoting a continuous layer of silver during the deposition process. Moreover, we can see that the TiO_2 layer is also better than the borosilicate alone. Thus the ex situ measurements confirm the order in which the silver films coalesce, as indicated in Table 5.3.

5.6 Discussion

The combination of direct optical monitoring and *in-situ* conductance measurements in the determination of the percolation threshold of silver thin films confirms the existing theories about the optical and electric properties of silver during film growth. To assess the percolation threshold time by optical means more precisely, probing the resonance at longer wavelengths (up to 2500 nm) would be beneficial as the plateau-like behavior would be more visible than what we obtain when using the data presented in Fig. 5.6; the percolation threshold could thus be calculated more precisely.
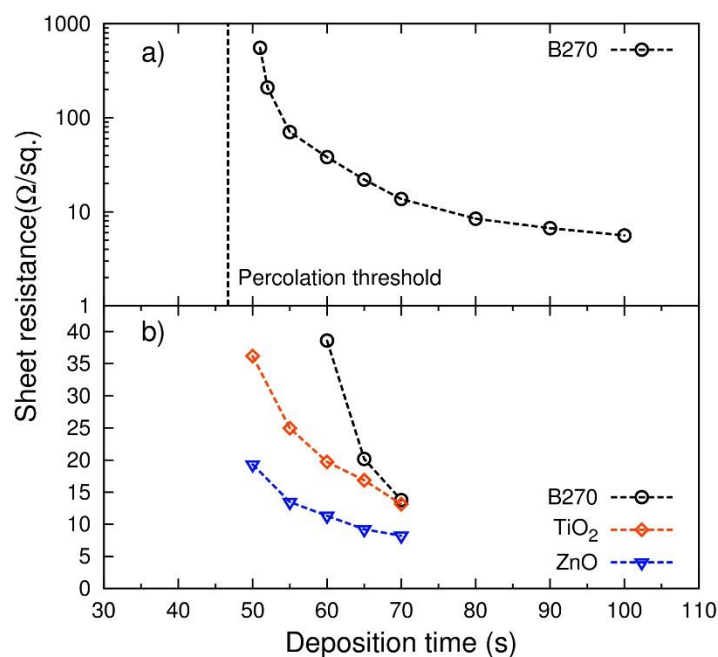
Figure 5.7 : (a) Ex situ sheet conductance measurements of silver for various continuous deposition times on a logarithmic scale. The first measurement was possible after 51 s of deposition. The vertical dashed line indicates the percolation threshold time obtained by optical means. (b) Ex situ sheet conductance measurements of silver for various continuous deposition times on various surfaces. As expected from Table 5.3, the ZnO layer is more efficient at promoting the formation of a continuous silver layer as predicted by the optical measurements.

We have mentioned that one of the factors influencing silver coalescence is the surface energy of the seed layers. From the results presented in Table 5.3, we see that the highest percolation threshold time is obtained in the presence of a SiO_2 underlayer followed by the bare B270 glass substrate. A borosilicate B270 glass substrate may possess more metallic inclusions compared to a vacuum deposited thin SiO2 film, thus increasing its surface energy. The lowest percolation threshold time is obtained on zinc stannate (ZnSnO) and zinc oxide (ZnO) films. In fact, zinc oxide films are well known as seed layers for silver growth [9, 19] as they increase the wettability of the deposited silver

films. The presence of tin in the zinc stannate films could have an impact on increasing the surface energy above that of the zinc oxide films. This could explain qualitatively why the percolation threshold is reached twice as fast when using a zinc stannate layer than a silicon dioxide layer.

It is also known that the surface energy may change under UV radiation [179-181], electrical surface charging [182], and heat treatment [183]. Therefore, by selecting the appropriate factors during silver growth it would be possible to control the percolation threshold time. Besides the atomic composition and surface treatments, which can also influence the surface energy, the microstructure of the underlying films is also known to impact the coalescence of the silver film by a roughness-induced change of wettability of the films [184, 185]. Therefore, a careful control of the microstructure to reduce or increase the roughness or surface patterning could also impact the percolation threshold time.

Moreover, the size distribution of the nanoparticles [12] could be linked to the statistical distribution of the S_1^2 parameter, as the particles' shape, size distribution, and surface coverage have a strong effect on the optical response of polarized light. Therefore the random distribution of the nanoparticles' size probed by the ellipsometer during the growth could eventually be determined in situ and could be the object of future experiments.

5.7 Conclusion

In this work we have showed how to determine the percolation threshold on various seed layers by direct optical measurements of the Stokes S_1 parameter without the use of optical models, and we have confirmed the results with in situ and ex situ conductivity measurements. We defined the

percolation threshold as the point in time for which the maximum of S_1^2 becomes stationary as a function of deposition time for longer wavelengths. We have confirmed that the percolation threshold time corresponds to the measurements of nontunneling currents under high vacuum. The percolation threshold thus marks the minimum amount of material required to reach a conductive thin film needed in various applications. Moreover, the method can be used to find the appropriate seed layer to wet the deposited silver layer and limit the formation of nano-islands. For applications that require light absorption, the S_1^2 parameter may be used to tune the plasmon resonance at the desired wavelength.

COPYRIGHT NOTICE

The material presented in this chapter is reproduced and modified from :

CHAPTER 6   CONTINUOUS ULTRATHIN SILVER FILMS DEPOSITED ON SIO₂ AND SINₓ USING A SELF-ASSEMBLED MONOLAYER

6.1 Foreword

In this chapter, we study the deposition of ultrathin silver films on silicon oxide and nitride surfaces functionalized with self-assembled monolayers of (3-mercaptopropyl)-trimethoxysilane. First, we compare both solution and vapour-phase functionalization techniques and find the greatest improvement in electrical and optical properties using deposition from solution. Using X-ray photoelectron spectroscopy, we demonstrate that the formation of silver-sulfur covalent bonds is at the root of the improved wetting confirmed by ellipsometry, sheet resistance measurement, and atomic force microscopy. Second, we show that this technique can be extended to functionalize silicon nitride. Finally, we demonstrate a simple, but efficient, low-emissivity optical filter.

6.2 Introduction

The ability to deposit high quality ultrathin metallic films is highly sought after due to the possibility of combining intrinsically high conductivity [8], optical transparency, and flexibility [186, 187]. Among the transition metals, silver thin films possess the lowest sheet-resistance and excellent optical transparency[188]. Silver growth under vacuum on non-metallic surfaces undergoes various stages of growth where the formation of nanoclusters dominates the morphological evolution of the thin film until the percolating stage where the surface coverage of the underlayer is completed [189, 190]. For this reason, there is substantial interest in developing methods that allow for percolation to occur earlier in the growth process, thus allowing thinner conductive films with higher transparency. Sometimes the changes in properties at various growth stages are so drastic that the same material can be destined for use in different applications according to its mass-effective thickness. For example, silver and gold, which exhibit pronounced localized surface plasmon resonances in the nanoparticle stage, can be used in solar cells [191] and

hydrogen production[192, 193]. In contrast, thin continuous metallic films are desirable for use in transparent electrodes [194] and low-emissivity windows [195].

6.3 Self-assembled monolayer surface treatment

Much of the research done on the wetting of silver films relates to finding the optimal surface to deposit the thin silver layer, such as sub-monolayer metal seeding [24, 196, 197], conductive organic layers [198], and other metal-oxide compounds. In contrast to physisorption where adatoms captured on the surface by coulombic interactions can diffuse to form nanoclusters, chemisorbed atoms can be attached to the surface by a strong chemical bond that prevents diffusion and allows for the formation of a very thin layer. For gold on SiO_2, a commonly used surfactant is the small molecule (3-mercaptopropyl)-trimethoxysilane (MPTMS) (linear formula $HS(CH2)_3Si(OCH_3)_3$). It self assembles on glass via its silane unit and functionalizes the surface with thiol groups (–SH) [199-201]. Self-assembly can proceed when a hydroxyl-terminated surface is immersed in a solution containing MPTMS or by adsorption following evaporation of the molecule. In the case of silver, MPTMS has been used to promote adhesion of silver particles [202, 203], and recently extended to continuous thin silver films [204, 205]. The formation of MPTMS self-assembled monolayers (SAMs) has been shown exclusively for silicon and SiO2 on which –OH groups can readily form following a piranha etch, UV/ozone, or oxygen plasma cleaning treatment. Moreover, the mechanisms behind the enhanced adhesion of silver atoms on a treated surface [204] have yet to be clearly uncovered. In this letter, we study the wetting of silver following the formation of an MPTMS SAM prepared by solution and from the vapour phase. We explicitly demonstrate chemisorption of the initial silver atoms as the reason for the dramatic improvement in film quality. Finally, we show that the process can be extended to silicon nitride films and use this to demonstrate a simple low-emissivity filter.

6.4 Sample preparation

To compare solution and vapour-phase functionalization, pre-cleaned borosilicate glass substrates were coated with 10 nm-thick SiO_2 thin films using RF magnetron sputtering (applied power density of 64 W/in^2 on a Si target, working pressure of 1.5 mTorr with an Ar/O_2 ratio of 2:1) to act as buffer layers. Surface activation was then performed using an oxygen plasma (6 W for 20 min

at a working pressure of 8 mTorr) to increase the formation of hydroxyl bonds on the SiO_2 surface. The solution-processed MPTMS monolayer was obtained by immersing the SiO_2 samples in MPTMS solution (5% v/v MPTMS in anhydrous toluene (99.8%) prepared inside a nitrogen glove-box in a sealed container) for 30 min, washed with toluene, and dried using a nitrogen gun. The samples were then annealed inside a vacuum chamber at 100 °C overnight. The vapour-phase samples were prepared by placing substrates inside a desiccator containing 0.1 ml MPTMS and then saturated with MPTMS vapour by pulling vacuum. These were left within the saturated vessel for 4 h.

6.5 Results

6.5.1 Vapour vs solution processed MPTMS treatment

To confirm the formation of the MPTMS SAM, X-ray photoelectron spectroscopy (XPS) measurements were performed. Figure 6.1(a) shows the high-resolution spectrum of the sulfur 2s orbital for the solution processed MPTMS SAM. We use the S2s orbital for this investigation instead of the more intense and commonly used S2p because of the overlap of the S2p with the plasmon loss peak of the Si 2s. We see the presence of sulfur at the characteristic binding energy of C-S bonds at 228.1 eV.
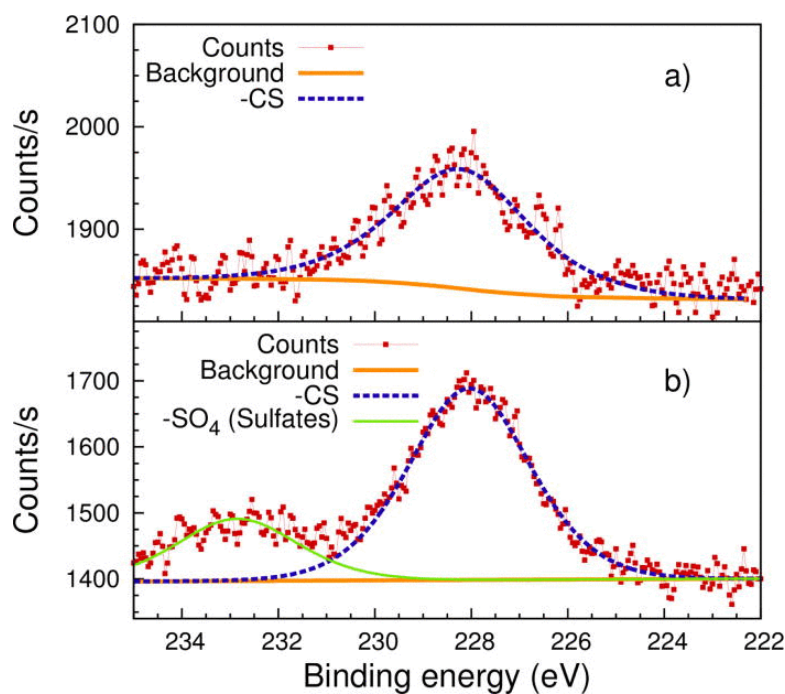
Figure 6.1 : (a) High resolution XPS scan of the sulfur 2s orbital for the solution-processed MPTMS SAM. The peak is centered at a sulfur-carbon binding energy of 228.1 eV (b) High resolution scan of the sulfur 2s orbital for the vapour-deposited MPTMS SAM. We notice the addition of the sulfates peak at 232.9 eV.

However, due to the close electronegativity values of S, C and H, we cannot distinguish between S-H, S-S, and C-S bonding. Figure 6.1(b) shows the high-resolution spectrum of the sulfur 2s orbital for the vapour formed MPTMS SAM. In addition to the C-S bond, we clearly detect sulfates ($-SO_4$) appearing in the high-resolution scan centered at 232.9 eV. The surface consists of 33% sulfate bonds and 67% thiol bonds for the vapour deposited samples, but only of thiol bonds for the solution processed samples. Thin silver films 7.0 nm thick were then deposited simultaneously on the vacuum and solution processed MPTMS samples as well as on a bare SiO_2 layer using DC magnetron sputtering (2.1 W/in^2 power density on a silver target (99.999% purity) at a deposition rate of 1 A/s). Table 6.1 shows the sheet resistance measured on all three samples immediately after the deposition and after 24 h.

Table 6.1 : Sheet resistance following 7 nm deposition of silver.

Sample	As deposited ($\Omega/\square$)	After 24 h ($\Omega/\square$)
Solution-processed	29 ±3	32 ± 3
Vapour-processed	70 ± 7	119 ± 10
SiO$_2$	220 ± 20	-

We observe a dramatic improvement between treated and untreated samples. Figure 6.1 and Table 6.1 show, however, that the solution-processed protocol is more efficient in creating sulfur thiol groups and improving wetting. It appears that the presence of sulfates on the vapour-formed SAM prevents the formation of Ag-S bonds, which can serve as nucleation centers for the sputtered silver atoms, preventing diffusion and promoting a layer-by-layer type of growth.

6.5.2 Silver wetting on MPTMS SAMs

The presence of sulfates when using the vapour-processed protocol indicates that it is best for the reaction to occur in an oxygen-free atmosphere. In addition to the sheet resistance measurement, atomic force microscopy (AFM) was carried on 7 nm thick silver films deposited on an MPTMS-treated (from solution) and a bare borosilicate glass. Figure 6.2(a) shows the topography of the silver film deposited on top of the MPTMS-treated glass while Figure 6.2(b) shows the topography of the silver film on bare glass. We observe a clear difference between the surface morphology of the two samples. The MPTMS-treated sample has distinctive small surface features and a very low average surface roughness (R_q) of 0.6 nm, characteristic of a smooth continuous film while the untreated sample shows a high average surface roughness value of 1.8 nm. The differences in the surface topography highlight the role of the solution-processed MPTMS treatment as an efficient wetting layer.
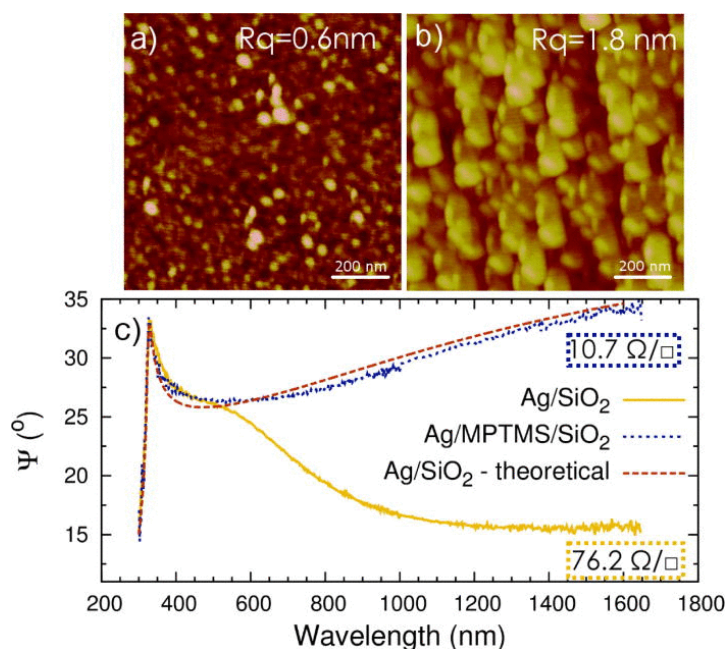
Figure 6.2 : (a) Atomic force microscopy images of a 7 nm silver film deposited on a MPTMS-treated borosilicate glass and (b) on a bare borosilicate glass sample. The average surface roughness (R_q) is shown (c) Optical characteristics obtained from ellipsometry measurements: measured W for a 8.8 nm silver film on both the MPTMS-treated and untreated SiO2 surface. The sheet resistance values for the treated and untreated samples are shown

Optical properties were measured using in-situ ellipsometry (M-2000, J.A. Woollam) at an incident angle of 70 to determine the effect of the SAM treatment. An 8.8 nm silver layer was deposited on an MPTMS-treated sample using the solution-based protocol and on a bare SiO_2 layer. Figure 6.2(c) shows the Ψ spectrum measured after silver deposition on each sample. Figure 6.2(c) also includes the theoretically calculated Ψ value for a thin silver film of the same thickness having bulk properties. We see clearly that the treated surface leads to a continuous film with properties approaching the bulk, while the film grown on bare SiO_2 differs significantly. The bulk-like optical properties of the silver film can be attributed to the very smooth surface obtained when using an MPTMS treatment. Moreover, contactless sheet resistance measurements revealed a value of 76.2 $\Omega/\square$ for the untreated surface and 10.7 $\Omega/\square$ with the MPTMS treatment for the same silver thickness.

To confirm the Ag-S bonding of the very first impinging atoms, a very small amount of silver (mass-thickness equivalent of 0.2 nm) was deposited on a solution-processed MPTMS treated surface. Figure 6.3 shows the high resolution spectra of sulfur on an MPTMS SAM before (Fig. 6.3(a)) and after (Fig. 6.3(b)) silver deposition.
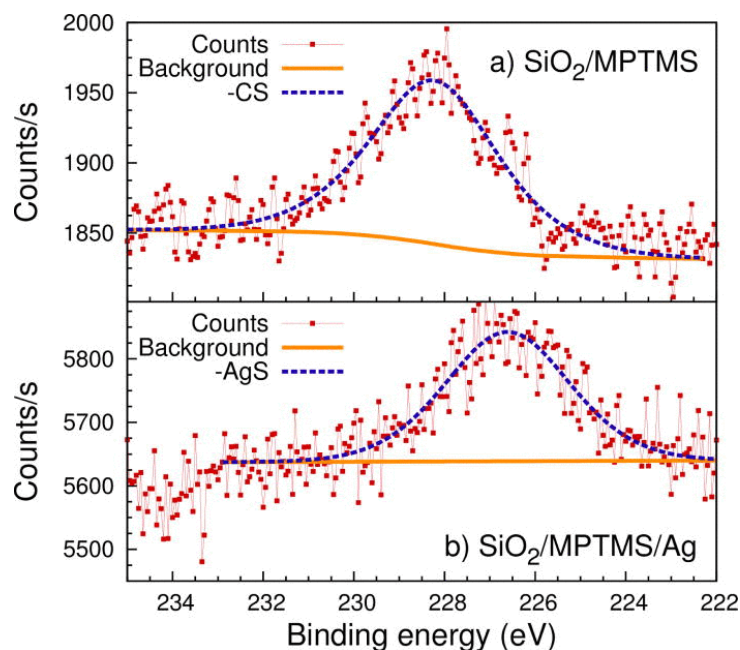
Figure 6.3 : High resolution XPS scan of the sulfur 2s orbital. The peak is centered at a sulfur-carbon binding energy of 228.1 eV. (b) High resolution scan after deposition of a sub-monolayer silver film. The peak is centered at a silver-sulfur binding energy of 226.6 eV.

For the silver deposited sample, we see a noticeable shift of the binding energy to lower energies at 226.6 eV, characteristic of Ag-S bonds, confirming that the initial atoms bind to the MPTMS activated surface. This shift in energy is explained by the lower electronegativity of silver compared to sulfur. The decrease of binding energy during covalent bonding between sulfur and metals is well documented and has been reported for thiol groups bonding with silver atoms [206]. This chemisorption process differs from wetting on chemically inert surfaces, where the surface free energy is a good indicator of the thin film growth behavior. In fact, MPTMS-treated surfaces tend to increase the measured water contact angle [207], which usually indicates a decrease in both the wettability and adhesion for metal atoms.

6.5.3 MPTMS formation on SiN$_x$

In principle, the requirement for the formation of an MPTMS SAM is the presence of a hydroxyl-terminated surface. To demonstrate that the process can be extended beyond the use of SiO$_2$, we have deposited MPTMS SAM from solution on 10 nm-thick magnetron-sputtered SiN (64W/in^2 using a Si target, 1.5 mTorr pressure with a Ar/N$_2$ ratio of 3:1) on which a layer of silver of equivalent mass-thickness of 0.20 nm was deposited. Figure 6.4 shows the high resolution spectra of the sulfur 2s orbitals. We notice again the presence of sulfur and thiol groups on the surface and the resulting shift of the 2s orbital in the presence of silver. We believe that the plasma modifies the elemental composition of the surface of the SiN layer to form a silicon oxi-nitride interface, where hydroxyl groups are easily formed. Interestingly, we notice the presence of sulfates in the high resolution scans, consisting of 20.9% of the S2s peak intensity before the silver deposition (Fig. 6.4(a)) and 9.4% after the silver deposition (Fig. 6.4(b)).

To demonstrate an application of this technique, we fabricated a "minimalistic" 3-layer low-emissivity optical filter using a SiN/Ag/SiN structure. The first 10 nm thick SiNx film was simultaneously deposited on two cleaned bare glass samples. One of the samples underwent the solution-based protocol described above for the formation of an MPTMS SAM, and both samples were then placed together inside the process chamber where depositions of 8.8 nm of silver and of the final SiN$_x$ film were performed. Figure 6.5 shows the optical properties of the full structure, including the glass substrate. Although wetting of silver on SiN$_x$ is intrinsically better than on SiO$_2$, we see that the low-emissivity filter with MPTMS functionalization is significantly improved.
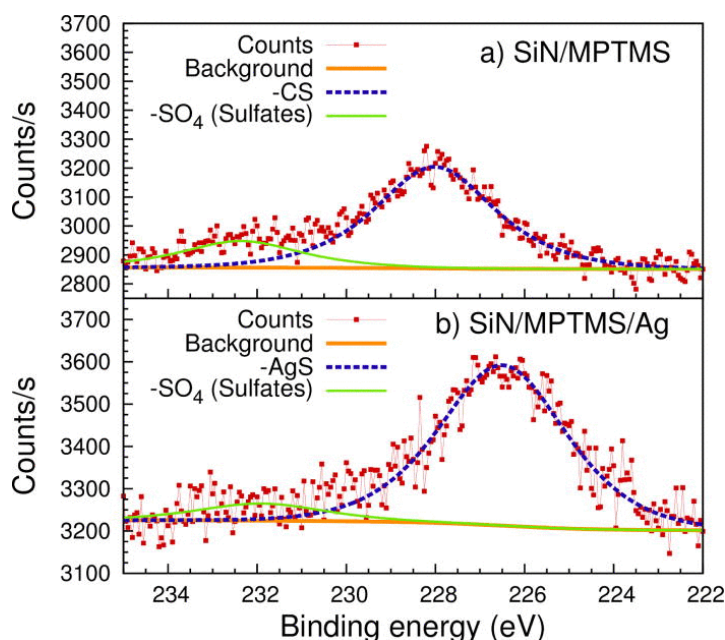
Figure 6.4 : (a) High resolution XPS scan of the sulfur 2s orbital for the MPTMS-treated SiN films (b) High resolution scan after deposition of a sub-monolayer silver film. We notice the shift in energy from the top part due to binding to silver atoms.

It shows a higher near-infrared reflection (86.6% vs 76.2% at 2500 nm) as well as higher visible transmission (81.1% vs 69.7% at 550 nm) for the same amount of sputtered silver. This is explained by a thinner, more conductive film brought about by the better wetting properties of the MPTMS-treated surface. Moreover, electrical measurements show a sheet resistance of 10.7 $\Omega/\square$ for the untreated stack and 7.4 $\Omega/\square$ for the treated one.

6.6 Conclusion

In summary, we have demonstrated, using XPS, the chemisorption mechanism of silver atoms on an MPTMS monolayer and linked the initial binding of silver to sulfur atoms to the improved electrical and optical properties of the silver film. We have shown that the vapor-deposited MPTMS SAM, where vacuum is pulled directly from ambient conditions leads to the formation of a substantial amount of sulfates on the surface, preventing optimal wetting of the silver layer. Using in-situ ellipsometry, we find that the silver film grown on top of MPTMS-treated surfaces exhibits optical properties very close to those of the bulk and is characterized by a very smooth surface as observed from AFM images. Finally, we demonstrate that the MPTMS SAM can act as an efficient

wetting layer for silver on other materials, such as SiN_x, which greatly improves the performance of a simple low-emissivity filter
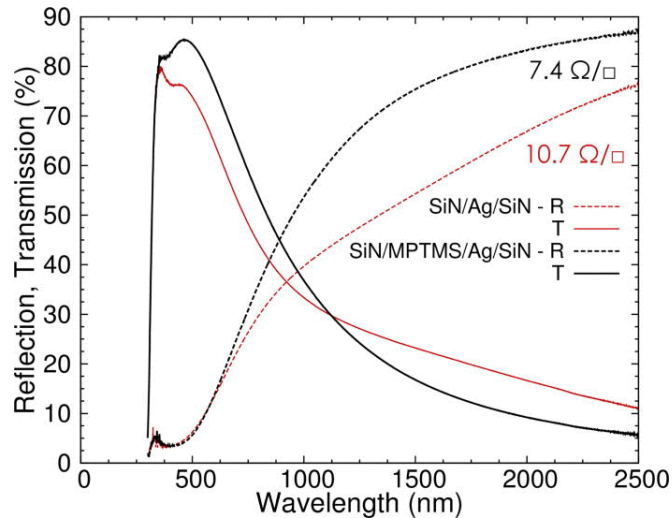
Figure 6.5 Comparison of a simple design of a low-emissivity filter on a B270 glass substrate with and without MPTMS treatments. The sheet resistance values for both devices are shown.

COPYRIGHT NOTICE

The material presented in this chapter is reproduced and modified from:

Soroush Hafezian, Kate Maloney, Josianne Lefebvre, Ludvik Martinu, and Stéphane Kéna-Cohen, "Continuous ultrathin silver films deposited on SiO_2 and SiN_x using a self-assembled monolayer," Appl. Phys. Lett. 109, 121603 (2016) with the permission of AIP Publishing.

CHAPTER 7   DEGRADATION MECHANISM OF PROTECTED ULTRATHIN SILVER FILMS AND THE ROLE OF THE SEED LAYER

7.1 Foreword

In this chapter, we characterize the oxidation and degradation of protected silver thin films through the Kirkendall effect. We then present a solution to reduce the degradation of silver films exposed to a reactive oxidizing environment. In particular, we study the growth of silver deposited by magnetron sputtering on glass substrates pre-coated with three different underlayers: SiO_2, ZnO and a self-assembled monolayer of (3-mercaptopropyl)trimethoxysilane (MPTMS). The films are then covered with a 2-nm barrier titanium film and exposed to reactive oxygen plasma. X-ray photoelectron spectroscopy and time-of-flight secondary ion mass spectroscopy reveal that the degradation process begins with the migration of silver through the top titanium barrier. We quantify the degradation by comparing the atomic content of silver present at the top of the degraded samples. We find that in the case of the ZnO and SiO_2, a significantly higher amount of silver migrates through the top barrier and onto the surface, as compared to the MPTMS-treated surface. We attribute this difference to the chemisorption of silver atoms to the MPTMS layer.

7.2 Introduction

Metal-based transparent conductive films play an important role in modern optoelectronic devices [208, 209] and as radiative heat-reflectors in energy saving applications [92, 210, 211]. Silver films, in particular, possess very high sheet conductivities beyond their percolation thickness as well as good transparency and a neutral transmitted color. Moreover, Ag deposition can easily be scaled

to coat large surfaces with the help of physical vapor deposition techniques such as magnetron sputtering, providing nanoscale uniformity over a large area [99, 212].

The simplest architecture for low-emissivity coatings on glass consists of a dielectric-silver-dielectric stack where the thickness of each layer is tuned to have the highest transmission in the visible and highest reflection in the near-infrared. The bottom layer is typically chosen to promote wetting by the Ag layer. High surface energy metal-oxides such as ZnO [19] or Ag_2O [213] tend to reduce the mobility of sputtered silver atoms and lead to early coalescence stage, a critical requirement for ultra-thin silver films. Alternatively, we can modify the top interface of the underlayer so that it improves the growth of silver. This can be achieved using metal nanoparticles [214] or a very-thin (1-2 nm) metallic interface [22, 215]. One can also use a surfactant to bind the silver atoms through chemisorption. The chemisorbed atoms tend to suppress island formation and increase the film adhesion. One such surfactant is the thiol-based (3-mercaptopropyl)trimethoxysilane (MPTMS), which was previously been shown to help silver and gold thin films growth through the formation of Ag/Au-S bonds [216, 217].

Silver is very sensitive to reactive oxygen and its use requires special precautions in reactive plasma-based processes. A common strategy for protecting silver films is to use a very thin (~2 nm) metallic film (e.g. Ti) as protective layer. When the silver/barrier double-layer is exposed to O_2 plasma during the deposition of the top dielectric, reactive oxygen reacts with the Ti barrier which gradually transforms into sub-stoichiometric titanium dioxide (TiO_x). This intermediate layer has a very low dissolution rate and is essential to protect against corrosion of the underlying film [218]. However, if the barrier thickness is not adequate or if the oxidation process is too severe, the reactive species will lead to silver film failure.

The diffusion of reactive oxygen first occurs along the grain boundaries of the barrier layer and propagates through the whole film [219]. The diffusion of oxygen inside the barrier then generates vacancy migration starting from the outside and propagating towards the underlayer. Once the vacancies reach the barrier/silver film interface, silver atoms in turn start migrating towards the vacancies and leave a void behind, a mechanism labeled as the nanoscale Kirkendall effect [220]. This effect was recently exploited to form hollow nanospheres where the metallic core material was observed to diffuse outwardly to the passivated shell [221, 222]. The Kirkendall effect can occur locally at room temperature due to random atomic motion but becomes more pronounced for temperatures of a few hundred degrees Celsius. In the case of a plasma process, reactive oxygen species are adsorbed at the surface where they can interact with the metallic surface. This interaction between oxygen and the metallic layer is exothermic and can greatly enhance the outward migration of metallic atoms [223]. In this work, we investigate the degradation of protected silver films due to the diffusion of silver through the barrier and show that the use of MPTMS as an underlayer can inhibit such degradation.

7.3 Experimental Section

7.3.1 Sample preparation

Borosilicate (B270) glass substrates with dimensions of 6.45 cm^2 were cleaned using a soap-based detergent. Silicon dioxide films were then deposited using RF magnetron sputtering from a Si target at a $5x10^{-7}$ Torr base pressure, power density of 10 W/cm^2, Ar:O_2 gas ratio of 2:1 and a working pressure of 1.5 mTorr. Zinc oxide seed layers were deposited using DC sputtering at 2.5 W/cm^2 from a Zn target at a working pressure of 2 mTorr and an Ar:O_2 gas ratio of 10:7. To deposit the monolayer of MPTMS, SiO$_2$ samples were first subjected to a directional O$_2$ plasma (a power of

6W applied to the substrate holder with only O_2 gas inside the chamber) to hydrolize the surface. The samples were then taken out of the process chamber and immediately immersed inside an MPTMS solution (5% v/v of MPTMS in toluene) in ambient air and sealed at room temperature for 30 minutes. The samples were then taken out of the mixture and washed with toluene to remove excess MPTMS and annealed in vacuum at 100 °C for 16 hours. Finally, a thin Ag film was sputtered simultaneously on all three seed layers (SiO_2, ZnO and MPTMS-treated SiO_2) and covered with a Ti barrier layer.

7.3.2 Degradation under exposure to oxygen plasma

To expose the Ag/Ti bi-layers to reactive oxygen, a plasma was generated by applying an RF power density between 4 and 8 W/cm^2 on a Si target inside the process chamber at a working pressure of 10 mTorr and an $Ar:O_2$ gas ratio of 2:1. The low and high power density on the target modifies the generation rate of reactive oxygen species within the plasma to create a lower and higher oxidizing environment. The distance between the plasma source (the target) and the substrate holder was 70 cm. The shutter on the target was kept closed to prevent deposition and no bias was applied on the substrate holder. The degradation tests were conducted simultaneously with all samples on the rotating substrate holder.

7.3.3 Sample characterization

In-situ, optical characterization during deposition was performed using an M-2000 ellipsometer (J.A. Woollam) fixed on the sputtering chamber at a 70° incident angle with a spectral range of 190-1650 nm. Electrical measurements were done using contactless sheet resistance measurements immediately after taking the samples out of the process chamber.

For surface analysis, X-ray photoelectron spectroscopy (XPS) was conducted on degraded and as-deposited samples. The analyzed surface was 2 mm x 3 mm and the Mg Kα X-ray beam source was either normally incident to the sample or at grazing angle to reduce to a probing depth from ~5-10 nm to ~1 nm. When required, the surface of the samples was etched using an Ar^+ gun inside the vacuum chamber. The survey scans were taken at 1 eV steps up to 1200 eV.

For elemental depth profiling, Time-of-Flight Secondary Ion Mass Spectrometry (TOF-SIMS) was used. A Bi^+ primary ion source was first used to probe an area of 50×50 μm^2 for secondary ions mass spectra. The depth profiling was then performed using an O^{2-} source taken over an area of 500×500 μm^2.

7.4 Results and Discussion

Figure 7.1 (a) shows *in-situ* real time monitoring results of silver growth on a SiO$_2$ layer. We see that the optical properties shift from absorbing (a dip in the Ψ spectra) due to nano-island formation to fully reflective film for increasing thicknesses (a straight line approaching 45°).
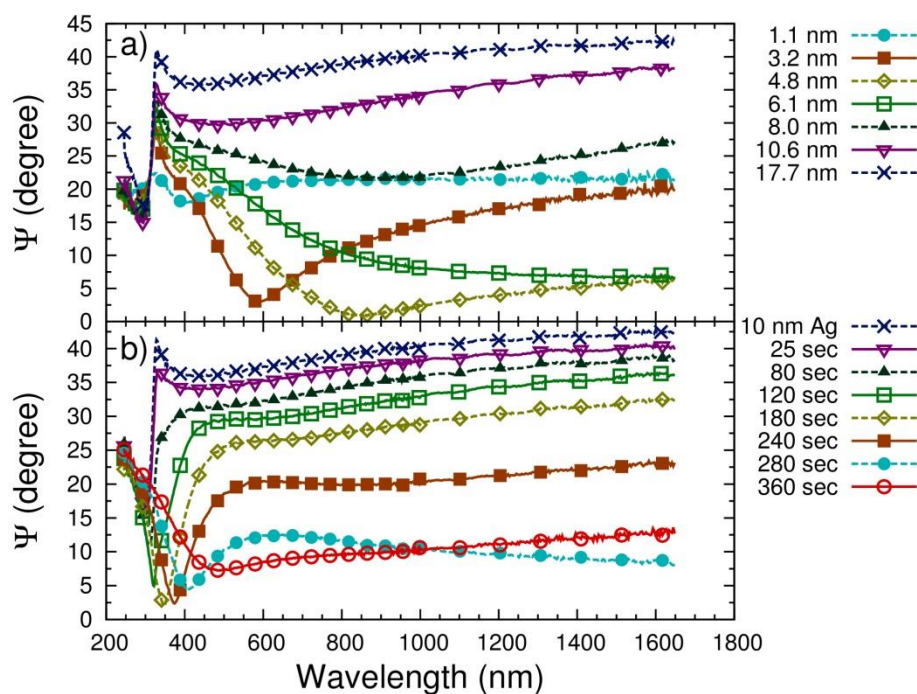
Figure 7.1 : (a) *In-situ* ellipsometry during silver growth using magnetron sputtering on a glass substrate. Optical properties change from an absorbing state (a dip in the Ψ spectra) to a fully reflective film. (b) Exposure of bare Ag film to reactive oxygen plasma. One can see the optical properties change within a few seconds as the film becomes oxidized.

In the presence of reactive oxygen, thin silver rapidly degrades and loses its reflective (and conductive) behavior. Figure 7.1(b) shows the evolution of Ψ when a 10 nm thin silver film is exposed to reactive plasma inside the process chamber. A very rapid change in the ellipsometric data shows the transition from a reflective film to an oxidized compound. In order to prevent this rapid oxidation, a thin metallic (Ti) barrier is deposited on top of the silver film. Figure 7.2 shows an *in-situ* ellipsometry measurement during oxidation using two different power densities applied

on the target (4 W/cm^2 and 8 W/cm^2) in order to generate low and high density of reactive oxygen inside the plasma.

We see from Figure 7.2(a) that when the Ti thickness is adequate for the oxidizing environment, the reflective behavior of the silver film is preserved, and that the thin Ti layer acts as a passive layer preventing the exposure of the silver film to reactive species. In Figure 7.2(b), we increase the applied power on the plasma source from 4 W/cm^2 to 8 W/cm^2. In this case the oxidizing environment is too severe and the barrier thickness is not adequate. This higher power density will be used for all subsequent degradation tests. Even for thin Ti layers, one can observe that there is initially a holding period of a few seconds (up to 80s in this case) but eventually the reactive species reach the silver film and the degradation starts.
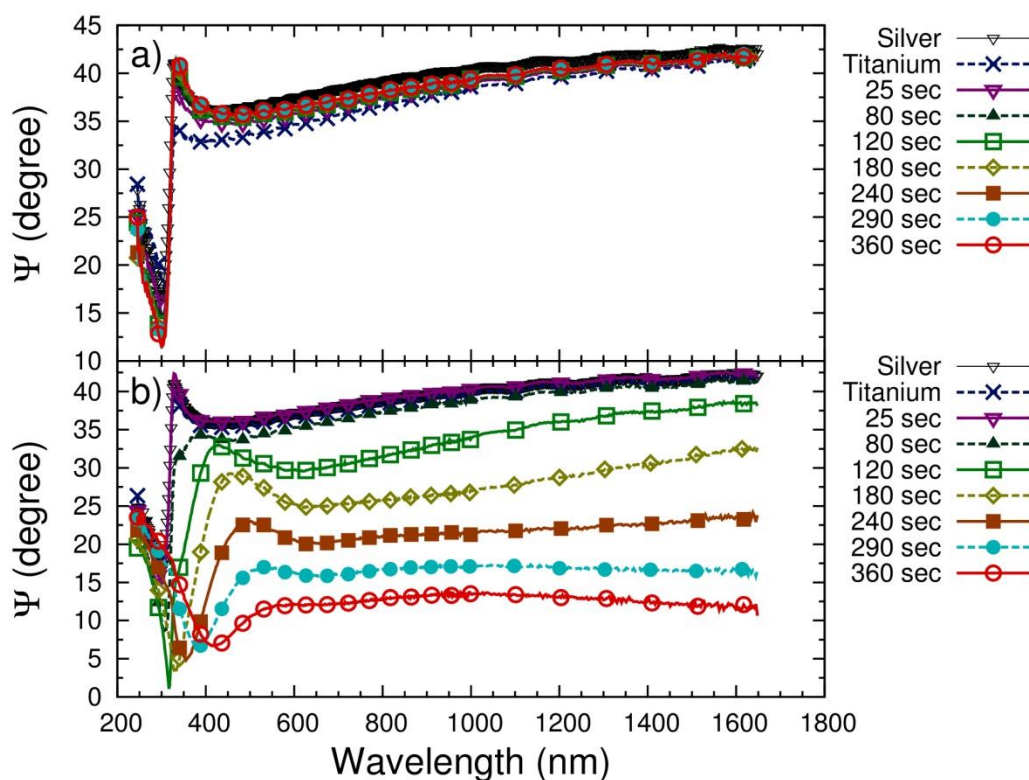
Figure 7.2 : *In-situ* ellipsometry during exposure of a bi-layer of Ag (10nm)/Ti (2nm) film to a reactive O_2 plasma. (a) The Ti barrier thickness is sufficient to prevent degradation of the silver film for low power plasma applied on the target (180 W). (b) The test is repeated with the plasma power on the target increased to 350W and the silver film eventually degrades.

Figures 7.1 and 7.2 underscore the need to protect the silver film using a passivating layer. The thickness and exposure time presented here are used to study the degradation mechanism, rather than achieve ultimate values. In Figure 7.2 (a) we see that there is a vertical shift in the Ψ spectra of the Ag-Ti bilayer after exposure to plasma. This is due to the Ti layer gradually taking up oxygen adatoms and oxidizing into a sub-stoichiometric TiO_x compound. Figure 7.3 shows the optical properties of a thin titanium layer (a), the same layer exposed to O_2 plasma for 300 seconds (b) and a fully stoichiometric TiO_2 film (c) for reference.
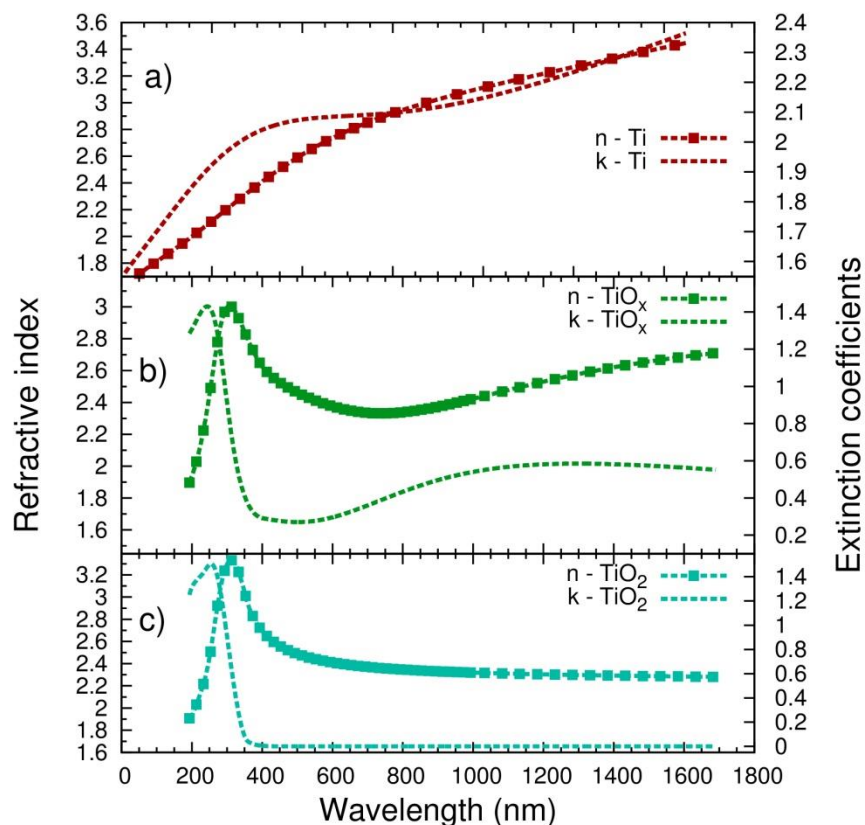
Figure 7.3 : (a) Optical properties of a 3 nm Ti layer (b) Ti layer exposed to oxygen plasma for 300 seconds (c) Fully stoichiometric TiO$_2$ layer.

For a silver film, the optical properties are deeply correlated to the electrical conductivity [224]. Figure 7.4 shows the sheet resistance of bi-layers of Ag/Ti (10 nm Ag and 2 nm Ti) exposed to O$_2$ plasma generated from a power density of 8 W/cm^2 on the Si target. We see that the stack is conductive up to 120 seconds of exposure, but it degrades as the oxidation time is increased. The preliminary decrease in the sheet resistance is due again to the oxidation of the titanium barrier.
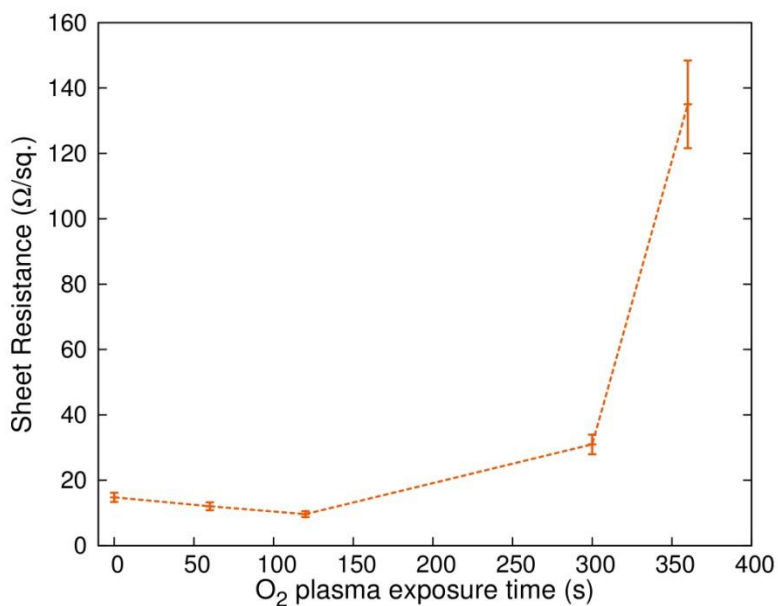
Figure 7.4 : Sheet resistance of Ag/Ti bi-layer exposed to O_2 plasma. There is an initial decrease in the sheet resistance as the Ti barrier becomes oxidized. Eventually the exposure leads to degradation of the silver film.

To confirm that the degradation of silver films in the presence of reactive oxygen is caused by surface migration of silver atoms, Figure 7.5 shows the XPS survey data of a non-degraded and degraded Ag/Ti sample deposited on SiO_2.
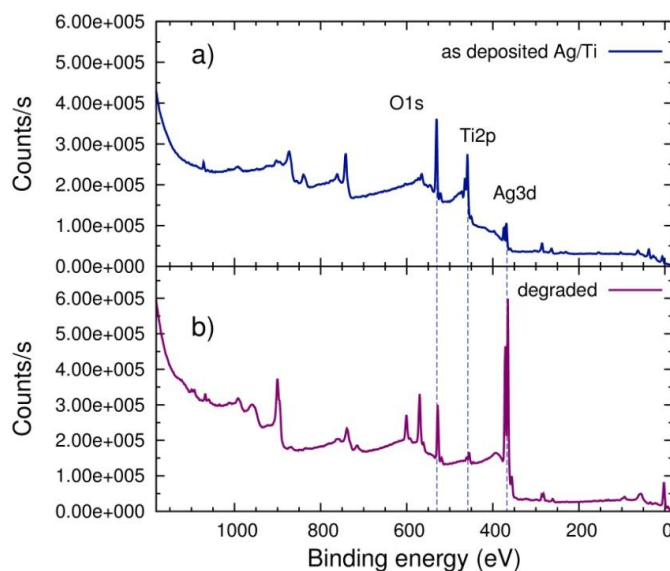
Figure 7.5 : XPS survey data of Ag/Ti bi-layer before (a) and after (b) degradation with O_2 plasma. We see a great increase of the Ag atomic content on the surface after sample degradation accompanied by a decrease in Ti atomic content.

The increase of the Ag3d orbital peak in Figure 7.5 for the degraded sample clearly indicates surface migration of Ag atoms through the Ti barrier. The atomic percent content of Ag goes from 5.4% of the total elements present on the surface before degradation to 25.9%. From the Ti2p orbital peak, the atomic percent of Ti goes from 16.2% before oxidation to 2.7% after. If we probe the first nanometer on the surface using a grazing angle of 70°, the results are 2.0% of Ag before and 23.4% after degradation. For Ti we have 10.7% and 0.6% atomic percent before and after degradation, respectively. For the O1s orbital we have a 55.4% atomic content before and 41.5% after the degradation. The results of the atomic content according to each orbital are presented in Table 7.1. We note that the Ag3d, Ti2p and O1s orbitals constitute on average 80% of the surface composition, while carbon (C1s) and sodium (Na1s) orbitals make up for the rest.

Table 7.1 : Surface elemental content (at. %) of different orbitals for as-deposited and degraded Ag-Ti bi-layers at incident and grazing angle.

Orbitals	Binding energy (eV)	as deposited (at. %) 0º /70º	degraded (at. %) 0º/70º
Ag3d	367.2	5.4/2.0	25.9/23.4
Ti2p	457.8	16.2/10.7	2.7/0.6
O1s	529.9	55.4/41.5	41.5/35.0

We see from Figure 7.5 and Table 7.1 that the surface of the degraded sample is Ag-rich and containing very little Ti. To further prove this migration effect, we have etched a degraded sample inside the XPS chamber and repeated the survey scan. The results are presented in Figure 7.6. By looking at the Ag and Ti peaks, we clearly see that the more we etch the surface the more the Ti content compared to the Ag content increases; this indicates that the Ti atoms are buried under the top-migrating Ag atoms.
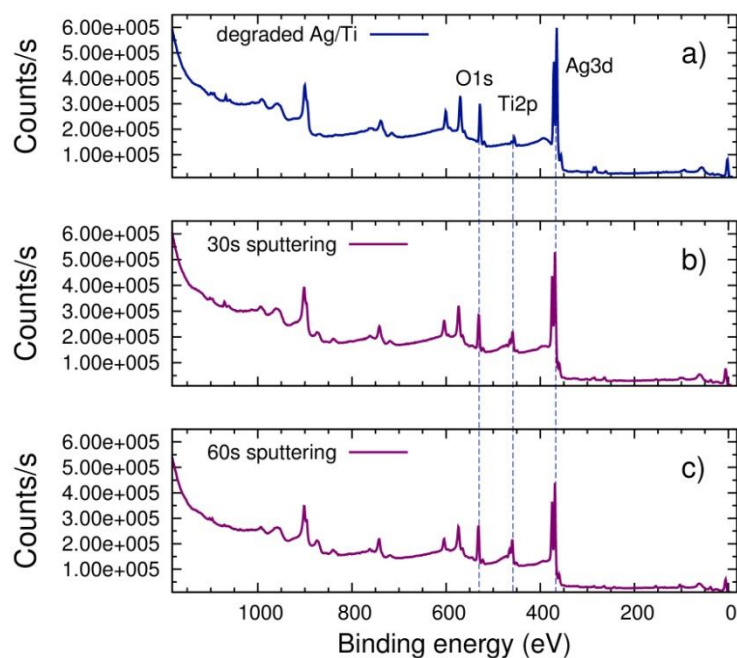
Figure 7.6 XPS survey data of degraded Ag/Ti sample (a) and subsequent *in-situ* sputtering of the surface (b and c). There is a decrease in the Ag atomic content and an increase of the Ti atomic content following the gradual sputtering.

The atomic concentrations on the surface of the degraded sample before and after sputtering for different times are presented in Table 7.2.

Table 7.2: Surface elemental composition (at.%) from survey scans of the degraded bi-layer after 30 seconds and 60 seconds of *in-situ* etching.

Orbitals	Binding energy (eV)	degraded (at. %)	30s sputtering (at. %)	60s sputtering (at. %)
Ag3d	367.2	26.0	26.3	21.9
Ti2p	457.8	3.9	11.1	14.9
O1s	529.9	44.7	45.7	50.8

To confirm the profile distribution of each layer before and after degradation, TOF-SIMS scans were conducted and are presented in Figure 7.7. The samples chosen for the TOF-SIMS scans are the same that were presented previously in Figure 7.5. We see in Figure 7.7 that before degradation takes place, the interfaces are well separated, and no major diffusion process takes place. Once the reactive oxygen gets through the barrier, however, there is intermixing between all Ag, Ti, TiO_x interfaces and we find Ag and AgO species composing the very first layers of the surface.

Now that we have established that Ag atoms migrate during degradation due to reactive species generated in the O_2 plasma, we can study the effect as a function of the choice of underlayer. We have chosen a ZnO seed layer to increase the wettability of the impinging Ag atoms. Because of the higher surface energy, the atoms coalesce much sooner than with SiO_2. However, aside from the reduced mobility leading to early coalescence, the sticking mechanism of the silver atoms on the ZnO is based on physisorption where no chemical bonds are formed at the surface. The other surface chosen is a MPTMS-treated SiO_2 layer. In this case, we obtain sulfur bonds on the surface which are readily available to bind to the sputtered silver atoms so that the mobility is greatly reduced, leading to a rapid coalescence as well as strong adhesion at the Ag/MPTMS/SiO_2 interface.
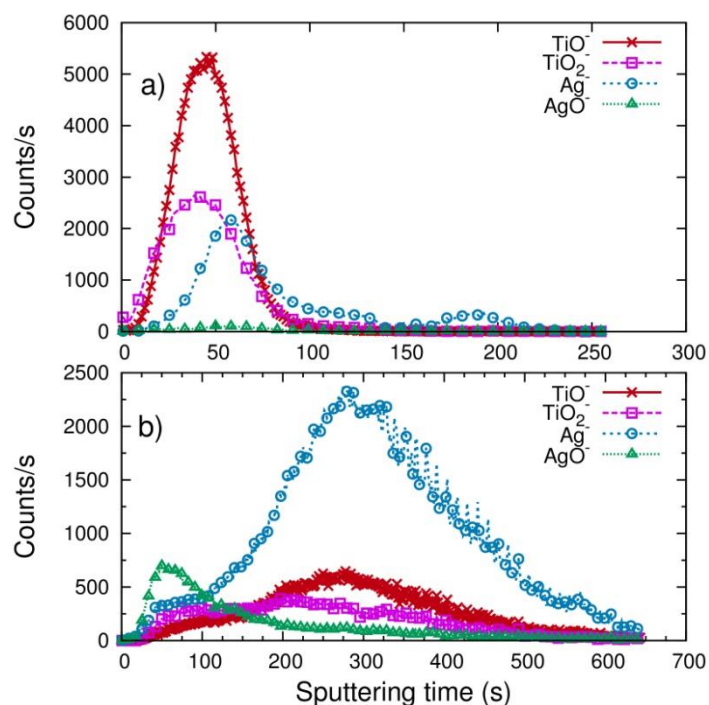
Figure 7.7 : TOF-SIMS scan on non-degraded (a) and degraded (b) Ag/Ti bi-layers. The interfaces are well separated before degradation starts (a) and there is a strong intermixing after the degradation has occurred (b). Moreover we see in (b) that Ag and AgO species are present on the top interface.

Figure 7.8 shows a grazing angle XPS survey scan results for the same degradation tests done on Ag/Ti bi-layer deposited on SiO_2, ZnO and MPTMS underlayers. For the SiO_2 and ZnO seed layers, we see that after degradation the Ti peak is barely visible due to high signal coming from the Ag3d orbitals of the accumulated silver on the surface. For the MPTMS seed layer, both the Ag3d and Ti2p peaks are visible after degradation.

To obtain a numerical comparison between the samples, we can use the ratio of Ag/Ti for the test before and after degradation. These numbers are reported in Table 7.3 as well as the sheet resistance for the samples before and after degradation.
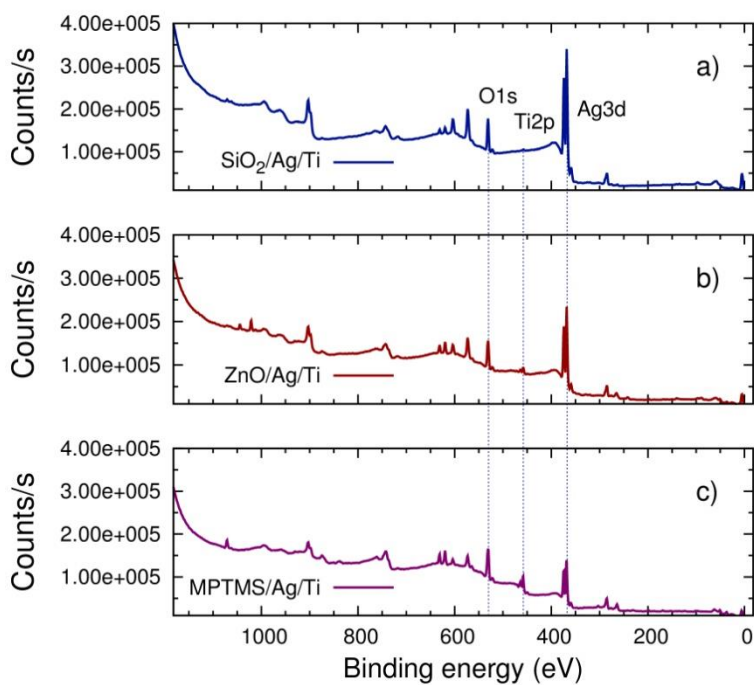
Figure 7.8 : XPS survey data at grazing angle (70°) for SiO_2, ZnO and MPTMS underlayers. The Ti2p peak is mostly visible for the MPTMS-tread SiO_2 sample, due to a reduced amount of Ag migrating to the surface.

Table 7.3: Elemental composition (at. %) obtained from XPS suvey scan at 70° grazing angle and Ag/Ti ratio for as-deposited and degraded bi-layers on different seed layers. We see that the MPTMS-treated surface has the lowest Ag content on the surface after degradation and the lowest Ag/Ti ratio.

As-deposited	SiO$_2$/Ag/Ti (15.3 Ω/□) (at. %)	ZnO/Ag/Ti (12.8 Ω/□) (at. %)	MPTMS/Ag/Ti (12.4 Ω/□) (at. %)
Ag3d	2.0	2.8	1.4
Ti2p	10.7	9.5	11.2
Ag/Ti	**0.2**	**0.3**	**0.1**
Degraded	SiO$_2$/Ag/Ti (170 Ω/□) (at. %)	ZnO/Ag/Ti (19.4 Ω/□) (at. %)	MPTMS/Ag/Ti (17.5 Ω/□) (at. %)
Ag3d	23.4	16.7	9.0
Ti2p	0.6	3.2	4.9
Ag/Ti	**39.0**	**5.2**	**1.8**

The MPTMS seed layer also provides better electrical properties of the thin silver films before and after the degradation. Over the course of 17 deposition tests, the MPTMS/Ag/Ti stacks had on average a sheet resistance of 12.0±2.0 Ω/□ whereas the ZnO/Ag/Ti stack had an average of 13.0±3.0 Ω/□. Moreover, we see in Table 7.3 that after the degradation, the sheet resistance for the selected samples goes from 12.4±1.0 Ω/□ to 17.5±2.0 Ω/□ for the MPTMS case and from 12.8±1.0 Ω/□ to 19.4±2.0 Ω/□ for the ZnO seed layer. For the SiO$_2$/Ag/Ti stack, the sheet resistance went from 15.3±1.0 Ω/□ to 170.0±20.0 Ω/□ after oxidation. Regarding the Ag/Ti ratio on the very top of the samples, we have 39 times more silver than titanium for the SiO$_2$ sublayer, 5.2 times more for the ZnO layer, and only 1.8 times more for the MPTMS seed layer. This was expected from Figure 7.8 where the Ti peak is barely visible for the SiO$_2$ and ZnO sublayers and more apparent

for the MPTMS seed layer, suggesting that the MPTMS treatment helps preventing atomic silver migration.

7.5 Summary and Conclusions

In this work we have confirmed that the degradation mechanism of Ag/Ti planar bi-layers follows the Kirkendall effect at the nanoscale, where the core metallic atoms diffuse outwardly towards the passivating layers in the presence of reactive species. We have shown that this degradation can occur during a reactive process if the barrier layer fails or if the films are exposed to a highly corrosive environment. To prevent the migration (and degradation), we have used a thiol-based surfactant (MPTMS) to bind the silver atoms to the surface onto which they are sputtered. We show that chemisorptions greatly reduces the migration of silver atoms to the surface, up to 2.5x less compared to physisorbed atoms on a high-surface energy seed layer (ZnO) and 20x less compared to a low-surface energy seed layer (SiO_2). We suggest that these findings can apply to other bi-layer systems (core-shell or planar) with different metals and present a long-term solution against the degradation at metallic interfaces in a corrosive environment.

CHAPTER 8   IN-SITU OPTICAL MONITORING OF HIGHLY TUNABLE CORE-SHELL SILVER NANOPARTICLES SYNTHESIZED BY MAGNETRON SPUTTERING

8.1 Foreword

In this Chapter we present an approach to synthesize highly absorbing silver core-shell nanoparticles thin films deposited by magnetron sputtering. By way of optical monitoring using *in situ* real time spectroscopic ellipsometry, we demonstrate how to tune the absorption peak of the surface plasmon resonance of the nanoparticles and how to retain the optical properties after the deposition process using substrate heating. We fabricate silver core-shell nanoparticles by avoiding exposure to reactive oxygen. By covering the nanoparticles with a thin metallic layer and subsequently inserting a reactive gas inside the process chamber we can gradually change the metallic layer to a metal-oxide or metal-nitride compound. We demonstrate this technique for Ag/SiO$_2$, Ag/SiN, Ag/TiN and Ag/ZnO core-shell nanoparticles.

8.2 Introduction

Plasmonic nanostructures have gathered a lot of interest in recent years due to the unique interactions between electromagnetic waves with metallic surfaces. Incident light coupling to the collective oscillations of the free electrons available at the boundaries of a metallic medium gives rise to a propagating, decaying surface wave called a surface plasmon. Close to the plasma frequency, the propagating wave acquires a very large wavevector allowing waveguiding in nanostructures much smaller than the wavelength of incident light. If the nanostructure dimensions are such that the wave is spatially confined, incident radiation couples to the surface-boundary electrons, but the propagation is restricted to a sub-wavelength volume in which the electric field is greatly enhanced. Due to the strong absorbing cross-section and availabilities of free electrons contained in a small volume, these metallic nanostructures are found in a multitude of devices and applications such as nano-antennas[225], enhancing catalytic reactions[226], water-splitting for hydrogen production [105, 227], and solar absorbing thin films [228]. However, the synthesis of

self-assembled nanoparticles on large scale can be a complex task as most techniques rely on wet chemical methods.

Metallic nanostructures can be synthesized in a wide variety of processes depending on the shape, size and structure that is desired. One way of synthesis is by way of physical vapour deposition techniques such as magnetron sputtering which allows for very precise control over the effective mass-thickness of the deposited film. The growth of silver on dielectric surfaces has been extensively studied and is known to follow a Volmer-Weber type of growth [24], where the silver atoms diffusion and nucleation leads to a self-assembled island formation. Noble metals gold and silver as well as copper follow this growth mechanism. Depending on the surface free energy and the surface temperature, these nano-islands take a spheroidal shape with a base diameter ranging from few nanometers to a few tens of nanometers and a height of a few nanometers.

The light-matter interaction at the early growth stage is mainly governed by surface plasmon excitations. The electromagnetic surface oscillations of the free electrons at the boundaries of nano-islands are called local surface plasmons (LSPs). The resonant frequency of these nanoparticles (NPs) depends on their size and shape, the surrounding medium as well as the distance between neighbouring particles[229]. It is possible to affect the growth process by heating the surface during deposition of metallic films. The additional heat promotes the atomic diffusion onto the surface which influence the growth process of the nano-islands [230].

In this work, we present a synthesis pathway to obtain nano-islands embedded in a thin medium giving the nanoparticles a core-shell like structure. Using in-situ optical monitoring, we demonstrate how to tune the LSP resonance and how to control the stoichiometry of the outside shell. These two parameters allow us to obtain nanoparticles with a wide range of optical properties.

8.3 Nanoparticles synthesis

In the present work, thin silver nanoparticles (NPs) were deposited inside a high-vacuum process chamber with a base pressure of 7×10^{-8} Torr equipped with an M-2000 ellipsometer (J.A Woollaam) for *in-situ* monitoring. The ellipsometer is installed at a fixed angle of 70° and the ellipsometry parameter Ψ is acquired every 2.4 seconds. The ellipsometry variable Ψ is the ratio of the intensity of the reflected *p*-polarized light over *s*-polarized light ($\frac{r_p}{r_s}$). For the synthesis of Ag

core-shell structure, silver films were first deposited from a silver target by applying a power density of 1.3 W/cm^2 at a 4 millitorr pressure using Ar gas. To avoid oxidation of the nanoparticles by ambient oxygen for ex-situ characterization, 5 nm thin zinc stannate (ZnSnO$_x$) films were used to cap the silver nanoparticles. The ZnSnO$_x$ was obtained by sputtering from a ZnSnO$_x$ dielectric target using Ar gas to avoid the presence of reactive oxygen inside the plasma. For core-shell structures, a thin Si, Zn or Ti metallic film was sputtered on the silver NPs and oxygen or nitrogen was subsequently inserted inside the plasma after the deposition was completed. The reactive species generated this way reacted with the outer layer to produce a core-shell structure with the silver NPs. The *ex-situ* optical characterization was obtained using a Perkin-Elmer Lambda 1050 spectrophotometer.

8.4 Results and Discussions

8.4.1 Core-shell nanoparticles

Figure 8.1 shows the absorption spectra of Ag NPs deposited on borosilicate glass and protected with a 5 nm layer of ZnSnO$_x$. We see the signature of the LSP absorption in the visible range due to the presence of Ag nanoparticles. As the nanoparticles grow, the absorption increases, red shifts and broadens.
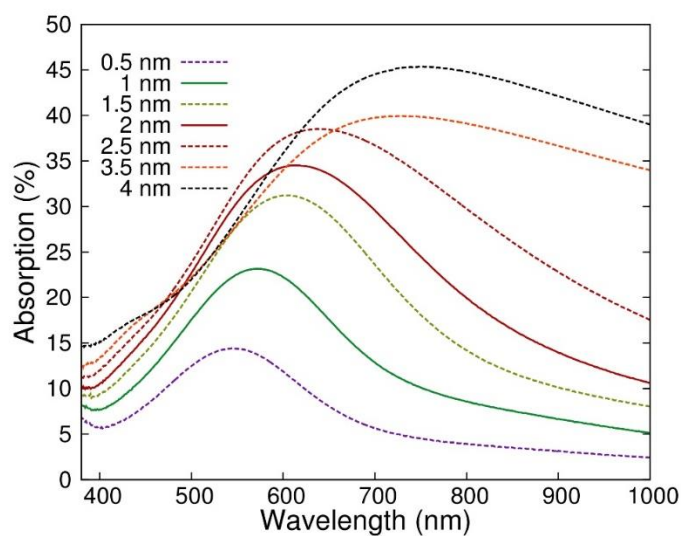
Figure 8.1 Absorption spectra of Ag nanoparticles grown on borosilicate and capped with a layer of ZnSnO$_x$. The absorption red shifts and broadens as the particles grow.

A common way to protect Ag films is by having a sacrificial layer (usually a metal such as Ti, Ni or Cr) coated on top of the film and then proceed to deposit an oxide by way of reactive sputtering. During the deposition of the top oxide layer, the sacrificial metallic layer takes up the reactive oxygen generated inside the plasma and self-passivates. Figure 2 shows *in-situ* monitoring on Ag NPs during such process. First, a thin Ag film is deposited and the ellipsometry data taken after 30 seconds of deposition from the Ag target on a borosilicate glass substrate. The deposition rate has been adjusted to 0.1 nm/s such that an effective mass thickness of 3 nm of silver is obtained. We notice the dip in the Ψ as the signature of the LSP at 570 nm. Following the Ag NPs deposition, a 3 nm sacrificial Ti film was sputtered on top. We notice a broadening in Ψ following the Ti layer deposition as the metallic medium changes the plasmonic resonance of the Ag NPs. Next, an O_2 plasma is generated inside the process chamber by applying a 2 W/cm^2 power density on a test target (with the shutter closed to avoid deposition) and the sample was left to react with the reactive oxygen species. As the Ti layer passivates to form a TiO_x layer, we see a gradual red shift and a narrowing of the Ψ spectrum. This transition occurs as we change the surrounding medium of the NPs from a metallic to a dielectric layer, accompanied by changes in the LSP resonance of the thin film. However, we can see that the oxidation process can destructively alter the optical properties if the reactive oxygen gets through the Ti barrier to react with the silver NPs. This results in the disappearance of the LSP peak from the Ψ spectra.
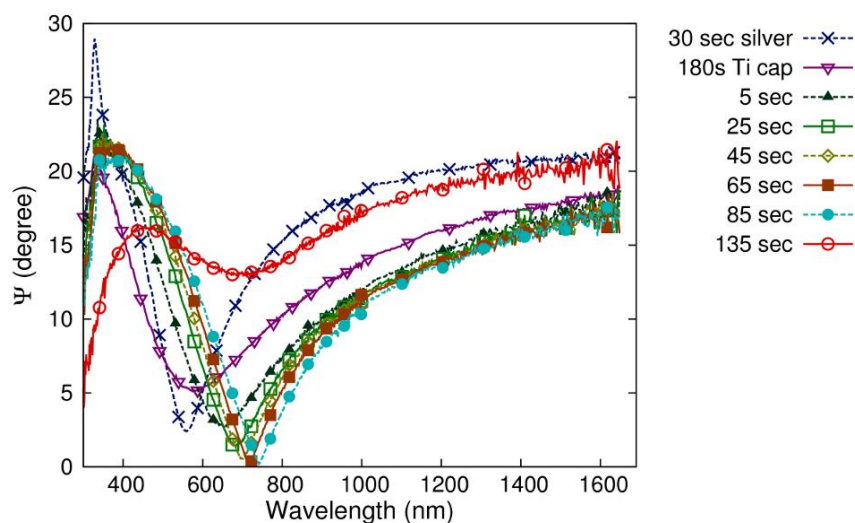
Figure 8.2 : In-situ real-time ellipsometry of the oxidation process of a titanium barrier on Ag NPs. We see an initial broadening of Ψ after the deposition of the titanium barrier and a red-shift in the LSP absorption peak as the barrier is exposed to a reactive O_2 plasma. After 2 minutes of the oxidation process, the reactive O_2 reaches the silver nanoparticles and the film loses the characteristic LSP absorption.

By carefully monitoring the oxidation (or nitriding) process to avoid damage to the buried silver core, one can in principle change the surrounding shell to any metal-oxides (or metal-nitrides). Figure 8.3 shows the same experiment done for four different core-shell structures using Si, Ti and Zn targets followed by the oxidation or nitriding process.
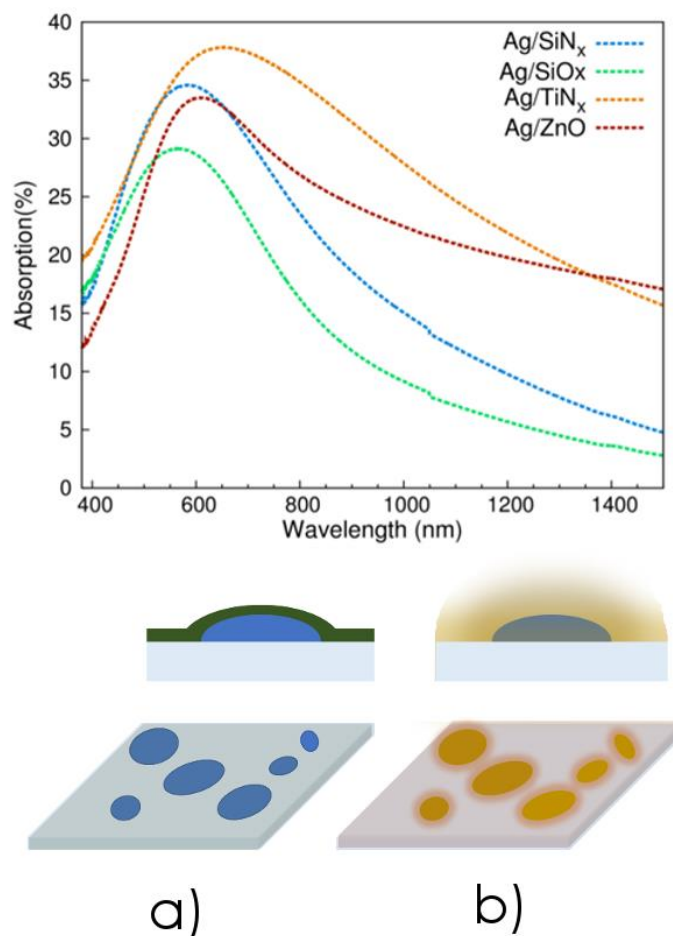
Figure 8.3 : (Top) absorption spectra for different core-shell nanostructures obtained by oxidizing and nitriding a sacrificial Si, Ti and Zn barrier (Bottom) Schematic of core-shell particle synthesis. Silver nanoislands are covered with a sacrificial layer (a) and exposed to a reactive plasma (b).

8.4.2 LSP *in-situ* monitoring

Changing the outer shell of the Ag NPs allows for tunability in the optical properties. It is also possible to modify the optical properties by changing the size distribution of the Ag NPs. One possibility is to heat the substrate in order to increase the diffusion of the sputtered silver atoms on the surface. The additional diffusion time of the Ag atoms allows the formation of agglomerated silver islands with a more uniform distribution. Figure 8.4 shows the absorption spectra of nanoparticles deposited on borosilicate glass at room temperature (RT) and at 300°C and covered

with a ZnSnO$_x$ capping layer. We see that by heating the substrate we obtain a narrower absorption as well as an increased extinction cross-section which leads to a stronger absorption.
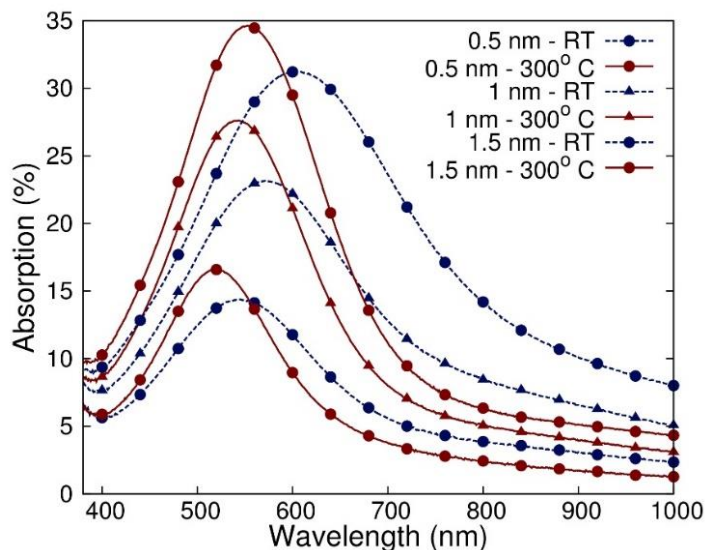
Figure 8.4 : Absorption spectra of silver NPs deposited at room temperature (RT) and at 300°C on borosilicate glass and capped with a ZnSnO$_x$ layer. The absorption is narrower and greater when the substrate is heated.

We saw in Figure 8.1 that using *in-situ* real time monitoring allows one to observe the absorption peak maximum (corresponding to a minimum in the reflectivity spectrum, given by the ellipsometry variable Ψ). Figure 8.5 shows the LSP resonance as a function of Ag deposition time for different substrate temperatures. Following the deposition process, the *in-situ* monitoring was continued. One striking difference between the different deposition temperatures during growth of the thin films is the rate of change of the LSP resonance. For deposition at room temperature and at 100°C the LSP resonance increases rapidly above 550 nm after 30 seconds of the process (marked by the dashed vertical line). At 300°C, the increase is slowed down to 530 nm, and at 380°C it is further slowed down to 460 nm. This means that by changing the surface temperature, we can control the rate of change of the LSP resonance and fine tune the absorption peak position.

Moreover, once the deposition process is stopped, we observe a blueshift in the LSP resonance which is more pronounced for the samples deposited at room temperature, 100°C and 300°C. Interestingly, at 380°C, there seems to be no shift in the LSP resonance, pointing to a critical temperature where the nanoparticles properties are stabilized post-deposition. Many processes such

as Ostwald ripening and shape and stress relaxation can occur when mobile atoms are present on a surface[231, 232]. The shape relaxations occur when the atoms on the outside of the nanoparticles escape and subsequently attach to a thermodynamically stable site. The process continues until all unstable atoms reach a stable position [233].

In all cases, the silver atoms and clusters re-arrange in order to reach a thermodynamic equilibrium. These effects inevitably lead to a change in the optical properties such as the resonance blue-shift observed in Figure 8.5.
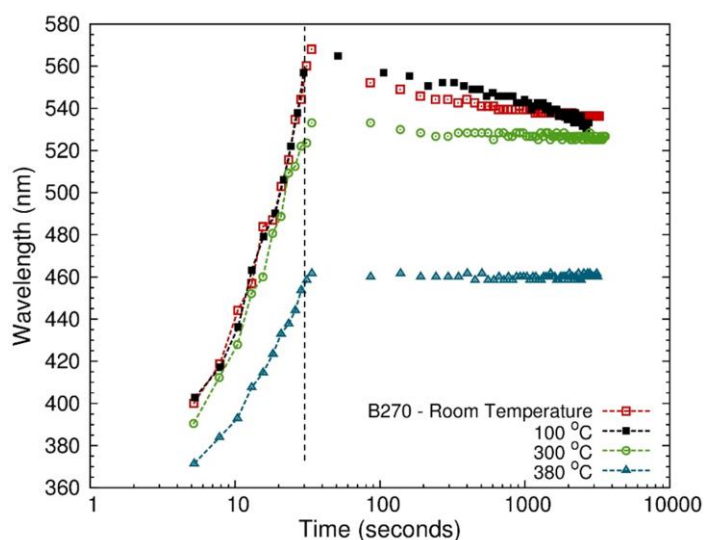
Figure 8.5 : Optical monitoring during deposition of silver. The minimum in the ellipsometry variable Ψ is plotted as a function of deposition time. The dashed line represents the end of the deposition process. The optical monitoring past the deposition process shows a blue-shift in the LSP absorption for temperatures below 380 °C.

The difference in the particles size and distribution can also be observed by atomic force microscopy (AFM). Figure 8.6 shows differences for Ag NPs deposited on borosilicate. For the room temperature sample, the NP exhibit an average height of 3.2 nm and a base diameter of 35 nm. For the 380°C sample, however, the average height is 3.4 nm and the average diameter 29 nm. Therefore, the extra heat reduced the aspect-ratio of the nanoparticles. The additional energy provided to the silver atoms helped them to overcome the kinks and steps of the substrate (and other nanoparticles) which resulted in a decreased base diameter and an increased height.

Moreover, by comparing Figure 8.6 a) and b), we notice that in the heated sample the silver clusters are well separated, and they are more uniform compared to the sample deposited at room temperature. These differences are reflected in the optical monitoring data. Interestingly, the particle size statistics indicates that at high temperature the size distribution is smaller than at room temperature. Here the additional heat can play a role in accelerating the shape relaxation process, where particles that at too large lose outside atoms that diffuse and meet smaller clusters to which they attach to and start to grow larger. This process eventually evens out the size of individual clusters as each atoms find a thermodynamically stable position.
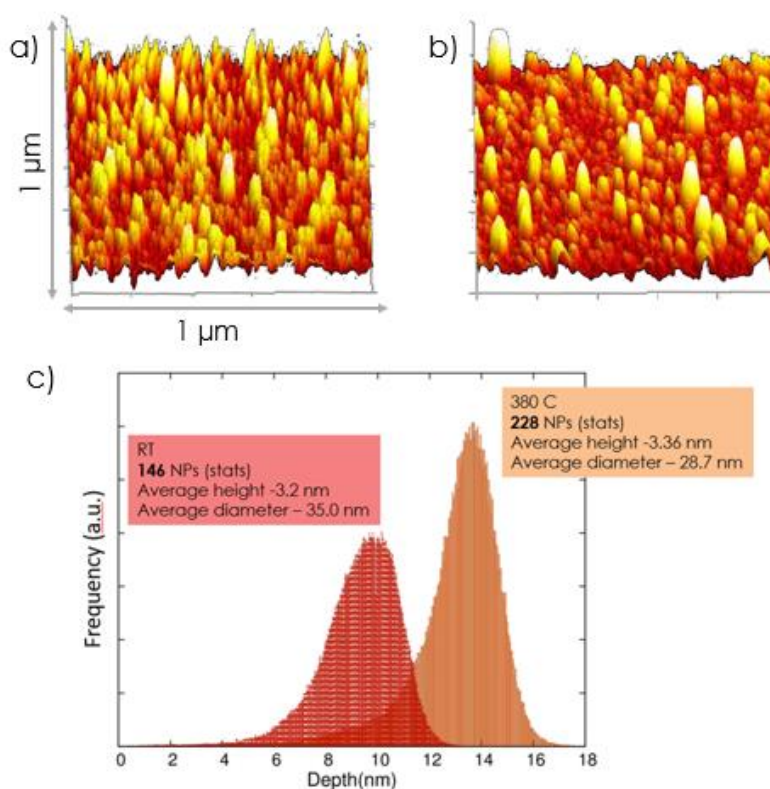
Figure 8.6 : 1 μm x 1 μm AFM images of nanoparticles on B270 glass deposited at room temperature (a) and 380 °C (b). The histogram reveals a smaller base diameter, a smaller size distribution and greater height for the sample deposited at 380°C.

8.5 Conclusions

In summary, we have demonstrated the tunability of Ag core-shell structures using magnetron sputtering and *in-situ* oxidation process. The ability to passivate the outer layer of a core-shell structure provides an additional parameter for the films' optical properties. Moreover, we believe these structures could be used for applications relying on electron injection into the outer shell for chemical reactions and catalysis. The bandgap of the outer oxide (or nitride) shell can be precisely controlled with the process described in this letter and can be useful for opto-electronic applications. Finally, we have demonstrated that for a critical temperature, thermodynamic relaxations effect in silver nanoparticles is inhibited and that the nanoparticles conserve their shapes and optical properties overtime. This can be used in order to obtain precisely the desired LSP resonance during the growth of silver NPs.

CHAPTER 9   CONCLUSIONS AND PERSPECTIVES

9.1 Summary

To conclude our work, we will give a review of the various achievements presented in the previous chapters. As we had stated in the beginning of the thesis, the main objective of this work is to optimize the optical and electrical properties of ultrathin silver films for their long-term use in passive heat-reflecting, low-emissivity glazing. We believe that this goal was achieved through numerous key results and experimental procedures presented in Chapter 5 to Chapter 8.

Our first step was to develop an optical method using *in-situ* ellipsometry to determine with precision the percolation threshold thickness of silver films during growth. The method was extensively used to compare the wetting of silver films on different surfaces in order to facilitate the seed layer selection and obtain the thinnest possible silver films. This methodology is still regularly used in our laboratory and has also permitted various studies on the growth control and optical properties of silver nanoparticles. Initially, all the wetting surfaces studied for silver growth consisted in metal-oxide layers of a few nanometers. Therefore, the bonding mechanism of the silver atoms evaporated on these surfaces was restricted to a physisorption process. By introducing a thiol-based self-assembled monolayer of MPTMS on SiO_2, we were able to obtain ultrathin silver films with bulk-like optical properties. We linked the enhanced electrical and optical properties to the bonding between the sulfur (in thiol form) and silver atoms. Even though this surface treatment is usually applied on silica or glass, we were able to demonstrate its formation on silicon nitride and used it to create a simple SiN/Ag/SiN stack with excellent optical properties.

In a plasma environment, where atomic dissociation and ionization of a reactive gas occur, the rapid degradation of silver can cause irreversible damage to the stack if no protective measures are taken. We have shown that the degradation of silver caused by reactive oxygen takes place by the migration of silver atoms through the top barrier. Using the same MPTMS treatment, we demonstrated that we could inhibit the atomic migration caused by oxygen adsorption on the top barrier. Thus, the reduced amount of silver migrating to the surface was attributed to the chemical bonding between silver and sulfur on the underlying layer after the MPTMS treatment.

Finally, we have investigated the growth and optical properties of silver nanoparticles using *in-situ* ellipsometry. Combining the methodology previously developed, we were able to synthesise silver nanoparticles capped with a layer of oxide (or nitride) to obtain a wide range of optical properties. By monitoring the local surface plasmon resonance of silver nanoparticles during sputtering, we were able to predict the spectral absorption peak as well as monitor the phenomenon of post-deposition diffusion of silver atoms. We discovered that above a specific substrate temperature, the post-diffusion vanished, and the optical properties of the nanoparticles remained stable even after a few hours. By covering the nanoparticles with a metallic layer, we were able to expose the sample to a reactive plasma containing O_2 (or N_2) gas to passivate the outer layer. In this manner, we were able to obtain silver nanoparticles embedded in a capping shell of a metal-oxide (or metal-nitride) with variable stoichiometry. We believe that the results presented throughout this thesis combine into a step towards a better understanding of the seeding mechanism of very thin silver layers, a better understanding of the degradation process that can occur in a reactive atmosphere and a novel approach of fabricating core-shell silver nanoparticles using physical vapour deposition.

9.2 Discussions and perspectives

As we have seen in Chapter 5 and 6, the typical island-type growth of silver films can be supressed through the right seed layer selection. In most cases, the wetting behavior for elements favouring this type of growth (such as Ag, Au and Cu) depends on the free surface energy difference between the seed layer and the deposited material. We saw how Sn inclusions in zinc oxide to form zinc stannate helped with the percolation thickness reduction, due to a more metallic character of the $ZnSnO_x$ layer. Therefore, thin transparent oxides with metallic inclusions, such as aluminum-doped zinc oxide (AZO) [234], boron-doped zinc oxide (ZnO:B) [235, 236], gallium-doped zinc oxide (ZnO:Ga) [237] are all potential candidates for seeding of silver compared to the undoped layers, as well as a multitude of other thin film compositions.

Alternatively, we saw that seeding of silver atoms when a chemical bond was present reduced considerably the percolation threshold thickness. In this case, silver atoms are attached to the available bonds with a higher binding energy than physisorption. One way of initiating these bonds formation was through surface treatment via immersion in a solution containing the MPTMS thiol-based molecule or (in a less efficient way) evaporation of the MPTMS through chamber saturation.

For large scale production, liquid immersion of substrates prior to deposition gives rise to numerous industrial challenges. One approach to this problem is to provide the sulfur bonds by sputtering sulfur containing coatings such as zinc sulfide (ZnS), tin sulfide (SnS_x) [238] or indium sulfide (In_2S_3) [239]. These sulfide compounds could in principle bond to silver atoms and improve the wetting of silver films, as demonstrated for ZnS/Ag/ZnS transparent electrodes [240-242].

The research and advances made in the field of passive low-emissivity coatings could also help the field of active solar-energy coating. As we have previously mentioned, the most recent research on active coatings for solar energy control is focusing on multi-spectral selective coatings, where different elements of the coating architecture interact with either the visible or the near-infrared part of the solar spectrum. In their bleached state, electrochromic coatings cut the income of the solar radiation through absorption. Since this intermediate state is highly emissive, the absorbed radiation is re-emitted, a process that can partially offset the net energy reduction by re-radiating heat inside the building or cause overheating leading to device degradation. By combining the electrochromic device with a low-emissivity coating it becomes possible to prevent the unwanted thermal reradiation [243]. Moreover, we saw that state-of-the-art research on optically active materials (electrochromic and thermochromic) are directed towards nanoparticles having changing properties under an external stimulus. By reducing the dimensions of the thin film materials to nanoparticles, it is possible to either enhance the chromaticity of the device, such as increased thermochromaticity of VO_2 nanoparticles embedded inside a dielectric or find new properties such as plasmon-assisted optical switching using conductive nanoparticles. However, the synthesis of these nanoparticles can be a serious challenge regarding their size distribution, nanostructure and stability. The results presented regarding the growth monitoring of silver islands and the synthesis of core-shell nanoparticles may open new ways to synthesize new nanostructures by enabling control over the size distribution and stoichiometry of the embedding medium. Moreover, it has been demonstrated that ordinary, non-switching metallic nanoparticles can demonstrate optical modulation properties when embedded in an active matrix, such as silver or gold nanoparticles embedded in a VO_2 thin film [244-247].

Besides their use as radiative heat-reflector or optical absorbers in solar energy control coatings, silver nanostructures have also found their way in other energy related areas. The unique properties of plasmonic elements to confine light strongly on the nanoscale has pushed their use in passive

steam generating devices [248], solar thermal collectors [249, 250] and hydrogen producing devices [251]. Silver nanoparticles have also found their way in biomedical applications where their anti-microbial activities are reported [252-254]. The action of silver nanoparticles on their surrounding occurs at the interface, where dissolution, passivation and release of silver ions are the source of chemical activities. The understanding developed throughout this thesis can contribute to further development of these silver nanostructures. The presented core-shell nanostructures can play a catalytic role under sunlight irradiation through hot electron injection between the silver core to the shell/external medium to enhance catalytic reactions. The electronic structure of the outside shell can be controlled through its stoichiometry to influence the semiconducting character. A sub-stoichiometric shell can act as an electron acceptor in contact with the silver nanoparticles and fully oxidized shell as an electron blocking layer. Similarly, we saw that release and migration of silver atoms can be influenced based on the surface treatment prior to the silver deposition. In applications based on the slow release of silver ions, such as nanoparticles drug delivery systems, a suitable surface treatment could delay the release of silver ions before they reach the infected sites.

With certain minor differences, transparent conductive electrodes and low-emissivity windows both share the same goals and challenges. The low-emissivity stacks presented in this thesis were based on planar, continuous thin films. A recent advance in transparent electrodes is the use of silver nanowires and nanogrids [255-258]. Besides keeping the sheet resistance to very low values, these nanostructures demonstrate very high visible transmittance and their use in flexible and stretchable electronics can inspire future low-emissivity coatings.

In conclusion, research activities directed towards the future of energy saving will for the most part keep expanding as the need for energy increases. As we have seen, the energy management inside buildings must continue to improve in order to provide the next generations with more efficient and sustainable infrastructures. Eventually, established technologies such as electrochromic and thermochromic glasses and polymer coatings will take a substantial part of the market due to increased efficiencies and customer preferences compared to passive heat-reflecting windows. However, rather than comparing them as two competing approaches to one solution, we can easily foresee the synergy between active and passive nanostructures combined into one 'multi-purpose' window pane.

REFERENCES

[1]   F. Biroi, *Energy Technology Perspectives 2017*. International Energy Agency, 2017.

[2]   *Transition to Sustainable Buildings: Strategies and Opportunities to 2050* (Energy technology perspectives). OECD, 2013, 2013.

[3]   S. S. D. Arasteh, J. Apte , and M. LaFrance, "Zero Energy Windows," in *ACEEE Summer Study on Energy Efficiency in Buildings*, Pacific Grove, CA, 2006.

[4]   M. V. d. Hoeven, *Technology Roadmap, Energy efficient building envelopes.* International Energy Agency, 2013.

[5]   D. Ürge-Vorsatz and A. Reith, "Monetary Benefits of ambitious building energy policies," Global Buildings Performance Network, 2015.

[6]   R. J. Martin-Palma, L. Vazquez, J. M. Martinez-Duart, and Malats-Riera, "Silver-based low-emissivity coatings for architectural windows: Optical and structural properties," (in English), *Solar Energy Materials and Solar Cells,* vol. 53, no. 1-2, pp. 55-66, May 1998.

[7]   C. G. Granqvist, "Solar energy materials," (in English), *Advanced Materials,* vol. 15, no. 21, pp. 1789-1803, Nov 4 2003.

[8]   K. Ellmer, "Past achievements and future challenges in the development of optically transparent electrodes," (in English), *Nature Photonics,* vol. 6, no. 12, pp. 808-816, Dec 2012.

[9]   I. Crupi, S. Boscarino, V. Strano, S. Mirabella, F. Simone, and A. Terrasi, "Optimization of ZnO:Al/Ag/ZnO:Al structures for ultra-thin high-performance transparent conductive electrodes," (in English), *Thin Solid Films,* vol. 520, no. 13, pp. 4432-4435, Apr 30 2012.

[10]   K. Kim, K. Hong, B. Koo, I. Lee, and J. L. Lee, "Transparency controllable silver-based electrode for flexible optoelectronics," (in English), *Applied Physics Letters,* vol. 102, no. 8, Feb 25 2013.

[11]   T. N. Xu *et al.*, "Photon energy conversion via localized surface plasmons in ZnO/Ag/ZnO nanostructures," (in English), *Applied Surface Science,* vol. 258, no. 15, pp. 5886-5891, May 15 2012.

[12]   S. Morawiec, M. J. Mendes, S. Mirabella, F. Simone, F. Priolo, and I. Crupi, "Self-assembled silver nanoparticles for plasmon-enhanced solar cell back reflectors: correlation between structural and optical properties," (in English), *Nanotechnology,* vol. 24, no. 26, Jul 5 2013.

[13]   J. C. Bian *et al.*, "Mechanisms in photoluminescence enhancement of ZnO nanorod arrays by the localized surface plasmons of Ag nanoparticles," (in English), *Applied Surface Science,* vol. 258, no. 22, pp. 8548-8551, Sep 1 2012.

[14]   J. Xu *et al.*, "Efficiency enhancements in Ag nanoparticles-SiO2-TiO2 sandwiched structure via plasmonic effect-enhanced light capturing," *Nanoscale Res Lett,* vol. 8, no. 1, p. 73, Feb 12 2013.

[15]   A. Zolanvari, H. Sadeghi, R. Norouzi, and A. Ranjgar, "Surface plasmons and optical properties of TiO2/X (X = Au and Ag) nanostructured thin films," *Chin. Phys. Lett.,* vol. 30, 2013.

[16]   S. Schubert, J. Meiss, L. Muller-Meskamp, and K. Leo, "Improvement of Transparent Metal Top Electrodes for Organic Solar Cells by Introducing a High Surface Energy Seed Layer," (in English), *Advanced Energy Materials,* vol. 3, no. 4, pp. 438-443, Apr 2013.

[17]   R. Alvarez, J. C. Gonzalez, J. P. Espinos, A. R. Gonzalez-Elipe, A. Cueva, and F. Villuendas, "Growth of silver on ZnO and SnO2 thin films intended for low emissivity applications," (in English), *Applied Surface Science,* vol. 268, pp. 507-515, Mar 1 2013.

[18]   N. Venugopal and A. Mitra, "Influence of temperature dependent morphology on localized surface plasmon resonance in ultra-thin silver island films," (in English), *Applied Surface Science,* vol. 285, pp. 357-372, Nov 15 2013.

[19]   M. Arbab, "The base layer effect on the d.c. conductivity and structure of direct current magnetron sputtered thin films of silver," *Thin Solid Films,* vol. 381, no. 1, pp. 15-21, 2001.

[20]   A. Q. Chen and M. Deutsch, "Tunable asymmetric reflectance in silver films near the percolation threshold," (in English), *Journal of Applied Physics,* vol. 109, no. 9, May 1 2011.

[21]   A. A. Schmidt, H. Eggers, K. Herwig, and R. Anton, "Comparative investigation of the nucleation and growth of fcc-metal particles (Rh, Ir, Ni, Pd, Pt, Cu, Ag, Au) on amorphous carbon and SiO2 substrates during vapor deposition at elevated temperatures," (in English), *Surface Science,* vol. 349, no. 3, pp. 301-316, Apr 10 1996.

[22]   W. Chen, M. D. Thoreson, S. Ishii, A. V. Kildishev, and V. M. Shalaev, "Ultra-thin ultra-smooth and low-loss silver films on a germanium wetting layer," *Opt Express,* vol. 18, no. 5, pp. 5124-34, Mar 1 2010.

[23]   H. S. Yang, B. Qu, S. B. Ma, Z. J. Chen, L. X. Xiao, and Q. H. Gong, "Indium tin oxide-free polymer solar cells using a PEDOT:PSS/Ag/PEDOT:PSS multilayer as a transparent anode," (in English), *J Phys D Appl Phys,* vol. 45, no. 42, Oct 24 2012.

[24]   A. Anders, E. Byon, D. H. Kim, K. Fukuda, and S. H. N. Lim, "Smoothing of ultrathin silver films by transition metal seeding," (in English), *Solid State Communications,* vol. 140, no. 5, pp. 225-229, Nov 2006.

[25]   R.A. Maniyara *et al.*, "Tunable plasmons in ultrathin metal films," *Nature Photonics,* vol. 13, pp. 328-333, 2019.

[26]   Yan-Gang Bi *et al.*, "Ultrathin Metal FIlms as the Transparent Electrode in ITO-Free Organic Optoelectronic Devices," *Advanced Optical Materials,* vol. 7, p. 1800778, 2019.

[27]   J. Yun, "Ultrathin Metal films for Transparent Electrodes of Flexible Optoelectronic Devices," *Advanced Functional Materials,* vol. 27, no. 18, p. 1606641, 2017.

[28]   B. A. and K. J.W., "Diffusion and Conduction in Percolation Systems," in *Diffusion in Condensed Matter*. Berlin: Springer, 2005.

[29]   M. Walther, D.G. Cooke, C. Sherstan, M. Hajar, M.R. Freeman, and F. A. Hegmann, "Terahertz conductivity of thin gold films at the metal-insulator percolation transition," *Physical Review B,* vol. 76, p. 125408, 2007.

[30] Y. D. Yin, R. M. Rioux, C. K. Erdonmez, S. Hughes, G. A. Somorjai, and A. P. Alivisatos, "Formation of hollow nanocrystals through the nanoscale Kirkendall Effect," (in English), *Science,* vol. 304, no. 5671, pp. 711-714, Apr 30 2004.

[31] A. A. El Mel *et al.*, "Kirkendall Effect vs Corrosion of Silver Nanocrystals by Atomic Oxygen: From Solid Metal Silver to Nanoporous Silver Oxide," (in English), *J Phys Chem C,* vol. 121, no. 35, pp. 19497-19504, Sep 7 2017.

[32] K. Chiba and K. Nakatani, "Photoenhance migration of silver atoms in transparent heat mirror coatings," *Thin Solid Films,* vol. 112, pp. 359-367, 1984.

[33] A. H. Pfund, "Transparent Screen," Patent Appl. US1176313A, 1916.

[34] R. E. Hummel, "Electronic Properties of Materials," 4 ed., 2011, p. 225.

[35] R. E. Hummel, "Electronic Properties of Materials," 4 ed., 2011, p. 228.

[36] L. Liu *et al.*, "Achieving low-emissivity materials with high transmission for broadband radio-frequency signals," *Sci Rep,* vol. 7, no. 1, p. 4840, Jul 7 2017.

[37] Z. Chen, L. Zhu, A. Raman, and S. Fan, "Radiative cooling to deep sub-freezing temperatures through a 24-h day–night cycle," *Nature communications,* vol. 7, p. 13729, 2016.

[38] K. S. Lion, "Heat-reflecting light-transmitting window shade or the like and material for use in manufacturing the same," Patent Appl. US2774421A, 1937.

[39] L. Holland and G. Siddall, "Heat-reflecting windows using gold and bismuth oxide films," *Journal of Applied Physics,* vol. 9, pp. 359-361, 1958.

[40] J. Rissman and H. Kennan, "Low-Emissivity Windows," A. E. I. Council, Ed., ed, 2013.

[41] H. J. Glaser, "History of the development and industrial production of low thermal emissivity coatings for high heat insulating glass units," *Appl Opt,* vol. 47, no. 13, pp. C193-9, May 1 2008.

[42] P. Grosse, R. Hertling, and T. Muggenburg, "Design of low emissivity systems based on a three-layer coating," (in English), *Journal of Non-Crystalline Solids,* vol. 218, pp. 38-43, Sep 1997.

[43] B. P. Jelle, "Solar radiation glazing factors for window panes, glass structures and electrochromic windows in buildings—Measurement and calculation," *Solar Energy Materials & Solar Cells,* vol. 116, pp. 291-323, 2013.

[44] B. P. Jelle, "Solar radiation glazing factors for window panes, glass structures and electrochromic windows in buildings-Measurement and calculation," (in English), *Solar Energy Materials and Solar Cells,* vol. 116, pp. 291-323, Sep 2013.

[45] B. P. Jelle, S. E. Kalnaes, and T. Gao, "Low-emissivity materials for building applications: A state-of-the-art review and future research perspectives," (in English), *Energy and Buildings,* vol. 96, pp. 329-356, Jun 1 2015.

[46] M. Rubin, "Optical properties of soda lime silica glasses," *Solar Energy Materials,* vol. 12, no. 4, pp. 275-288, 1985.

[47]   J. H. Henninger, "Solar Absorptance and Thermal Emittance of Some Common Spacecraft Thermal Control Coatings," in "NASA Reference Publication " NASA, 1984.

[48]   D. L. Marinoski, S. Guths, and R. Lamberts, "Development of a calorimeter for determination of the solar factor of architectural glass and fenestrations," (in English), *Building and Environment,* vol. 47s, pp. 232-242, Jan 2012.

[49]   J. H. Klems and G. O. Kelley, "Calorimetric Measurements of Inward-Flowing Fraction for Complex Glazing and Shading Systems," presented at the ASHRAE Winter Meeting, Atlanta, GA, 1996.

[50]   T. T. Chow, C. Y. Li, and Z. Lin, "Innovative solar windows for cooling-demand climate," (in English), *Solar Energy Materials and Solar Cells,* vol. 94, no. 2, pp. 212-220, Feb 2010.

[51]   M. Zinzi, "Office worker preferences of electrochromic windows: a pilot study," (in English), *Building and Environment,* vol. 41, no. 9, pp. 1262-1273, Sep 2006.

[52]   C. G. Granqvist, M. A. Arvizu, I. B. Pehlivan, H.-Y. Q. a, R.-T. Wen, and G. A. Niklasson, "Electrochromic materials and devices for energy efficiency and humancomfort in buildings: A critical review," *Electrochimica Acta,* vol. 259, pp. 1170-1182, 2018.

[53]   C. E. Ochoa, M. B. C. Aries, E. J. van Loenen, and J. L. M. Hensen, "Considerations on design optimization criteria for windows providing low energy consumption and high visual comfort," (in English), *Applied Energy,* vol. 95, pp. 238-245, Jul 2012.

[54]   Y. Hua, A. Oswald, and X. D. Yang, "Effectiveness of daylighting design and occupant visual satisfaction in a LEED Gold laboratory building," (in English), *Building and Environment,* vol. 46, no. 1, pp. 54-64, Jan 2011.

[55]   A. Cannavale, F. Martellotta, P. Cossari, G. Gigli, and U. Ayr, "Energy savings due to building integration of innovative solid-state electrochromic devices," (in English), *Applied Energy,* vol. 225, pp. 975-985, Sep 1 2018.

[56]   M. Casini, "Active dynamic windows for buildings: A review," (in English), *Renewable Energy,* vol. 119, pp. 923-934, Apr 2018.

[57]   C. G. Granqvist, "Electrochromics for smart windows: Oxide-based thin films and devices," (in English), *Thin Solid Films,* vol. 564, pp. 1-38, Aug 1 2014.

[58]   N. DeForest, A. Shehabi, S. Selkowitz, and D. J. Milliron, "A comparative energy analysis of three electrochromic glazing technologies in commercial and residential buildings," (in English), *Applied Energy,* vol. 192, pp. 95-109, Apr 15 2017.

[59]   Y. Ajaji and P. Andre, "Thermal comfort and visual comfort in an office building equipped with smart electrochromic glazing: an experimental study," (in English), *6th International Building Physics Conference (Ibpc 2015),* vol. 78, pp. 2464-2469, 2015.

[60]   E. L. Runnerstrom, A. Llordes, S. D. Lounis, and D. J. Milliron, "Nanostructured electrochromic smart windows: traditional materials and NIR-selective plasmonic nanocrystals," *Chem Commun (Camb),* vol. 50, no. 73, pp. 10555-72, Sep 21 2014.

[61]   C. G. Granqvist, M. A. Arvizu, H.-Y. Qu, R.-T. Wen, and G. A. Niklasson, "Advances in electrochromic device technology: Multiple roads towards superior durability," *Surface & Coatings Technology,* vol. 357, pp. 619-625, 2019.

[62]   C. G. Granqvist, "Oxide electrochromics: An introduction to devices and materials," (in English), *Solar Energy Materials and Solar Cells,* vol. 99, pp. 1-13, Apr 2012.

[63]   R. T. Wen, C. G. Granqvist, and G. A. Niklasson, "Eliminating degradation and uncovering ion-trapping dynamics in electrochromic WO3 thin films," *Nat Mater,* vol. 14, no. 10, pp. 996-1001, Oct 2015.

[64]   B. Baloukas *et al.*, "Galvanostatic Rejuvenation of Electrochromic WO3 Thin Films: Ion Trapping and Detrapping Observed by Optical Measurements and by Time-of-Flight Secondary Ion Mass Spectrometry," *ACS Appl Mater Interfaces,* vol. 9, no. 20, pp. 16995-17001, May 24 2017.

[65]   C. G. Granqvist, İ. B. Pehlivan, and G. A. Niklasson, "Electrochromics on a roll: Web-coating and lamination forsmart windows," *Surface & Coatings Technology,* vol. 336, pp. 133-138, 2018.

[66]   F. Blanchard, B. Baloukas, and L. Martinu, "Highly durable electrochromic tungsten oxide thin films prepared by high rate bias-enhanced sputter deposition," (in English), *Applied Materials Today,* vol. 12, pp. 235-243, Sep 2018.

[67]   B. A. Samad and P. V. Ashrit, "Optimization of mixed conductivity through nanostructure control in WO3 thin films," (in English), *Thin Solid Films,* vol. 636, pp. 717-722, Aug 31 2017.

[68]   J. W. Lee, H. J. Jung, J. Y. Park, J. B. Lee, and Y. Yoon, "Optimization of building window system in Asian regions by analyzing solar heat gain and daylighting elements," (in English), *Renewable Energy,* vol. 50, pp. 522-531, Feb 2013.

[69]   G. Garcia *et al.*, "Dynamically modulating the surface plasmon resonance of doped semiconductor nanocrystals," *Nano Lett,* vol. 11, no. 10, pp. 4415-20, Oct 12 2011.

[70]   A. Llordes, G. Garcia, J. Gazquez, and D. J. Milliron, "Tunable near-infrared and visible-light transmittance in nanocrystal-in-glass composites," *Nature,* vol. 500, no. 7462, pp. 323-6, Aug 15 2013.

[71]   A. Llordes *et al.*, "Linear topology in amorphous metal oxide electrochromic networks obtained via low-temperature solution processing," (in English), *Nature Materials,* vol. 15, no. 12, pp. 1267-1273, Dec 2016.

[72]   S. L. Zhang, S. Cao, T. R. Zhang, A. Fisher, and J. Y. Lee, "Al3+ intercalation/de-intercalation-enabled dual-band electrochromic smart windows with a high optical modulation, quick response and long cycle life," (in English), *Energy & Environmental Science,* vol. 11, no. 10, pp. 2884-2892, Oct 1 2018.

[73]   S. L. Zhang, S. Cao, T. R. Zhang, Q. F. Yao, A. Fisher, and J. Y. Lee, "Monoclinic oxygen-deficient tungsten oxide nanowires for dynamic and independent control of near-infrared and visible light transmittance," (in English), *Materials Horizons,* vol. 5, no. 2, pp. 291-297, Mar 2018.

[74]   M. Barawi *et al.*, "A dual band electrochromic device switchable across four distinct optical modes," (in English), *Journal of Materials Chemistry A,* vol. 6, no. 22, pp. 10201-10205, Jun 14 2018.

[75] P. Jin, S. Nakao, and S. Tanemura, "Tungsten doping into vanadium dioxide thermochromic films by high-energy ion implantation and thermal annealing," (in English), *Thin Solid Films,* vol. 324, no. 1-2, pp. 151-158, Jul 1 1998.

[76] J. Q. Shi, S. X. Zhou, B. You, and L. M. Wu, "Preparation and thermochromic property of tungsten-doped vanadium dioxide particles," (in English), *Solar Energy Materials and Solar Cells,* vol. 91, no. 19, pp. 1856-1862, Nov 23 2007.

[77] C. Piccirillo, R. Binions, and I. P. Parkin, "Synthesis and characterisation of W-doped VO2 by Aerosol Assisted Chemical Vapour Deposition," *Thin Solid Films,* vol. 516, pp. 1992-1997, 2008.

[78] M. Jiang *et al.*, "Improved luminous transmittance and diminished yellow color in VO2 energy efficient smart thin films by Zn doping," (in English), *Ceramics International,* vol. 40, no. 4, pp. 6331-6334, May 2014.

[79] C. H. Ji *et al.*, "Al-doped VO2 films as smart window coatings: Reduced phase transition temperature and improved thermochromic performance," (in English), *Solar Energy Materials and Solar Cells,* vol. 176, pp. 174-180, Mar 2018.

[80] S. Y. Li *et al.*, "Bandgap widening in thermochromic Mg-doped VO2 thin films: Quantitative data based on optical absorption," (in English), *Applied Physics Letters,* vol. 103, no. 16, Oct 14 2013.

[81] S. Y. Li, G. A. Niklasson, and C. G. Granqvist, "Thermochromic fenestration with VO2-based materials: Three challenges and how they can be met," (in English), *Thin Solid Films,* vol. 520, no. 10, pp. 3823-3828, Mar 1 2012.

[82] S. Y. Li, G. A. Niklasson, and C. G. Granqvist, "Thermochromic undoped and Mg-doped VO2 thin films and nanoparticles: Optical properties and performance limits for energy efficient windows," (in English), *Journal of Applied Physics,* vol. 115, no. 5, Feb 7 2014.

[83] N. R. Mlyuka, G. A. Niklasson, and C. G. Granqvist, "Mg doping of thermochromic VO2 films enhances the optical transmittance and decreases the metal-insulator transition temperature," (in English), *Applied Physics Letters,* vol. 95, no. 17, Oct 26 2009.

[84] S. Y. Li, G. A. Niklasson, and C. G. Granqvist, "Nanothermochromics with VO2-based core-shell structures: Calculated luminous and solar optical properties," (in English), *Journal of Applied Physics,* vol. 109, no. 11, Jun 1 2011.

[85] Y. Gao *et al.*, "Enhanced chemical stability of VO2 nanoparticles by the formation of SiO2/VO2 core/shell structures and the application to transparent and flexible VO2-based composite foils with excellent thermochromic properties for solar heat control," *Energy & Environmental Science,* vol. 5, p. 6104, 2012.

[86] Y. M. Li, S. D. Ji, Y. F. Gao, H. J. Luo, and M. Kanehira, "Core-shell VO2@TiO2 nanorods that combine thermochromic and photocatalytic properties for application as energy-saving smart coatings," (in English), *Scientific Reports,* vol. 3, Apr 2 2013.

[87] "Mg-doped VO2 nanoparticles: hydrothermal synthesis, enhanced visible transmittance and decreased metal–insulator transition temperature," *Physical Chemistry Chemical Physics,* vol. 15, no. 20, p. 7505, 2013.

[88]   Q. Hao *et al.*, "VO2 /TiN Plasmonic Thermochromic Smart Coatings for Room-Temperature Applications," *Adv Mater,* vol. 30, no. 10, Mar 2018.

[89]   B. Baloukas, S. Loquai, and L. Martinu, "VO2-based thermally active low emissivity coatings," (in English), *Solar Energy Materials and Solar Cells,* vol. 183, pp. 25-33, Aug 15 2018.

[90]   D. C. Lim *et al.*, "Semi-transparent plastic solar cell based on oxide-metal-oxide multilayer electrodes," *Progress in Photovoltaics Research and Applications,* vol. 26, no. 3, pp. 188-195, 2018.

[91]   J. C. Goldschmidt, "From window to solar cell and back," *Nat Mater,* vol. 17, no. 3, pp. 218-219, Mar 2018.

[92]   C. Schaefer, G. Bräuer, and J. Szczyrbowski, "Low emissivity coatings on architectural glass," *Surface and Coatings Technology,* vol. 93, no. 1, pp. 37-45, 1997.

[93]   M. Ohring, *Materials Science of Thin Films*. Academic Press, 2001.

[94]   J. L. Vossen and W. Kern, *Thin Film Processes II*. Academic Press, 1991.

[95]   P. M. Martin, *Handbook of Deposition Technologies for Films and Coatings*, 3 ed. William Andrew Publishing, 2010.

[96]   S. S. Todorov and E. R. Fossum, "Oxidation of silicon by a low-energy ion beam : Experiment and model," *Applied Physics Letters,* vol. 52, no. 1, pp. 48-50, 1988.

[97]   H. S. Butler and G. S. Kino, "Plasma Sheath Formation by Radio-Frequency Fields," *The Physics of Fluids,* vol. 6, p. 1346, 1963.

[98]   P. J. Kelly and R. D. Arnell, "Magnetron sputtering: a review of recent developments and applications," (in English), *Vacuum,* vol. 56, no. 3, pp. 159-172, Mar 2000.

[99]   G. Beister *et al.*, "Advanced Layer Systems and Coating Techniques for Large-Area Glass Coatings by Means of High-Rate Sputtering," (in English), *Glastechnische Berichte-Glass Science and Technology,* vol. 66, no. 6-7, pp. 175-183, Jun-Jul 1993.

[100]   M. A. Surmeneva *et al.*, "Incorporation of silver nanoparticles into magnetron-sputtered calcium phosphate layers on titanium as an antibacterial coating," (in English), *Colloids and Surfaces B-Biointerfaces,* vol. 156, pp. 104-113, Aug 1 2017.

[101]   M. Staszek, J. Siegel, M. Polivkova, and V. Svorcik, "Influence of temperature on silver nanoparticle size prepared by sputtering into PVP-glycerol system," (in English), *Materials Letters,* vol. 186, pp. 341-344, Jan 1 2017.

[102]   K. Zawadzka *et al.*, "Mechanisms of antibacterial activity and stability of silver nanoparticles grow n o n magnetron sputtered TiO2coatings," *Bulletin of Materials Science,* vol. 39, no. 1, pp. 57-68, 2016.

[103]   R. S. Sreedharan, V. S. Kavitha, S. Suresh, R. R. Krishnan, R. J. Bose, and V. P. M. Pillai, "Tailoring the properties of zinc oxide films by incorporating gold nanoparticles using RF magnetron sputtering," (in English), *Applied Physics a-Materials Science & Processing,* vol. 124, no. 12, Dec 2018.

[104]   A. Achour, M. Islam, S. Solaymani, S. Vizireanu, K. Saeed, and G. Dinescu, "Influence of plasma functionalization treatment and gold nanoparticles on surface chemistry and

wettability of reactive-sputtered TiO2 thin films," (in English), *Applied Surface Science,* vol. 458, pp. 678-685, Nov 15 2018.

[105] L. Y. Jiang, H. X. Li, J. X. Mu, and Z. G. Ji, "Manipulation of surface plasmon resonance of sputtered gold-nanoparticles on TiO2 nanostructured films for enhanced photoelectrochemical water splitting efficiency," (in English), *Thin Solid Films,* vol. 661, pp. 32-39, Sep 1 2018.

[106] V. Sharma, H. Sharma, R. Vyas, and K. Sachdev, "Polymer-metal-polymer (PMP) multilayer transparent electrode for organic optoelectronics," (in English), *Materials & Design,* vol. 156, pp. 135-142, Oct 15 2018.

[107] J. Linnet, A. R. Walther, C. Wolff, O. Albrektsen, N. A. Mortensen, and J. Kjelstrup-Hansen, "Transparent and conductive electrodes by large-scale nano-structuring of noble metal thin-films," (in English), *Optical Materials Express,* vol. 8, no. 7, pp. 1733-1746, Jul 1 2018.

[108] D. C. Lim *et al.*, "Semi-transparent plastic solar cell based on oxide-metal-oxide multilayer electrodes," (in English), *Progress in Photovoltaics,* vol. 26, no. 3, pp. 188-195, Mar 2018.

[109] F. M. Wisser, K. Eckhardt, W. Nickel, W. Bohlmann, S. Kaskel, and J. Grothe, "Highly transparent metal electrodes via direct printing processes," (in English), *Materials Research Bulletin,* vol. 98, pp. 231-234, Feb 2018.

[110] P. Andreazza, C. Andreazza-Vignolle, J. P. Rozenbaum, A. L. Thomann, and P. Brault, "Nucleation and initial growth of platinum islands by plasma sputter deposition," (in English), *Surface & Coatings Technology,* vol. 151, pp. 122-127, Mar 1 2002.

[111] C. T. Campbell, "Ultrathin metal films and particles on oxide surfaces: structural, electronic and chemisorptive properties," *Surface Science Reports,* vol. 27, no. 1-3, pp. 1-111, 1997.

[112] M. J. S. D. W. Pashley, M. H. Jacobs, and T. J. Law, "The growth and structure of gold and silver deposits formed by evaporation inside an electron microscope," *Philosophical Magazine,* vol. 10, pp. 127-158, 1964.

[113] A. G. Elliot, "Nucleation kinetics for gold deposited onto mica substrates," *Surface Science,* vol. 44, pp. 337-359, 1974.

[114] A. C. G. Desrousseaux, and Z. Jiang, "Variation du coefficient de collage de l'argent et de l'or durant leur condensation sur film de MgO," *Journal de Physique II,* vol. 3, pp. 1461-1477, 1993.

[115] C. G. Granqvist, "Ultrafine metal particles," *Journal of Applied Physics,* vol. 47, p. 2200, 1976.

[116] C. G. Granqvist and R. A. Buhrman, "Statistical model for coalescence of islands in discontinuous films," *Applied Physics Letters,* vol. 27, p. 693, 1975.

[117] P. T. Stroud, "Nucleation and critical condensation phenomena of silver on silicon oxide," *Journal of Physics C: Solid State Physics,* vol. 4, pp. 577-583, 1971.

[118] C. Templier, S. Muzard, A. Galdikas, L. Pranevicius, J. Delafond, and J. C. Desoyer, "A phenomenological study of the initial stages of film growth," (in English), *Surface & Coatings Technology,* vol. 125, no. 1-3, pp. 129-133, Mar 2000.

[119]   B. Lewis and J. C. Anderson, *Nucleation and Growth of Thin Films*. Academic Press Inc., 1979, p. 516.

[120]   G. Desrousseaux, A. Carlan, and Z. Jiang, "Variation du coefficient de collage de l'argent et de l'or durant leur condensation sur film de MgO," *Journal de Physique II,* vol. 3, no. 10, pp. 1461-1477, 1993.

[121]   L.-H. Chen, C.-Y. Chen, and Y.-L. Lee, "Nucleation and growth of clusters in the process of vapor deposition," *Surface Science,* vol. 429, no. 1-3, pp. 150-160, 1999.

[122]   G. Antczak and G. Ehrlich, "Jump processes in surface diffusion," *Surface Science Reports,* vol. 62, no. 2, pp. 39-61, 2007.

[123]   E. Seebauer, "Estimating surface diffusion coefficients," *Progress in Surface Science,* vol. 49, no. 3, pp. 265-330, 1995.

[124]   V. Halpern, "Cluster Growth and Saturation Island Densities in Thin-Film Growth," *Journal of Applied Physics,* vol. 40, no. 11, p. 4627, 1969.

[125]   J. G. Amar, M. N. Popescu, and F. Family, "Rate-Equation Approach to Island Capture Zones and Size Distributions in Epitaxial Growth," *Physical Review Letters,* vol. 86, no. 14, pp. 3092-3095, 2001.

[126]   W. J. C. Orr, "Calculations of the adsorption behaviour of argon on alkali halide crystals," *Transactions of the Faraday Society,* vol. 35, p. 1247, 1939.

[127]   P. Jensen, H. Larralde, M. Meunier, and A. Pimpinelli, "Growth of three-dimensional structures by atomic deposition on surfaces containing defects: simulations and theory," *Surface Science,* vol. 412-413, pp. 458-476, 1998.

[128]   A. Imre, D. L. Beke, E. Gontier-Moya, I. A. Szabo, and E. Gillet, "Surface Ostwald ripening of Pd nanoparticles on the MgO (100) surface," (in English), *Appl Phys a-Mater,* vol. 71, no. 1, pp. 19-22, Jul 2000.

[129]   M. Zinke-Allmang, L. C. Feldman, and S. Nakahara, "Role of Ostwald ripening in islanding processes," *Applied Physics Letters,* vol. 51, no. 13, p. 975, 1987.

[130]   N. C. Bartelt, W. Theis, and R. M. Tromp, "Ostwald ripening of two-dimensional islands on Si(001)," *Physical Review B,* vol. 54, no. 16, pp. 11741-11751, 1996.

[131]   P. T. Stroud, "Nucleation and critical condensation phenomena of silver on silicon oxide," *Journal of Physics C: Solid State Physics,* vol. 4, no. 5, pp. 577-583, 1971.

[132]   B. Lewis, "Nucleation and Initial-Growth Behavior of Thin-Film Deposits," *Journal of Vacuum Science and Technology,* vol. 4, no. 5, p. 209, 1967.

[133]   S. Ozawa and S. Fujiwara, "Nucleus shape and growth rate of bismuth films vacuum-deposited onto amorphous silicon monoxide and carbon substrates," *Thin Solid Films,* vol. 37, no. 1, pp. 73-83, 1976.

[134]   C. Templier, S. Muzard, A. Galdikas, L. Pranevicius, J. Delafond, and J. C. Desoyer, "A phenomenological study of the initial stages of film growth," *Surface and Coatings Technology,* vol. 125, no. 1-3, pp. 129-133, 2000.

[135] C. Furgeaud, L. Simonot, A. Michel, C. Mastail, and G. Abadias, "Impact of Ge alloying on the early growth stages, microstructure and stress evolution of sputter-deposited Cu-Ge thin films," (in English), *Acta Materialia,* vol. 159, pp. 286-295, Oct 15 2018.

[136] F. Cemin *et al.*, "Benefits of energetic ion bombardment for tailoring stress and microstructural evolution during growth of Cu thin films," (in English), *Acta Materialia,* vol. 141, pp. 120-130, Dec 2017.

[137] P. B. Barna and M. Adamik, "Fundamental structure forming phenomena of polycrystalline films and the structure zone models," (in English), *Thin Solid Films,* vol. 317, no. 1-2, pp. 27-33, Apr 1 1998.

[138] B. Lewis and G. J. Rees, "Adatom migration, capture and decay among competing nuclei on a substrate," *Philosophical Magazine,* vol. 29, no. 6, pp. 1253-1280, 1974.

[139] J. P. Hirth, "Some comments on heterogeneous nucleation from the vapor phase," *Journal of Crystal Growth,* vol. 17, pp. 63-69, 1972.

[140] M. Copel, M. C. Reuter, E. Kaxiras, and R. M. Tromp, "Surfactants in epitaxial growth," *Phys Rev Lett,* vol. 63, no. 6, pp. 632-635, Aug 7 1989.

[141] E. Mirica, G. Kowach, and H. Du, "Modified Structure Zone Model to Describe the Morphological Evolution of ZnO Thin Films Deposited by Reactive Sputtering," *Crystal Growth & Design,* vol. 4, no. 1, pp. 157-159, 2004.

[142] D. P. Singh, P. Goel, and J. P. Singh, "Revisiting the structure zone model for sculptured silver thin films deposited at low substrate temperatures," *Journal of Applied Physics,* vol. 112, no. 10, p. 104324, 2012.

[143] M. R. Jacobson and J. A. Thornton, "Structure-Zone Models Of Thin Films," vol. 0821, pp. 95-105, 1988.

[144] M. Fox, *Optical Properties of Solids*, 2nd ed. Oxford University Press, 2010, p. 408.

[145] M. A. Ordal *et al.*, "Optical properties of the metals Al, Co, Cu, Au, Fe, Pb, Ni, Pd, Pt, Ag, Ti, and W in the infrared and far infrared," *Appl Opt,* vol. 22, no. 7, pp. 1099-20, Apr 1 1983.

[146] D. Barchiesi and T. Grosges, "Fitting the optical constants of gold, silver, chromium, titanium, and aluminum in the visible bandwidth," (in English), *Journal of Nanophotonics,* vol. 8, Jan 6 2014.

[147] G. B. Smith and C.-G. S. Granqvist, *Green Nanotechnology: Solutions for Sustainability and Energy in the Built Environment*. CRC Press 2010, p. 472.

[148] S. A. Maier, *Plasmonics: Fundamentals and Applications*. Springer US, 2007, p. 224.

[149] M. Philipp, "Electrical Transport and Scattering Mechanisms in Thin Silver Films for Thermally Insulating Glazing," Ph.D. Thesis, Faculty of Mathematics and Natural Sciences, Dresden University of Technology, 2011.

[150] K. Vedam, "Spectroscopic ellipsometry: a historical overview," (in English), *Thin Solid Films,* vol. 313, pp. 1-9, Feb 1998.

[151] H. Fujiwara, *Spectroscopic Ellipsometry: Principles and Applications*. Wiley, 2007.

[152] P. V. d. Heide, *X-ray Photoelectron Spectroscopy: An introduction to Principles and Practices*. Wiley, 2011.

[153] V. I. Trofimov, N. M. Sushkova, and J. I. Kim, "X-ray photoelectron spectroscopy study of the initial growth of transition metal nanoscale films on (100) Si substrates," (in English), *Thin Solid Films,* vol. 515, no. 16, pp. 6586-6589, Jun 4 2007.

[154] J. A. Jimenez, H. Liu, and E. Fachini, "X-ray photoelectron spectroscopy of silver nanoparticles in phosphate glass," (in English), *Materials Letters,* vol. 64, no. 19, pp. 2046-2048, Oct 15 2010.

[155] Y. Q. Xiong, L. M. Liu, W. G. Lu, D. Q. Yang, and D. A. Da, "Atomic force microscopy and X-ray photoelectron spectroscopy study on nanostructured silver thin films irradiated by atomic oxygen," (in English), *Materials Science and Engineering B-Solid State Materials for Advanced Technology,* vol. 79, no. 1, pp. 68-70, Jan 4 2001.

[156] S. Olthof, J. Meiss, B. Lussem, M. K. Riede, and K. Leo, "Photoelectron spectroscopy investigation of thin metal films employed as top contacts in transparent organic solar cells," (in English), *Thin Solid Films,* vol. 519, no. 6, pp. 1872-1875, Jan 3 2011.

[157] IONTOF. *TOf.SIMS Superior Performance for all SIMS Applications* [Online]. Available: https://www.iontof.com/download/IONTOF_TOF-SIMS_5_Brochure.pdf.

[158] S. Muramoto, J. Brison, and D. G. Castner, "Exploring the Surface Sensitivity of ToF-SIMS by Measuring the Implantation and Sampling Depths of Bin and C60 Ions in Organic Films," *Analytical Chemistry,* vol. 84, no. 1, pp. 365–372, 2012.

[159] A. Zandiatashbar *et al.*, "High-throughput automatic defect review for 300mm blank wafers with atomic force microscope," (in English), *Metrology, Inspection, and Process Control for Microlithography Xxix,* vol. 9424, 2015.

[160] K. L. Sorokina and A. L. Tolstikhina, "Atomic force microscopy modified for studying electric properties of thin films and crystals. Review," (in English), *Crystallography Reports,* vol. 49, no. 3, pp. 476-499, May-Jun 2004.

[161] B. Instruments, "Atomic Force Microscopy (Bruker MultiMode Nanoscope IIIA)," in *Standard Operating Procedure*, Bruker, Ed., ed, 2016.

[162] N. Kalfagiannis *et al.*, "Plasmonic silver nanoparticles for improved organic solar cells," (in English), *Solar Energy Materials and Solar Cells,* vol. 104, pp. 165-174, Sep 2012.

[163] N. Venugopal and A. Mitra, "Optical transparency of ZnO thin film using localized surface plasmons of Ag nanoislands," (in English), *Optical Materials,* vol. 35, no. 7, pp. 1467-1476, May 2013.

[164] H. Monard and F. Sabary, "Optical properties of silver, gold and aluminum ultra-thin granular films evaporated on oxidized aluminum," (in English), *Thin Solid Films,* vol. 310, no. 1-2, pp. 265-273, Nov 21 1997.

[165] S. A. Maier and H. A. Atwater, "Plasmonics: Localization and guiding of electromagnetic energy in metal/dielectric structures," (in English), *Journal of Applied Physics,* vol. 98, no. 1, Jul 1 2005.

[166] B. Lamprecht *et al.*, "Metal nanoparticle gratings: influence of dipolar particle interaction on the plasmon resonance," *Phys Rev Lett,* vol. 84, no. 20, pp. 4721-4, May 15 2000.

[167] V. V. Truong and G. D. Scott, "Optical properties of aggregated noble metal films," *J. Opt. Soc. Am.,* no. 67, pp. 502–510, 1977.

[168] G. Bader, P. V. Ashrit, F. E. Girouard, and V. V. Truong, "P-Polarized Optical-Properties of Aggregated Au Films," (in English), *Journal of Applied Physics,* vol. 68, no. 4, pp. 1820-1824, Aug 15 1990.

[169] H. Y. Wei and H. Eilers, "From silver nanoparticles to thin films: Evolution of microstructure and electrical conduction on glass substrates," (in English), *Journal of Physics and Chemistry of Solids,* vol. 70, no. 2, pp. 459-465, Feb 2009.

[170] A. I. Maaroof and D. S. Sutherland, "Optimum plasmon hybridization at percolation threshold of silver films near metallic surfaces," (in English), *J Phys D Appl Phys,* vol. 43, no. 40, Oct 13 2010.

[171] T. W. H. Oates, D. R. McKenzie, and M. M. M. Bilek, "Percolation threshold in ultrathin titanium films determined by in situ spectroscopic ellipsometry," (in English), *Physical Review B,* vol. 70, no. 19, Nov 2004.

[172] J. Bulir, M. Novotny, A. Lynnykova, and J. Lancok, "Preparation of nanostructured ultrathin silver layer," (in English), *Journal of Nanophotonics,* vol. 5, p. 051511, Mar 17 2011.

[173] A. J. de Vries, E. S. Kooij, H. Wormeester, A. A. Mewe, and B. Poelsema, "Ellipsometric study of percolation in electroless deposited silver films," (in English), *Journal of Applied Physics,* vol. 101, no. 5, Mar 1 2007.

[174] T. W. H. Oates and A. Mucklich, "Evolution of plasmon resonances during plasma deposition of silver nanoparticles," (in English), *Nanotechnology,* vol. 16, no. 11, pp. 2606-2611, Nov 2005.

[175] M. N. Bulir, J. Lancok, L. Fekete, J. Drahokoupil, and J. Musil, "Nucleation of ultrathin silver layer by magnetron sputtering in Ar/N2 plasma," *Surf. Coat. Technol.,* vol. 228, pp. S86–S90, 2013.

[176] S. Grachev, M. de Grazia, E. Barthel, E. Sondergard, and R. Lazzari, "Real-time monitoring of nanoparticle film growth at high deposition rate with optical spectroscopy of plasmon resonances," (in English), *J Phys D Appl Phys,* vol. 46, no. 37, Sep 18 2013.

[177] V. S. Grinevich *et al.*, "Surface plasmon resonance investigation procedure as a structure sensitive method for SnO2 nanofilms," (in English), *Thin Solid Films,* vol. 522, pp. 452-456, Nov 1 2012.

[178] D. A. Grynko *et al.*, "Modulation polarimetry of the topological effect in gold-organic nanocomposite films," (in English), *Physics of the Solid State,* vol. 54, no. 11, pp. 2301-2308, Nov 2012.

[179] J. C. Joud, M. Houmard, and G. Berthome, "Surface charges of oxides and wettability: Application to TiO2-SiO2 composite films," (in English), *Applied Surface Science,* vol. 287, pp. 37-45, Dec 15 2013.

[180] T. T. U. Le, A. Sasahara, and M. Tomitori, "Water Wettability of an Ultrathin Layer of Silicon Oxide Epitaxially Grown on a Rutile Titanium Dioxide (110) Surface," (in English), *J Phys Chem C,* vol. 117, no. 45, pp. 23621-23625, Nov 14 2013.

[181] J. Han and W. Gao, "Surface Wettability of Nanostructured Zinc Oxide Films," (in English), *Journal of Electronic Materials,* vol. 38, no. 4, pp. 601-608, Apr 2009.

[182] D. Aronov and G. Rosenman, "Surface energy modification by electron beam," (in English), *Surface Science,* vol. 601, no. 21, pp. 5042-5049, Nov 1 2007.

[183] F. Goutaland, E. Marin, J. Y. Michalon, and A. Boukenter, "Growth of silver nanoparticles of variable and controlled diameter in silica-based and soda-lime glasses by simultaneous continuous ultraviolet irradiation and heat treatment," (in English), *Applied Physics Letters,* vol. 94, no. 18, May 4 2009.

[184] J. Bico, U. Thiele, and D. Quere, "Wetting of textured surfaces," (in English), *Colloids and Surfaces a-Physicochemical and Engineering Aspects,* vol. 206, no. 1-3, pp. 41-46, Jul 9 2002.

[185] T. Uelzen and J. Muller, "Wettability enhancement by rough surfaces generated by thin film technology," (in English), *Thin Solid Films,* vol. 434, no. 1-2, pp. 311-315, Jun 23 2003.

[186] D. S. Ghosh *et al.*, "Highly Flexible Transparent Electrodes Containing Ultrathin Silver for Efficient Polymer Solar Cells," (in English), *Advanced Functional Materials,* vol. 25, no. 47, pp. 7309-7316, Dec 16 2015.

[187] S. H. Liu *et al.*, "Silver/germanium/silver: an effective transparent electrode for flexible organic light-emitting devices," (in English), *Journal of Materials Chemistry C,* vol. 2, no. 5, pp. 835-840, 2014.

[188] E.Valkonen, B.Karlsson, and C-G.Ribbing, "Solar optical properties of thin films of Cu, Ag, Au, Cr, Fe, Co, Ni and Al," *Solar Energy,* vol. 32, no. 2, pp. 211-222, 1984.

[189] C. G. Granqvist and R. A. Buhrman, "Statistical model for coalescence of islands in discontinuous films," *Appl. Phys. Lett.,* vol. 27, p. 693, 1975.

[190] V. Halpern, "Cluster Growth and Saturation Island Densities in Thin-Film Growth," *Journal of Applied Physics,* vol. 40, p. 4627, 1969.

[191] F. Otieno, M. Airo, K. Ranganathan, and D. Wamwangi, "Annealed silver-islands for enhanced optical absorption in organic solar cell," (in English), *Thin Solid Films,* vol. 598, pp. 177-183, Jan 1 2016.

[192] S. Mubeen, G. Hernandez-Sosa, D. Moses, J. Lee, and M. Moskovits, "Plasmonic photosensitization of a wide band gap semiconductor: converting plasmons to charge carriers," *Nano Lett,* vol. 11, no. 12, pp. 5548-52, Dec 14 2011.

[193] H. Robatjazi, S. M. Bahauddin, C. Doiron, and I. Thomann, "Direct Plasmon-Driven Photoelectrocatalysis," *Nano Lett,* vol. 15, no. 9, pp. 6155-61, Sep 9 2015.

[194] C. Cioarec, P. Melpignano, N. Gherardi, R. Clergereaux, and C. Villeneuve, "Ultrasmooth silver thin film electrodes with high polar liquid wettability for OLED microcavity application," *Langmuir,* vol. 27, no. 7, pp. 3611-7, Apr 5 2011.

[195] C. Schaefer, G. Brauer, and J. Szczyrbowski, "Low emissivity coatings on architectural glass," (in English), *Surface & Coatings Technology,* vol. 93, no. 1, pp. 37-45, Aug 1997.

[196] D. Gu, C. Zhang, Y. K. Wu, and L. J. Guo, "Ultrasmooth and thermally stable silver-based thin films with subnanometer roughness by aluminum doping," *ACS Nano,* vol. 8, no. 10, pp. 10343-51, Oct 28 2014.

[197] L. Vj *et al.*, "Ultrasmooth Silver Thin Films Deposited with a Germanium Nucleation Layer," (in English), *Nano Letters,* vol. 9, no. 1, pp. 178-182, Jan 2009.

[198] L. Ke, S. C. Lai, H. Liu, C. K. Peh, B. Wang, and J. H. Teng, "Ultrasmooth silver thin film on PEDOT:PSS nucleation layer for extended surface plasmon propagation," *ACS Appl Mater Interfaces,* vol. 4, no. 3, pp. 1247-53, Mar 2012.

[199] P. Pallavicini *et al.*, "Self-assembled monolayers of silver nanoparticles firmly grafted on glass surfaces: low Ag+ release for an efficient antibacterial activity," *J Colloid Interface Sci,* vol. 350, no. 1, pp. 110-6, Oct 1 2010.

[200] C. A. Goss, D. H. Charych, and M. Majda, "Application of (3-Mercaptopropyl)Trimethoxysilane as a Molecular Adhesive in the Fabrication of Vapor-Deposited Gold Electrodes on Glass Substrates," (in English), *Analytical Chemistry,* vol. 63, no. 1, pp. 85-88, Jan 1 1991.

[201] A. Kossoy, V. Merk, D. Simakov, K. Leosson, S. Kéna-Cohen, and S. A. Maier, "Optical and Structural Properties of Ultra-thin Gold Films," *Advanced Optical Materials,* vol. 3, no. 1, pp. 71-77, 2015.

[202] S. H. Park, J. H. Im, J. W. Im, B. H. Chun, and J. H. Kim, "Adsorption kinetics of Au and Ag nanoparticles on functionalized glass surfaces," (in English), *Microchemical Journal,* vol. 63, no. 1, pp. 71-91, Sep 1999.

[203] P. Pallavicini, G. Dacarro, M. Galli, and M. Patrini, "Spectroscopic evaluation of surface functionalization efficiency in the preparation of mercaptopropyltrimethoxysilane self-assembled monolayers on glass," *J Colloid Interface Sci,* vol. 332, no. 2, pp. 432-8, Apr 15 2009.

[204] M. Kawamura, T. Fudei, and Y. Abe, "Growth of Ag thin films on glass substrates with a 3-mercaptopropyltrimethoxysilane (MPTMS) interlayer," (in English), *15th International Conference on Thin Films (Ictf-15),* vol. 417, 2013.

[205] T. Sasaki, M. Kawamura, Y. Abe, and K. H. Kim, "Suppression of property changes in Ag thin films by introducing organic monolayers," (in English), *Vacuum,* vol. 121, pp. 317-319, Nov 2015.

[206] J. H. Cho, J. A. Lim, J. T. Han, H. W. Jang, J. L. Lee, and K. Cho, "Control of the electrical and adhesion properties of metal/organic interfaces with self-assembled monolayers," (in English), *Applied Physics Letters,* vol. 86, no. 17, Apr 25 2005.

[207] M. H. Hu, S. Noda, T. Okubo, Y. Yamaguchi, and H. Komiyama, "Structure and morphology of self-assembled 3-mercaptopropyltrimethoxysilane layers on silicon oxide," (in English), *Applied Surface Science,* vol. 181, no. 3-4, pp. 307-316, Sep 21 2001.

[208] D. Wang, Y. Zhang, X. Lu, Z. Ma, C. Xie, and Z. Zheng, "Chemical formation of soft metal electrodes for flexible and wearable electronics," *Chem Soc Rev,* vol. 47, no. 12, pp. 4611-4641, Jun 18 2018.

[209] D. Li, W. Y. Lai, Y. Z. Zhang, and W. Huang, "Printable Transparent Conductive Films for Flexible Electronics," *Adv Mater,* vol. 30, no. 10, p. 1704738, Mar 2018.

[210] G. K. Dalapati *et al.*, "Transparent heat regulating (THR) materials and coatings for energy saving window applications: Impact of materials design, micro-structural, and interface quality on the THR performance," *Progress in Materials Science,* vol. 95, pp. 42-131, 2018.

[211] C. G. Granqvist and G. A. Niklasson, "Solar energy materials for thermal applications: A primer," *Solar Energy Materials and Solar Cells,* vol. 180, pp. 213-226, 2018.

[212] N. Selvakumar and H. C. Barshilia, "Review of physical vapor deposited (PVD) spectrally selective coatings for mid- and high-temperature solar thermal applications," *Solar Energy Materials and Solar Cells,* vol. 98, pp. 1-23, 2012.

[213] H. R. Colenso *et al.*, "Comparison of seed layers for smooth, low loss silver films used in ultraviolet-visible plasmonic imaging devices," *Thin Solid Films,* vol. 656, pp. 68-74, 2018.

[214] A. Anders, E. Byon, D.-H. Kim, K. Fukuda, and S. H. N. Lim, "Smoothing of ultrathin silver films by transition metal seeding," *Solid State Communications,* vol. 140, no. 5, pp. 225-229, 2006.

[215] N. Formica, D. S. Ghosh, A. Carrilero, T. L. Chen, R. E. Simpson, and V. Pruneri, "Ultrastable and atomically smooth ultrathin silver films grown on a copper seed layer," *ACS Appl Mater Interfaces,* vol. 5, no. 8, pp. 3048-53, Apr 24 2013.

[216] S. Hafezian, K. Maloney, J. Lefebvre, L. Martinu, and S. Kéna-Cohen, "Continuous ultrathin silver films deposited on SiO2 and SiNx using a self-assembled monolayer," *Applied Physics Letters,* vol. 109, no. 12, 2016.

[217] B. Pattier, J. F. Bardeau, M. Edely, A. Gibaud, and N. Delorme, "Cheap and robust ultraflat gold surfaces suitable for high-resolution surface modification," *Langmuir,* vol. 24, no. 3, pp. 821-5, Feb 5 2008.

[218] V. Maurice and P. Marcus, "Progress in corrosion science at atomic and nanometric scales," *Progress in Materials Science,* vol. 95, pp. 132-171, 2018.

[219] H. Aboulfadl, I. Gallino, R. Busch, and F. Mücklich, "Atomic scale analysis of phase formation and diffusion kinetics in Ag/Al multilayer thin films," *Journal of Applied Physics,* vol. 120, no. 19, 2016.

[220] Y. Yin, R. M. Rioux, C. K. Erdonmez, S. Hughes, G. A. Somorjai, and A. P. Alivisatos, "Formation of hollow nanocrystals through the nanoscale Kirkendall effect," *Science,* vol. 304, no. 5671, pp. 711-4, Apr 30 2004.

[221] J. G. Railsback, A. C. Johnston-Peck, J. Wang, and J. B. Tracy, "Size-dependent nanoscale kirkendall effect during the oxidation of nickel nanoparticles," *ACS Nano,* vol. 4, no. 4, pp. 1913-20, Apr 27 2010.

[222] L. Gao, C. Pang, D. He, L. Shen, A. Gupta, and N. Bao, "Synthesis of Hierarchical Nanoporous Microstructures via the Kirkendall Effect in Chemical Reduction Process," *Sci Rep,* vol. 5, p. 16061, Nov 10 2015.

[223] A.-A. El Mel *et al.*, "Kirkendall Effect vs Corrosion of Silver Nanocrystals by Atomic Oxygen: From Solid Metal Silver to Nanoporous Silver Oxide," *The Journal of Physical Chemistry C,* vol. 121, no. 35, pp. 19497-19504, 2017.

[224] C. Falcony, M. C. Tamargo, M. A. Aguilar, and L. C. Hernandez-Mainet, "Design and engineering of IZO/Ag/glass solar filters for low-emissivity window performance," *Optical Engineering,* vol. 56, no. 10, p. 1, 2017.

[225] L. Zhou, F. Ding, H. Chen, W. Ding, W. Zhang, and S. Y. Chou*, "Enhancement of Immunoassay's Fluorescence and Detection Sensitivity Using Three-Dimensional Plasmonic Nano-Antenna-Dots Array," *Anal Chem,* vol. 84, no. 10, pp. 4489-4495, 2012.

[226] G. W. Yang, G. Y. Gao, C. Wang, C. L. Xu, and H. L. Li, "Controllable deposition of Ag nanoparticles on carbon nanotubes as a catalyst for hydrazine oxidation," (in English), *Carbon,* vol. 46, no. 5, pp. 747-752, Apr 2008.

[227] Y. F. Wei *et al.*, "Enhanced photoelectrochemical water-splitting effect with a bent ZnO nanorod photoanode decorated with Ag nanoparticles," (in English), *Nanotechnology,* vol. 23, no. 23, Jun 15 2012.

[228] J. R. Cole and N. J. Halas, "Optimized plasmonic nanoparticle distributions for solar spectrum harvesting," (in English), *Applied Physics Letters,* vol. 89, no. 15, Oct 9 2006.

[229] V. A. Fedotov, V. I. Emel'yanov, K. F. MacDonald, and N. I. Zheludev, "Optical properties of closely packed nanoparticle films: spheroids and nanoshells," (in English), *Journal of Optics a-Pure and Applied Optics,* vol. 6, no. 2, pp. 155-160, Feb 2004.

[230] D. Fischer, "Influence of substrate temperature and silver-doping on the structural and optical properties of TiO2 films," (in English), *Thin Solid Films,* vol. 598, pp. 204-213, Jan 1 2016.

[231] T. W. H. Oates, A. Keller, S. Facsko, and A. Mucklich, "Aligned silver nanoparticles on rippled silicon templates exhibiting anisotropic plasmon absorption," (in English), *Plasmonics,* vol. 2, no. 2, pp. 47-50, Jun 2007.

[232] T. Wenzel, J. Bosbach, F. Stietz, and F. Trager, "In situ determination of the shape of supported silver clusters during growth," (in English), *Surface Science,* vol. 432, no. 3, pp. 257-264, Jul 20 1999.

[233] N. B. Leonov, S. G. Przhibel'skii, and T. A. Vartanyan, "Reversible relaxation of the shape of metal nanoparticles and its light-induced acceleration," (in English), *Jetp Letters,* vol. 91, no. 3, pp. 125-128, Feb 2010.

[234] X. Jiang, F. L. Wong, M. K. Fung, and S. T. Lee, "Aluminum-doped zinc oxide films as transparent conductive electrode for organic light-emitting devices," (in English), *Applied Physics Letters,* vol. 83, no. 9, pp. 1875-1877, Sep 1 2003.

[235] V. Kumar, R. G. Singh, L. P. Purohit, and R. M. Mehra, "Structural, Transport and Optical Properties of Boron-doped Zinc Oxide Nanocrystalline," (in English), *Journal of Materials Science & Technology,* vol. 27, no. 6, pp. 481-488, Jun 2011.

[236] L. Gao, Y. Zhang, J. M. Zhang, and K. W. Xu, "Boron doped ZnO thin films fabricated by RF-magnetron sputtering," (in English), *Applied Surface Science,* vol. 257, no. 7, pp. 2498-2502, Jan 15 2011.

[237] V. Bhosle, J. T. Prater, F. Yang, D. Burk, S. R. Forrest, and J. Narayan, "Gallium-doped zinc oxide films as transparent electrodes for organic solar cell applications," (in English), *Journal of Applied Physics,* vol. 102, no. 2, Jul 15 2007.

[238] N. K. Reddy, M. Devika, and K. Gunasekhar, "Stable and low resistive zinc contacts for SnS based optoelectronic devices," (in English), *Thin Solid Films,* vol. 558, pp. 326-329, May 2 2014.

[239] R. Xu *et al.*, "The fabrication of In2O3/In2S3/Ag nanocubes for efficient photoelectrochemical water splitting," *Phys Chem Chem Phys,* vol. 18, no. 4, pp. 2710-7, Jan 28 2016.

[240] G. Leftheriotis, P. Yianoulis, and D. Patrikios, "Deposition and optical properties of optimised ZnS/Ag/ZnS thin films for energy saving applications," (in English), *Thin Solid Films,* vol. 306, no. 1, pp. 92-99, Aug 28 1997.

[241] X. J. Liu, X. Cai, J. F. Mao, and C. Y. Jin, "ZnS/Ag/ZnS nano-multilayer films for transparent electrodes in flat display application," (in English), *Applied Surface Science,* vol. 183, no. 1-2, pp. 103-110, Nov 12 2001.

[242] X. J. Liu, X. Cai, J. S. Qiao, H. F. Mao, and N. Jiang, "The design of ZnS/Ag/ZnS transparent conductive multilayer films," (in English), *Thin Solid Films,* vol. 441, no. 1-2, pp. 200-206, Sep 22 2003.

[243] S. Papaefthimiou, G. Leftheriotis, and P. Yianoulis, "Advanced electrochromic devices based on WO3 thin films," (in English), *Electrochimica Acta,* vol. 46, no. 13-14, pp. 2145-2150, Apr 2 2001.

[244] S. Homaeigohar and M. Elbahri, "Switchable Plasmonic Nanocomposites," (in English), *Advanced Optical Materials,* vol. 7, no. 1, Jan 4 2019.

[245] S. Garshasbi and M. Santamouris, "Using advanced thermochromic technologies in the built environment: Recent development and potential to decrease the energy consumption and fight urban overheating," (in English), *Solar Energy Materials and Solar Cells,* vol. 191, pp. 21-32, Mar 2019.

[246] P. Jin, M. Tazawa, and G. Xu, "Reversible tuning of surface plasmon resonance of silver nanoparticles using a thermochromic matrix," (in English), *Journal of Applied Physics,* vol. 99, no. 9, May 1 2006.

[247] M. Maaza, O. Nemraoul, C. Sella, and A. C. Beye, "Surface plasmon resonance tunability in Au-VO2 thermochromic nano-composites," (in English), *Gold Bulletin,* vol. 38, no. 3, pp. 100-106, 2005.

[248] O. Neumann, A. S. Urban, J. Day, S. Lal, P. Nordlander, and N. J. Halas, "Solar vapor generation enabled by nanoparticles," *ACS Nano,* vol. 7, no. 1, pp. 42-9, Jan 22 2013.

[249] H. L. Duan, L. L. Tang, Y. Zheng, and C. Xu, "Effect of plasmonic nanoshell-based nanofluid on efficiency of direct solar thermal collector," (in English), *Applied Thermal Engineering,* vol. 133, pp. 188-193, Mar 25 2018.

[250] J. B. Chou *et al.*, "Design of wide-angle selective absorbers/emitters with dielectric filled metallic photonic crystals for energy applications," *Opt Express,* vol. 22 Suppl 1, pp. A144-54, Jan 13 2014.

[251] M. V. Pavliuk *et al.*, "Nano-hybrid plasmonic photocatalyst for hydrogen production at 20% efficiency," (in English), *Scientific Reports,* vol. 7, Aug 17 2017.

[252] B. Le Ouay and F. Stellacci, "Antibacterial activity of silver nanoparticles: A surface science insight," (in English), *Nano Today,* vol. 10, no. 3, pp. 339-354, Jun 2015.

[253] M. Liong *et al.*, "Multifunctional inorganic nanoparticles for imaging, targeting, and drug delivery," *ACS Nano,* vol. 2, no. 5, pp. 889-96, May 2008.

[254] S. Shrivastava, T. Bera, A. Roy, G. Singh, P. Ramachandrarao, and D. Dash, "Characterization of enhanced antibacterial effects of novel silver nanoparticles," (in English), *Nanotechnology,* vol. 18, no. 22, Jun 6 2007.

[255] S. I. Chung, P. K. Kim, T. G. Ha, and J. T. Han, "High-performance flexible transparent nanomesh electrodes," *Nanotechnology,* vol. 30, no. 12, p. 125301, Mar 22 2019.

[256] L. B. Hu, H. Wu, and Y. Cui, "Metal nanogrids, nanowires, and nanofibers for transparent electrodes," (in English), *Mrs Bulletin,* vol. 36, no. 10, pp. 760-765, Oct 2011.

[257] C. Bao *et al.*, "In situ fabrication of highly conductive metal nanowire networks with high transmittance from deep-ultraviolet to near-infrared," *ACS Nano,* vol. 9, no. 3, pp. 2502-9, Mar 24 2015.

[258] P. B. Catrysse and S. H. Fan, "Nanopatterned Metallic Films for Use As Transparent Conductive Electrodes in Optoelectronic Devices," (in English), *Nano Letters,* vol. 10, no. 8, pp. 2944-2949, Aug 2010.

APPENDIX A   TRANSMISSION CALCULATION COEFFICIENTS

Table A.1 : Normalized relative spectral distribution

$D_{65}(\lambda)V_{ph}(\lambda)\Delta\lambda$ for the calculation of the Visible Solar Transmittance (T_{vis})

Wavelength (nm)	$D_{65}(\lambda)V_{ph}(\lambda)\Delta\lambda$	Wavelength (nm)	$D_{65}(\lambda)V_{ph}(\lambda)\Delta\lambda$
380	0	590	0.063306
390	0.000005	600	0.053542
400	0.000030	610	0.042491
410	0.000103	620	0.031502
420	0.000352	630	0.020812
430	0.000948	640	0.013810
440	0.002274	650	0.008070
450	0.004192	660	0.004612
460	0.006663	670	0.002485
470	0.009850	680	0.001255
480	0.015189	690	0.000536
490	0.021336	700	0.000276
500	0.033491	710	0.000146
510	0.051393	720	0.000057
520	0.070523	730	0.000035
530	0.087990	740	0.000021
540	0.094427	750	0.000008
550	0.098077	760	0.000001
560	0.094306	770	0.000000
570	0.086891	780	0.000000
580	0.078994		

A.2 : Normalized relative spectral distribution of global solar radiation for the

calculation of the Solar Transmittance (Ts$_{ol}$)

Wavelength (nm)	$S_{sol}(\theta,\lambda)\Delta\lambda$	Wavelength (nm)	$S_{sol}(\theta,\lambda)\Delta\lambda$	Wavelength (nm)	$S_{sol}(\theta,\lambda)\Delta\lambda$
300	0	520	0.015357	1000	0.036097
305	0.000057	530	0.015867	1050	0.034110
310	0.000236	540	0.015827	1100	0.018861
315	0.000554	550	0.015844	1150	0.013228
320	0.000916	560	0.015590	1200	0.022551
325	0.001309	570	0.015256	1250	0.023376
330	0.001914	580	0.014745	1300	0.017756
335	0.002018	590	0.014330	1350	0.003743
340	0.002189	600	0.014663	1400	0.000741
345	0.002260	610	0.015030	1450	0.003792
350	0.002445	620	0.014859	1500	0.009693
355	0.002555	630	0.014622	1550	0.013693
360	0.002683	640	0.014526	1600	0.012203
365	0.003020	650	0.014445	1650	0.010615
370	0.003359	660	0.014313	1700	0.007256
375	0.003509	670	0.014023	1750	0.007183
380	0.003600	680	0.012838	1800	0.002157
385	0.003529	690	0.011788	1850	0.000398
390	0.003551	700	0.012453	1900	0.000082
395	0.004294	710	0.012798	1950	0.001087
400	0.007812	720	0.010589	2000	0.003024
410	0.011638	730	0.011233	2050	0.003988
420	0.011877	740	0.012175	2100	0.004229
430	0.011347	750	0.012181	2150	0.004142
440	0.013246	760	0.009515	2200	0.003690
450	0.015343	770	0.010479	2250	0.003592
460	0.016166	780	0.011381	2300	0.003436
470	0.016178	790	0.011262	2350	0.003163
480	0.016402	800	0.028718	2400	0.002233
490	0.015794	850	0.048240	2450	0.001202
500	0.015801	900	0.040297	2500	0.000475
510	0.015973	950	0.021384		

APPENDIX B   LIST OF PUBLICATIONS

The doctoral project presented in this thesis has yielded several publications in peer-reviewed journals, international conferences and collaborations with other research groups. These academic achievements are presented below

Peer-reviewed journal publications

1.   Soroush Hafezian, Bill Baloukas, and Ludvik Martinu, "Percolation threshold determination of sputtered silver films using Stokes parameters and *in situ* conductance measurements," Appl. Opt. 53, 5367-5374 (2014)

2.   Soroush Hafezian, Kate Maloney, Josianne Lefebvre, Ludvik Martinu, and Stéphane Kéna-Cohen, "Continuous ultrathin silver films deposited on SiO_2 and SiN_x using a self-assembled monolayer," Appl. Phys. Lett. 109, 121603 (2016)

3.   Soroush Hafezian, Rodrigue Béaini, Stéphane Kéna-Cohen, Ludvik Martinu, "Degradation mechanism of protected ultrathin silver films and the role of seed layer, " Appl. Surf. Sci. 484, 335-340, (2019)

Peer-reviewed collaborations

1.   Lili Wang, Dhanashree Moghe, Soroush Hafezian, Pei Chen, Margaret Young, Mark Elinski, Ludvik Martinu, Stéphane Kéna-Cohen, and Richard R. Lunt, "Alkali Metal Halide Salts as Interface Additives to Fabricate Hysteresis-Free Hybrid Perovskite-Based Photovoltaic Devices," ACS Appl. Mater. Interfaces, 8 (35), pp 23086–23094, 2016

2.   Julien Brodeur, Romain Arguel, Soroush Hafezian, Fábio Barachati, and Stéphane Kéna-Cohen, "Nearly 40% outcoupling efficiency in OLEDs with all-metal electrodes," Appl. Phys. Lett. 113, 041105 (2018)

3.   Fábio Barachati, Antonio Fieramosca, Soroush Hafezian, Jie Gu, Biswanath Chakraborty, Dario Ballarini, Ludvik Martinu, Vinod Menon, Daniele Sanvitto and Stéphane Kéna-Cohen, "Interacting polariton fluids in a monolayer of tungsten disulfide," Nature Nanotechnology, 13, pages 906–909 (2018)

International conferences

1.   Soroush Hafezian, Kate Maloney, Josianne Lefebvre, Ludvik Martinu, Stéphane Kéna-Cohen, "Continuous ultrathin silver films deposited on SiO_2 and SiN_x using a self-assembled monolayer," ICOOPMA, Montreal, June 2016

2.   Soroush Hafezian, Stéphane Kéna-Cohen, Ludvik Martinu, "Optical properties of 1-DT stabilized silver nanoparticles," FCSE, Montreal, June 2017

3.   Soroush Hafezian, Rodrigue Béaini, Ludvik Martinu, Stéphane Kéna-Cohen, "Treatment against process oxidation of ultra-thin silver films," MRS, Boston, November 2018